Rev.	Publish date	Description	Made by	Checked by	Project appro.	Client appro.
0	15.08.2019	Final issue	KAK	RML	SEJ	

Client

Statens vegvesen

Contractor

AAS-JAKOBSEN COWI Multiconsult
JOHS HOLT AkerSolutions entail NGI DISSING+WEITLING architecture a/s mossmaritime

Contract no.:

18/91094

Document name:

Preferred solution, K12 – Appendix S

Parametric excitation

Document no.:	Rev.:	Pages:
SBJ-33-C5-AMC-90-RE-119	0	214

CONCEPT DEVELOPMENT, FLOATING BRIDGE E39 BJØRNAFJORDEN

Preferred solution, K12

Appendix S – Parametric excitation

CLIENT

Statens vegvesen

DATE: / REVISION: 15.08.2019 / 0

DOCUMENT CODE: SBJ-33-C5-AMC-90-RE-119

AAS-JAKOBSEN COWI Multiconsult

JOHS HOLT AkerSolutions entail NGI DISSING+WEITLING architecture a|s mossmaritime

REPORT

PROJECT	Concept development, floating bridge E39 Bjørnafjorden	DOCUMENT CODE	SBJ-32-C5-AMC-90-RE-119
SUBJECT	Appendix S – Parametric excitation	ACCESSIBILITY	Restricted
CLIENT	Statens vegvesen	PROJECT MANAGER	Svein Erik Jakobsen
CONTACT	Øyvind Kongsvik Nedrebø	PREPARED BY	Knut Andreas Kvåle, Mads Fredrik Heiervang, Finn-Idar Grøtta Giske
		RESPONSIBLE UNIT	AMC

SUMMARY

The main purpose of phase 5 of the E39 Bjørnafjorden project is to identify and document which of the four described bridge alternatives that may be regarded as the best solution. In this context, AMC have assessed the concepts' robustness with regards to parametric excitation. Parametric excitation is considered as an effect that may be crucial for the safety of the concepts.

In contrast to traditional resonance, where an external force applied at or near a natural frequency of the structure causes resonance, parametric excitation is caused by an oscillating variation of one or more of the system properties. Parametric excitation may be far more aggressive and more dangerous than traditional resonance due to the exponential growth of response over time even for a system with damping [1] [2]. The focus for the Bjørnafjord Bridge has been parametric excitation caused by an axial force variation that induces variation in the geometric stiffness of the system. An attempt to give a simple description of a complex and challenging problem may be as follows: the variation of the axial force in the slender girder of the Bjørnafjord Bridge concepts is a source to stiffness variation that leads to amplification of the load effects at frequencies other than the loading frequencies. The challenge has thus been addressed by the looking into the following topics:

- Determination of the axial force variation for the different concepts and for different loadings
- Applying the defined criterion for possible onset of parametric resonance on the possible concepts
- Establishing a criterion for evaluation of a threshold (denoted *terminal* in the current document) level for the parametric resonance response taking into account the effect of present nonlinear/quadratic damping
- Establishing how the stochastic nature of the loading should be treated
- Establishing procedures for evaluating the effects of:
    - o the magnitude of the external force
    - o the external static forces
    - o the effect of wide-bandedness

Based on these studies and the established procedures, the robustness of the four concepts regarding this topic have been documented and compared in a quantitative manner. As a short summary, the following results are found:

- K11: onset will occur, threshold response is of some magnitude
- K12: onset may occur, but threshold response is low
- K13: is not exposed to parametric resonance at all, due to its limited ability to build up net dynamic axial force in the girder
- K14: onset may occur, but threshold response is low

0	15.08.2019	Final issue	K. A. Kvåle	R. M. Larssen	S. E. Jakobsen
REV.	DATE	DESCRIPTION	PREPARED BY	CHECKED BY	APPROVED BY

TABLE OF CONTENTS

1 Overview and summary

1.1 General

The main purpose of phase 5 of the E39 Bjørnafjorden project is to identify and document which of the four described bridge alternatives that may be regarded as the best solution. In this context, AMC have assessed the concepts' robustness with regards to parametric excitation. Parametric excitation is considered as an effect that may be crucial for the safety of the concepts.

In contrast to traditional resonance, where an external force applied at or near a natural frequency of the structure causes resonance, parametric excitation is caused by an oscillating variation of one or more of the system properties. Parametric excitation may be far more aggressive and more dangerous than traditional resonance due to the exponential growth of response over time even for a system with damping [1] [2].

There are several parameters that could, in principle, trigger such resonances, however the axial force variation is considered most critical for the Bjørnafjord Bridge because of the slender bridge girder with several low-damped lateral eigenmodes.

An attempt to give a simple description of the complex and challenging issue may be as follows:

The dynamic axial force response in the slender bridge girder is the source of a geometric stiffness variation that may lead to a large and unacceptable amplification of the load effects at other frequencies than the loading frequencies.

1.2 Conclusion

The main finding is that the curved concepts (K11, K12, K14) are prone to parametric excitation from swell waves, as there is a critical axial eigenmode exposed to a high modal force with low linear damping in the swell frequency range (around 13 seconds). Also, the triggered eigenmode at around half the frequency has low linear damping. Consequently, all curved concepts *fail* the defined onset criterion, proposed by the client.

The mooring line damping for the side anchored concepts (K12 and K14) gives a significant contribution to the damping both for the critical axial eigenmode and the triggered eigenmode. The mooring damping reduces the axial force response and ensures a high damping level at the triggered eigenmode. Because of the mooring damping contribution, *the K12 and K14 concepts are considered robust* with regards to parametric excitation, even though the concepts fail the onset criterion.

The K11 concept has a low level of quadratic damping and has a significantly higher axial force response. As such, there is a risk of an unacceptable response from parametric excitation. Thus, *the K11 concept does not show the necessary robustness* for parametric excitation that AMC requires at this stage of concept development and with the current knowledge about the phenomenon.

A possible design mitigation for the K11 concept is to release the bridge girder at the tower and back spans, such that dashpots can be positioned at the tower connection and introduce a linear damping. Preliminary analysis show that this design mitigation will give a significant damping contribution such that the onset criterion may be fulfilled. However, the dashpot damper design has not been detailed, and as such there is an uncertainty to whether this design measure will be feasible.

1.3   Method

To evaluate parametric excitation AMC has applied the following procedure:

- Global response analysis of the defined swell, windsea and wind conditions to determine the dynamic axial force response (σ_N).

- Evaluate the critical axial force response (A_{cr}) for each uncoupled eigenmode and each critical frequency ratio considering the geometric stiffness variation and damping of each mode.

- Evaluating the defined onset criterion for parametric excitation:
  $\frac{\sigma_N}{0.4} < A_{cr}$.

- If the concept fails the onset criterion, the threshold response for the parametric excitation, based on approximating the stochastic axial force variation as harmonic, is calculated. For determination of the threshold response, the effect of quadratic damping is included, and the response level is based on a probability of exceedance of 0.01% and 10% for the 100-year and 10 000-year conditions, respectively.

- Quantify the threshold response including a 20% reduction of quadratic damping and a 20% increase of the axial force response level. This last step is made as a robustness check to account for the related uncertainties.

The available knowledge on this complex phenomenon is limited, and care should therefore be taken in all steps related to its treatment. As the onset criterion is exceeded, there is an inherent uncertainty of the response from parametric excitation. Therefore, it has been of utmost importance to perform specialized studies such that a robust methodology is developed. The following findings are of particular importance:

- For the evaluation, the axial force is applied at a single frequency. Therefore, the effect of the spectral bandwidth is studied. For the broad banded wind sea axial force response, only a limited frequency range will contribute to parametric excitation, such that the applicable axial force response is reduced. The effect of frequency distribution on parametric excitation from swell is limited, and is evaluated to cause roughly a 10% reduction of the threshold response. This effect is not accounted for in the presented results, but is quantified for selected modes.

- An external load (from wind or second order wave effects) may cause a stochastic response of the triggered mode, and significantly affect the results. For an evaluation with a weak or no external load, parametric excitation is rarely observed in the realizations and as a result the process is not well-behaved. Thus, the methodology is based on applying an external load together with the axial force variation, which ensures the following process characteristics:

  o   Low simulation time to build up response from parametric excitation

  o   Significant reduction of rare events

  o   Improved probability distribution fit to the Gumbel distribution

  o   Improved overall *well-behavedness*

- Realistic uncertainties (20%) in the axial force and quadratic damping could potentially increase the response significantly (roughly 100% increase). This effect is accounted for by the robustness check of the terminal response.

1.4   Sensitivities and uncertainties

An important focus has been to build a thorough understanding of the mooring line damping, such that critical parameters are identified for this essential damping contribution for the K12 and K14 concepts. A simplified method to verify and quantify the mooring line damping is presented in Appendix F, Enclosure 2. The mooring line static / mean tension is a governing and somewhat uncertain value. For the K14 concept, the current, mean wind, temperature and tide may affect the static tension. For the K12 concept, it is mainly the temperature and tide that affects the static tension as a substantial part of the horizontal loads are carried through arch action. A combination of an extreme tide and an extreme temperature condition may result in a 20-25% reduction of the mooring line damping.

The viscous damping on the pontoons is studied in Appendix H. The study shows that there are uncertainties related to the stationary drag coefficient, the dependency on the KC-number and 3-dimensional effects. The hydrodynamic linear radiation damping is based on linear potential theory, and the correlated uncertainties are considered low. However, a small reduction may lead to a large increase of response.

The axial force response is sensitive to the defined Metocean basis [3]. A complete screening of the sea state has been performed to select the most critical sea states. Sensitivity studies of the spectrum parameters are also performed. The studies show that a high number of wave components is necessary to obtain the correct level of response, particularly so for the K11 concept in swell conditions, which is characterized by low damping.

1.5   Validation

In order to build a better understanding and to validate the results of the uncoupled eigenmodes, the global analysis model in OrcaFlex has been subjected to loads that trigger parametric excitation. For harmonic analyses, where the global model is subjected to an equal axial force response, the same level of response to parametric excitation as the single-degree-of-freedom (SDOF) model is observed. Also, stochastic analysis of the global analysis model verifies that an external load at the triggered mode may amplify the effect of parametric excitation.

In the global analysis, a reduction in the axial force response is observed after the onset of parametric excitation, which results in a substantially lower level of the axial force response. This reduction of axial response is not accounted for in the SDOF results, where frequency domain results (linear analysis) are used as input.

1.6   Results

A summary of the results is found in Table 1-1.

Table 1-1: Overview of results from parametric excitation. The onset criterion denotes the recommended procedure from client for evaluation of parametric resonance. The 100-year and 10 000-year threshold response denotes the expected dynamic response for a probability of exceedance of 0.01% and 10%, respectively. The threshold response robustness check denotes the defined threshold response including a 20% reduction of quadratic damping and a 20% increase of the axial force response level.

Concept	Condition	Return period	Onset criterion	Threshold response [MPa]	Threshold response robustness check [MPa]
K11	Swell	100	Fails	475	752
		10000	Fails	332	537
	Windsea	100	OK	N/A	N/A
		10000	OK	N/A	N/A
	Wind	100	OK	N/A	N/A
		10000	OK	N/A	N/A
K12	Swell	100	Fails	26	43
		10000	Fails	16	27
	Windsea	100	OK	N/A	N/A
		10000	OK	N/A	N/A
	Wind	100	OK	N/A	N/A
		10000	OK	N/A	N/A
K13	Swell	100/10000	OK	N/A	N/A
	Windsea	100/10000	OK	N/A	N/A
	Wind	100/10000	OK	N/A	N/A
K14	Swell	100	Fails	30	56
		10000	Fails	4	17
	Windsea	100	OK	N/A	N/A
		10000	OK	N/A	N/A
	Wind	100	OK	N/A	N/A
		10000	OK	N/A	N/A

2   Introduction

Parametric excitation is identified as an important topic to evaluate in the design of the Bjørnafjord Bridge. Parametric excitation is triggered by a dynamic variation of one or more of the system's parameters and causes the system to become unstable. In the work by NTNU [2], it was identified that the Bjørnafjord Bridge concept may be vulnerable to parametric variations in the bridge girder's geometric stiffness caused by an axial force variation, as it is a slender bridge with several low-damped lateral eigenmodes. Parametric resonance is characterized by an exponential growth of response over time, even in the presence of damping, and is considered more dangerous than traditional resonance where the response grows linearly in the absence of damping [4]. However, the complex dynamic behaviour and the inherent uncertainties at this stage makes the instability challenging to assess.

For systems that are well-behaved, extreme values are occurring in a relatively predictable manner, without rare events. Parametric resonance may affect a system's behaviour such that at rare conditions, a much larger response suddenly occurs. Deterministic time-variation of system parameters induced by external excitation could generally be handled by a nonlinear computational setup, which update the model's properties and characteristics throughout the simulation. The traditional approach for the nonlinear analysis of systems exposed to stochastic excitations relies on brute force Monte Carlo simulation, which is based on sampling multiple deterministic excitation time series from the stochastic description, to render corresponding deterministic response. By running many simulations, an approximation of the stochastic response is established. As stated in Øiseth et al. [2], this approach might not capture the effects of parametric resonance, because only certain combinations of response and excitation values will bring the system into an unstable state. The parametric resonance may occur in a few of the stochastic simulated realizations of selected extreme conditions (response from wave and wind conditions); however, the phenomena will not occur at all in most of the realizations. As indicated herein, it could perhaps still be a plausible route later, under certain modelling circumstances. However, as the available literature and knowledge on similar applications are currently highly limited, it is reasonable to avoid the extra uncertainties this involves and ensure a conservative attitude towards the unknown phenomenon. The complex nature of parametric resonance of stochastically excited systems motivates a simplified approach to deal with the phenomenon.

The procedure suggested in Øiseth et al. [2] relies on ensuring that onset of parametric excitation does not occur. Because *the onset* of instability should be avoided, no parametric excitation is allowed to initiate, and the damping should be linearized about the system state prior to any response due to the parameter variation. For modes where the damping contributions are mainly of nonlinear nature, predominately from quadratic drag damping originating from anchoring systems and pontoons, the criterion to avoid onset may be too strict to be fulfilled for all load cases and concepts. Due to this, a need to quantify the consequence of the observed exceedances of the criterion emerges: a simplified method to account for the quadratic drag damping is suggested.

2.1   Scope and limitations

The scope has been to perform the assessment according to the recommendation in the report received from the client [2]. As the preferred concepts does not fulfil the given criterion, a significant part of the work has been to establish a methodology that can account for the quadratic damping contribution and still evaluate the concepts in a robust manner.

As implied above, the only parameter variation studied is the geometric stiffness change due to axial force variation. Other examples of parameter variations that, in principle, could trigger parametric resonance are:

- Geometric stiffness due to *bending moments* in girder. The effect of this is believed to be very limited compared to the effect from axial forces.

- Added mass due to changing draft or rotations of pontoons. The heave motion is dominated by motion around 6 seconds and is not believed be an important issue.

- Hydrostatic stiffness (from restoring forces) due to changing draft or rotations of pontoons. The restoring loads only affect vertical and rotational eigenmodes which have a high linear hydrodynamic damping.

Furthermore, the evaluation has been performed with uncoupled eigenmodes, such that coupling effects are not accounted for. However, the results have been benchmarked with the global analysis model.

Important limitations for the global analysis are given in Appendix F. The axial force response has been treated separately as this is considered more robust and give a better understanding of the individual load groups. The aerodynamic damping is accounted for in the evaluations of wind-generated waves. In addition, the following effects have not been considered for the global response analyses for evaluation of parametric resonance:

- The effect of wave current interaction.

- The effect of an inhomogenous sea state.

- Second order wave effects

- Hydrodynamic interaction between the pontoons

The abovementioned topics are addressed in Appendices G and H.

2.2 Conservativism

Parametric resonance in the context of stochastic excitation is considered a complex phenomenon, and one that should be treated carefully. By allowing the *onset criterion* to be exceeded, more uncertainty is to be expected. Because the consequence of errors could potentially be very large, see, e.g., Section 7, all assumptions should be made with a conservative approach. The conservativism of the proposed method is deemed good based on the following aspects:

- The stochastic nature of the excitation sources acting on the bridges are believed to make it less likely for the structures to enter into instabilities. Even wide banded processes are assumed to be harmonic.

- All energy within a segment is assumed to act with the worst frequency ratio to all relevant modes.

- The suggested procedure does not assume anything on the requirement of the duration of the axial force variation to induce a stationary response. As indicated in the next section, the duration of the harmonic excitation in low-damped systems is very important to reach large amplitudes. The assumptions above is assuming a steady-state, never-ending, harmonic excitation.

- As shown in Section 4.3, the single-degree-of-freedom assumption likely produce conservative axial force variation amplitudes. In reality, the axial force is likely reduced when the response in the parametrically excited modes is induced.

- If multiple modes are prone to become parametrically excited, they are all assumed to be so at the same time. This implies that the energy from the axial force variation enters multiple modes according to the methodology suggested.

2.3 Structure of the appendix and recommended reading

The amount of content in the current document is extensive; to make it more accessible to the readers less involved in the details of the topic, a prioritized list of the sections giving most value to a new reader is provided below.

1. **Sections 1 (Summary) and 2 (Introduction)**

2. **Section 6: Assessment of the concept's performance with regard to parametric excitation, based on the suggested simplified procedure**

3. Section 3: Methodology behind the procedure used to assess the effects of parametric excitation

4. Section 7: Study on the sensitivity of the parameters involved in the simplified procedure

5. Section 5: Global axial force response

6. Section 4: More specialized topics

7. Section 8: Study of parametric excitation in global analysis models

8. Section 9: Mitigation strategies to improve robustness of K11

3 Methodology

3.1 Introduction

In [2], the client and NTNU outline a method to evaluate the robustness against parametric resonance. In the note, a linearized procedure is proposed to evaluate the instability using uncoupled modes, i.e., as multiple single-degree-of-freedom (SDOF) problems. This linear procedure is briefly presented in Section 3.3.

The proposed criterion has shown to be difficult to satisfy for the concepts as it inherently disregards the quadratic damping, which is the main damping contribution in the critical frequency range. Through mathematical derivation, supported by a significant amount of simulations, it is found that the response from harmonic parameter variation will stabilize at a terminal value when quadratic damping is included. However, the terminal value is sensitive to the quadratic damping coefficients and the axial force variation. The procedure used to estimate the terminal values is presented in Section 3.4.

3.2 Mathematical interpretation of parametric resonance

The response of an SDOF system due to an external force $p(t)$ is established from the well-known general equation of motion:

$$\ddot{y}(t) + 2\xi\omega_n\dot{y}(t) + \omega_n^2 y(t) = \frac{p(t)}{m}$$

where ξ is the critical damping ratio, ω_n is the natural frequency, $y(t)$ is the generalized SDOF response, and $p(t)$ is the external force. Contrary, parametric resonance is a phenomenon that induces response in a dynamic system due to oscillations in the system coefficients, as follows:

$$\ddot{y}(t) + 2\xi\omega_n\dot{y}(t) + \omega_n^2\big(1 - 2\mu\Phi(t)\big)y(t) = 0 \tag{1}$$

This equation is known as the *Mathieu-Hill equation*, where $\mu\Phi(t)$ describes some applied parameter variation.

When Equation 1 is simplified such that $\Phi(t) = \cos(\omega t)$, it is reduced to what is referred to as the *Mathieu equation*, and it can be solved rather straightforwardly, either numerically or analytically. This is written as follows:

$$\ddot{y} + 2\xi\omega_n\dot{y} + \omega_n^2(1 - 2\mu \cdot \cos\omega t)y = 0$$

The *Ince-Strutt* diagram depicts the combinations of amplitude and load frequency of a harmonic parameter variation that define the stability border, i.e., indicating for what combinations the system is on the border between stable and unstable. By normalizing the coefficients defining the SDOF system, a general diagram can be made for every critical damping ratio, as illustrated in Figure 3-1. This result can be produced either numerically or analytically [5]. Here, the frequency ratio between the parameter variation and the normal mode of the system is given as $\beta = \omega/\omega_n$. As the figure indicates, the minimum amplitude related to each excitation frequency (or instability region) varies and shows to be most critical for frequency ratios close to 2.0. The critical amplitudes of the various instability regions are in the order of $(2\xi)^{1/k} = (2\xi)^{\beta/2}$, where k indicates the index of the instability region [1].
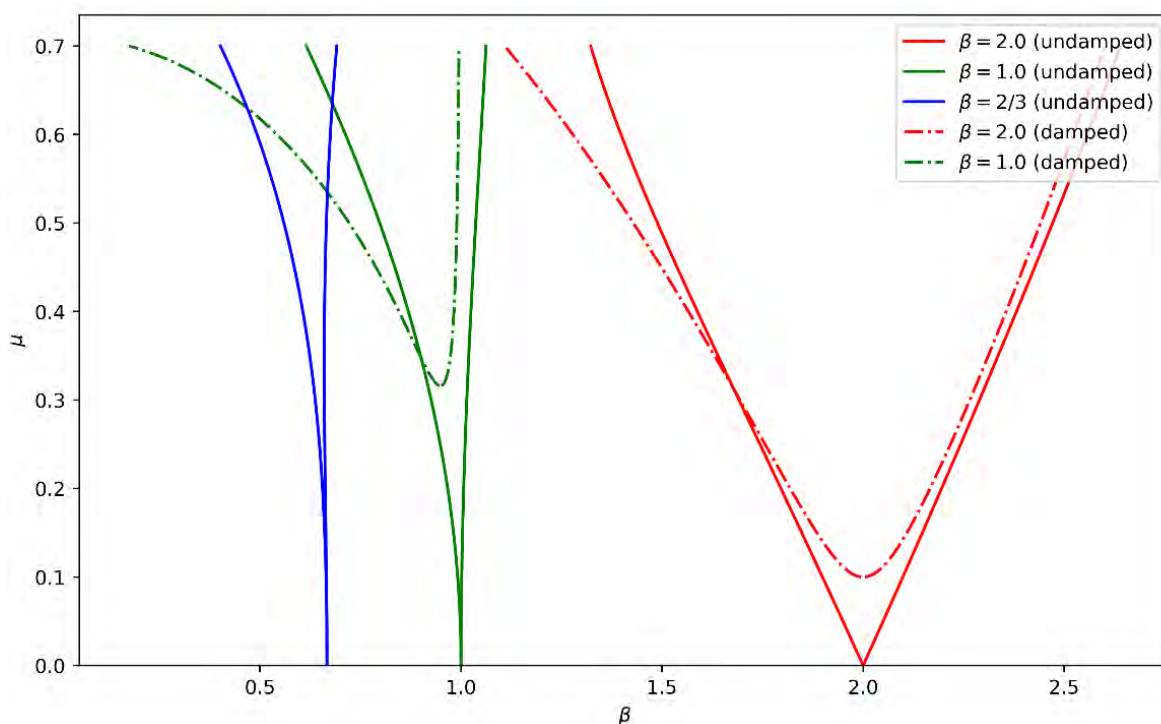
Figure 3-1. Ince-Strutt diagram indicating the stability bounds of a generic SDOF system. The x-axis represents frequency ratio between parameter variation frequency and natural frequency, whereas the y-axis indicates the amplitude of the parameter variation.

Table 3-1. Approximate critical amplitudes of the three first stability regions.

Stability region	Frequency ratio, $\beta = \frac{\omega}{\omega_n}$	Critical amplitude, μ_{cr}
First	2.0	2ξ
Second	1.0	$\sqrt{2\xi}$
Third	0.5	$(2\xi)^{1/3}$

3.3   Linearized onset criterion

To deal with stochastic axial force variation, it is suggested to ensure that the standard deviation σ_N of the axial force variation fulfils the following criterion in [2]:

$$\sigma_N < 0.4 A_{cr}$$

To establish the critical harmonic amplitudes (A_{cr}) of a certain mode, the following expression is indirectly given in [2]:

$$A_{cr} = 2\mu_{cr} \frac{k_{tot}}{\hat{k}_g}$$

where μ_{cr} is the critical amplitude as represented in the Mathieu equation, k_{tot} is the total stiffness of the mode (including static geometric stiffness), and $\hat{k}_g$ is the geometric stiffness contribution to the mode normalized by the amplitude of the dynamic axial force distribution, such that the total instantaneous stiffness is $k - N\cos(\omega t)\,\hat{k}_g$. Table 3-1 shows the value of μ_{cr} for the three first instability regions. As an approximation, the critical amplitude corresponding to the first stability region, corresponding to $\beta = 2.0$, can be rewritten as follows:

$$A_{cr} = 4\xi \frac{k}{\hat{k}_g} \approx 4\xi \left(P_{cr} - P_{0,axial} \right)$$

3.4 Terminal level estimation

The criterion to avoid the expected axial force amplitude to exceed the critical harmonic amplitude for all modes, suggested in the provided background material by the client [2], is concerning the onset of parametric resonance (herein denoted as the *onset criterion*). This implies that the evaluation of stability should be based on the model's static state. According to the background material, the onset criterion therefore relies on including only the linear damping, as the nonlinear damping contributions are only present when the parametric resonance has occurred. In the bridge concepts, quadratic drag damping is originating from mooring lines and pontoons. None of the bridge concepts evaluated are strictly passing the criterion for all the relevant excitation cases, and a need to quantify the consequence of the observed exceedances emerges. Motivated by this, a method to estimate the terminal response of a quadratically damped SDOF system, i.e., vibration mode, exposed to a parameter variation with twice the frequency of the natural frequency, is given in Enclosure 1. The term *terminal* is chosen deliberately to indicate that the response value is only reached asymptotically. Furthermore, by approaching the stochastic parameter variation as harmonic, an estimate of the corresponding terminal response can be established. The mathematical details and verification studies of the terminal level is provided in Enclosure 1. The most important aspects are repeated below.

The equation of motion including quadratic drag damping reads out as follows:

$$\ddot{y} + 2\xi\omega_n\dot{y} + \frac{c_{quad}}{m}|\dot{y}|\dot{y} + \left(\omega_n^2 + \frac{\hat{k}_g}{m} \cdot N(t) \right) y = \frac{p(t)}{m} \tag{2}$$

c_{quad} denotes the quadratic damping coefficient. As reported in Enclosure 1, the terminal generalized response of an SDOF system exposed to harmonic geometric stiffness variation $N \cdot \hat{k}_g \cdot \cos(2\omega_d t)$ can be expressed as follows:

$$y_0 = 3\pi \frac{N \cdot \hat{k}_g - 2c_{lin}\omega_n}{16c_{quad}\omega_n^2} \tag{3}$$

where N is the amplitude of the axial force and c_{lin} the linear damping contributions. The suggested method is equivalent to linearizing the quadratic damping at the instantaneous response amplitude in a time domain simulation and assessing the critical amplitude with that linearized damping. As the response grows, the damping increases, and at a certain level the applied axial force amplitude is equal to the critical amplitude; the linearized system has stabilized. Figure 3-2 and Figure 3-3 exemplify the converged response and effective critical amplitude calculated from instantaneously linearized quadratic damping, respectively, and supports the assessment above.
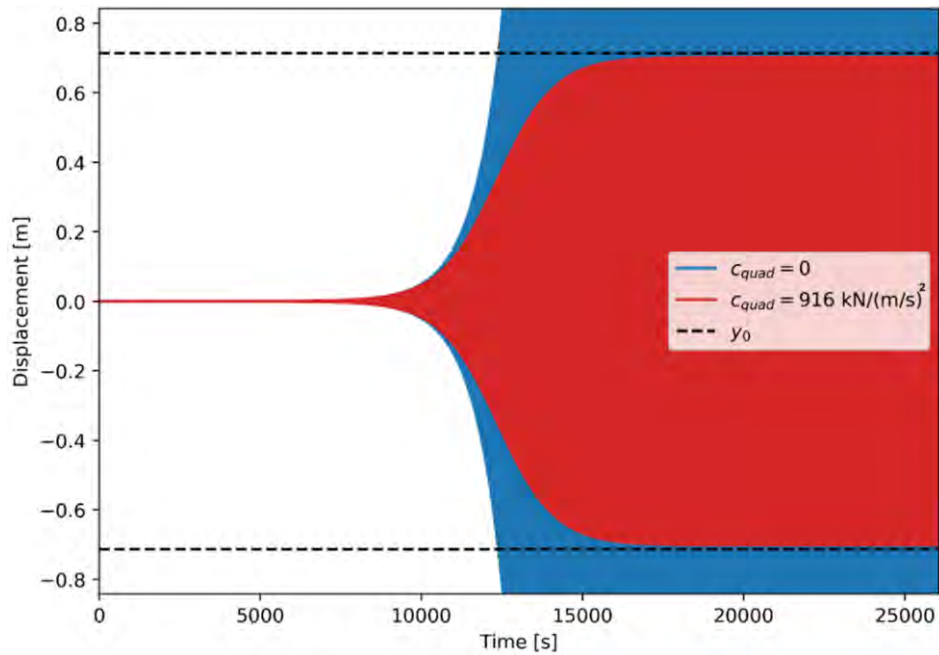
Figure 3-2. $N = 2.0A_{cr}$. With and without drag damping. The estimated terminal level is shown for comparison.
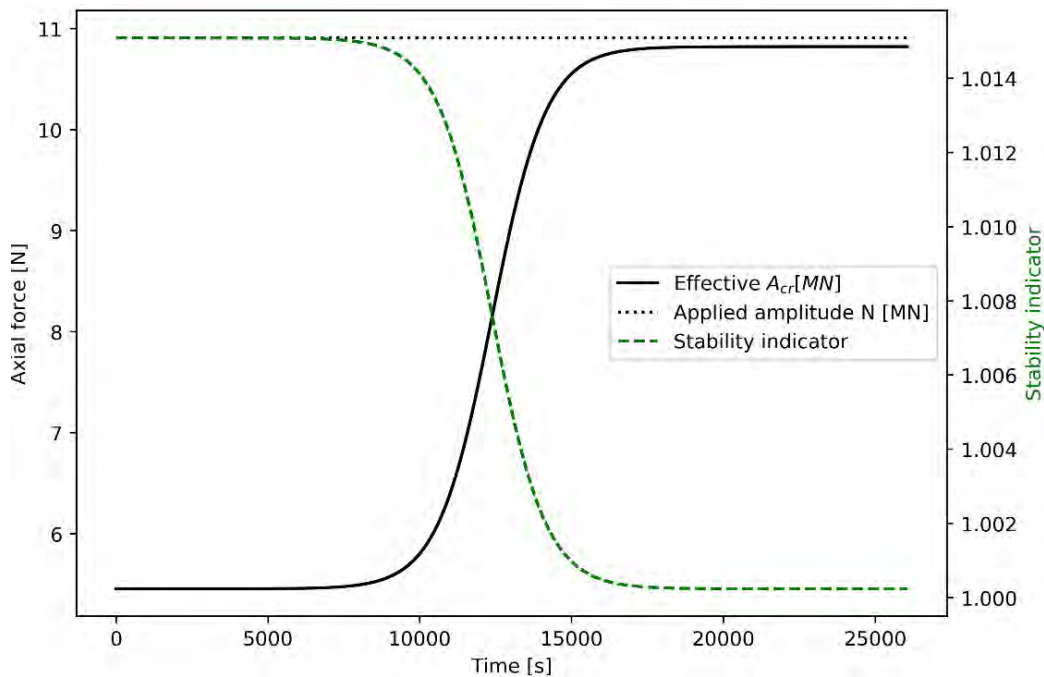
Figure 3-3. The effect on the effective critical amplitude as the quadratic drag damping increases with increasing amplitude. Initially the amplitude of the axial force is set to $N = 2.0A_{cr}$. The stability indicator is based on the eigenvalues of the matrix $[B]$ found in Equation 1 in Enclosure 1, which indicates stable solutions when at or below 1.0.

3.4.1 Approaching the stochastic parameter variation as harmonic

The stochastic axial force variation is assumed to be completely characterized by a spectral density, obtained by a frequency domain analysis of the global response to a set of extreme conditions. An example is shown in Figure 3-4, which depicts a power spectral density characterizing the axial force

variation due to a swell condition ($H_s = 0.46m$, $T_p = 13s$), and a short time segment of a selected realization corresponding to the spectral density.

To deal with the complex phenomenon, the stochastic axial force variation is approached as a single-component harmonic process, that should predict response on the conservative side. A harmonic axial force variation is defined as follows:

$$N(t) = A \cdot \cos(2 \cdot \omega_d t)$$

where ω_d is the damped natural frequency of the system.

The response of the system could then be considered mode by mode, assuming that all, or a segment within a relevant frequency band, is acting as a harmonic axial force variation for each mode. If the resulting terminal response, corresponding to a maximum load effect (bending moments, axial force, stress in extreme fibre, etc.), is not acceptable, the structure has failed the check.
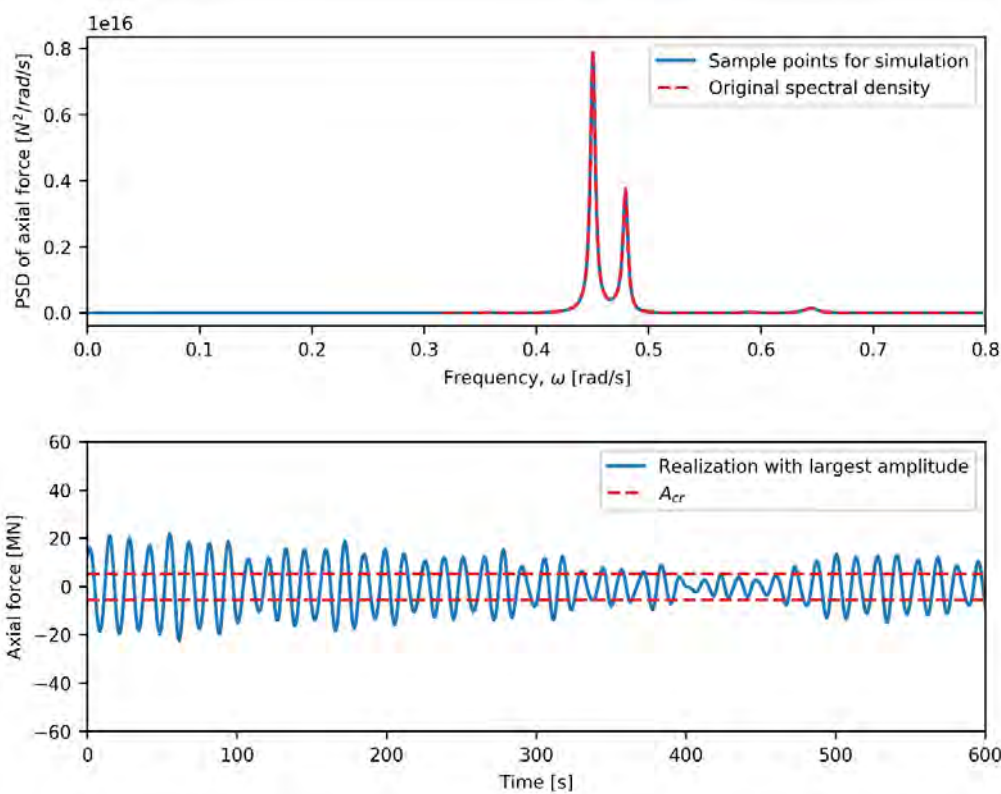
Figure 3-4. Power spectral density of the axial force variation, and a short segment of a selected realization corresponding to the spectral density.

3.4.1.1   *Equal-variance harmonic process*

The first, and rather engineering-based, approach is to assume equal variance. This implies that the variance of the axial force (the integral of the spectral density) σ_N^2, is used to establish the amplitude of a harmonic process with the same variance. The variance of a harmonic process with amplitude A is given as $\sigma^2 = \frac{A^2}{2}$. By utilizing this, the amplitude of the harmonic process can be assumed as follows:

$$A = \sqrt{2}\sigma_N$$

3.4.1.2   Based on Xie criterion

Xie [1] proposes an *almost-sure* criterion that relates the standard deviation of the axial force, for a frequency ratio between the applied parameter variation and the resonance frequency of 2.0, that reads out $\sigma_N < 0.5 A_{cr}$. Based on the same logic, the amplitude of the harmonic case representing a conservative approximation of the stochastic variation, can be set as follows:

$$A = 2\sigma_N$$

3.4.1.3   Using the expected peak value of the stochastic process

The expected peak value of the stochastic axial force process is used to suggest a criterion in [2]. The amplitude of the harmonic axial force variation is then chosen as the expected peak value during a period T of a Gaussian process as follows:

$$A = E[\max(N(t);\ 0 < t < T)] = \sqrt{2\ln(2f_n T)}\left(1 + \frac{0.5772}{2\ln(2f_n T)}\right)\sigma_N$$

This value can be used as the amplitude of the harmonic process, for instance for $T = 1h$ (expected maximum amplitude during a 1-hour-long simulation). For a narrow banded Gaussian process, the expected value of an arbitrary peak is given by $\sqrt{\pi/2}\,\sigma_N \approx 1.25\sigma_N$. Considering the example $f_n = 0.0456$ Hz and $T = 1h$, we have $A \approx 3.57\sigma_N$ which means that the amplitude of the harmonic process is chosen almost three times as large as the average amplitude.

3.4.1.4   Harmonic process with amplitude equal to a value with specified exceedance probability

The simulation of a single realization of the process can be approached through Monte Carlo simulation, by assuming that the realization can be composed as follows (see, e.g., [6] [7]):

$$N_n(t) = \sum_{k=1}^{N} c_k \cos(\omega_k t + \epsilon_k)$$

where c_k is a Rayleigh-distributed random amplitude, ϵ_k is a uniformly distributed random phase, that correspond to all discrete frequency components $\omega_1, \omega_2, \dots \omega_N$. By assuming that all the energy in the spectral density is focused at a single frequency component, the amplitude of the harmonic component is given by its Rayleigh distribution. The cumulative probability function of a Rayleigh distributed variable reads as follows:

$$F(x;\alpha) = 1 - e^{-x^2/(2\sigma_N^2)}$$

The value x_p with probability of exceedance $p = P[X > x_p]$ is therefore given as:

$$x_p = \sqrt{-2\sigma_N^2 \ln(p)}$$

Thus, the harmonic amplitude corresponding to an exceedance probability p is written as follows:

$$A = \sqrt{-2\ln(p)}\,\sigma_N \tag{4}$$

It should be noted that the exceedance probability p can also be interpreted as an exceedance probability for the terminal response level (provided $x_p > A_{cr}$). By rewriting

$$p = P[X > x_p] = P\left[3\pi\frac{X \cdot \hat{k}_g - 2c_{lin}\omega_n}{16c_{quad}\omega_n^2} > 3\pi\frac{x_p \cdot \hat{k}_g - 2c_{lin}\omega_n}{16c_{quad}\omega_n^2}\right] = P[y_0(X) > y_0(x_p)]$$

it is seen that the terminal response level $y_0(X)$ of a harmonic component with a Rayleigh distributed amplitude X has a probability p of exceeding the terminal level $y_0(x_p)$ corresponding to an amplitude $x_p = \sqrt{-2\ln(p)}\,\sigma_N$.

This formulation is the preferred one, which is why its results are emphasised in the succeeding sections. Herein, the value of p is chosen, in a crude and simplified manner, as $p = \frac{q_f}{q_{cond}}$, where q_f is the annual failure probability (chosen as 10^{-5}) and q_{cond} is the annual probability of the considered condition (e.g., 10^{-2} for a 100-year condition).

3.4.2   *Treatment of axial forces from wind sea and swell*

In [2], an uncertainty of 10% on the natural frequencies of both the mode generating the axial force and the mode being parametrically excited should be assumed. As Figure 3-5 indicates, for cases where the excitation is not located at the resonant frequency of a mode, the resulting response spectral density, representing, e.g., axial force, will not be mode-driven. Therefore, for cases excited by wind sea and swell, the combined uncertainty of the natural frequencies is concentrated at the frequency of the mode being parametrically excited. To avoid over-conservative estimates when conducting the simplified approach outlined above, the input spectral density is subdivided into several segments. All modes with frequency ratios of 0.5, 1.0 or 2.0 deviating less than 20% of any frequency within the suggested band of any segment are considered to have frequency ratio identical to 0.5, 1.0 and 2.0, respectively. The frequency bands are defined from the frequency corresponding to a numerical spectral density value equal to 5% (swell) or 10% (wind sea) of the value at the corresponding peak. A more optimal frequency band can be chosen based on the findings in Section 4.4, but this is not utilized at the current stage. Only the segment with the largest standard deviation of the relevant segments is used to assess the terminal level, as multiple segments are assumed to not be contributing at the same frequency. An example of a segmented spectral density is shown in Figure 3-6, for K11 exposed to 10000-year wind sea. The wind sea and swell axial forces are established using frequency-domain analyses in OrcaFlex.
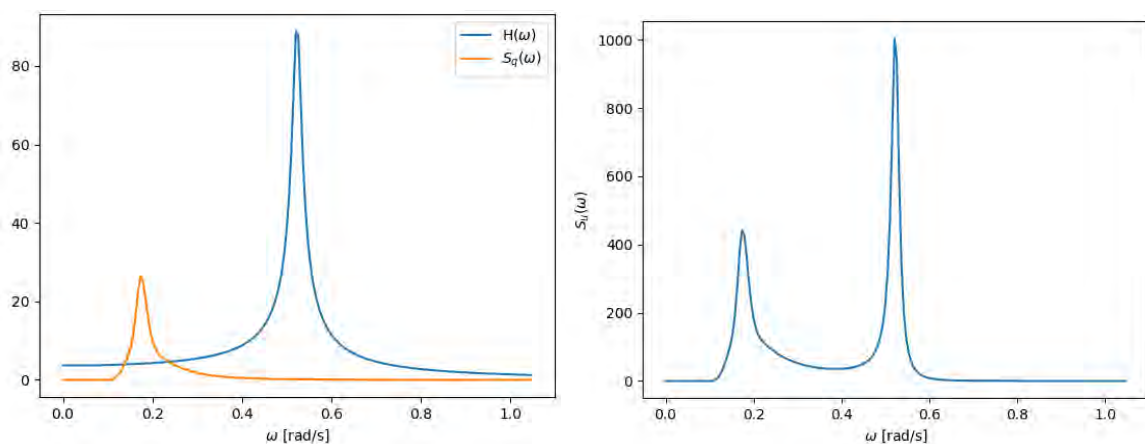

Figure 3-5. Spectral density of the response due to excitation in the tail of the frequency-domain transfer function.
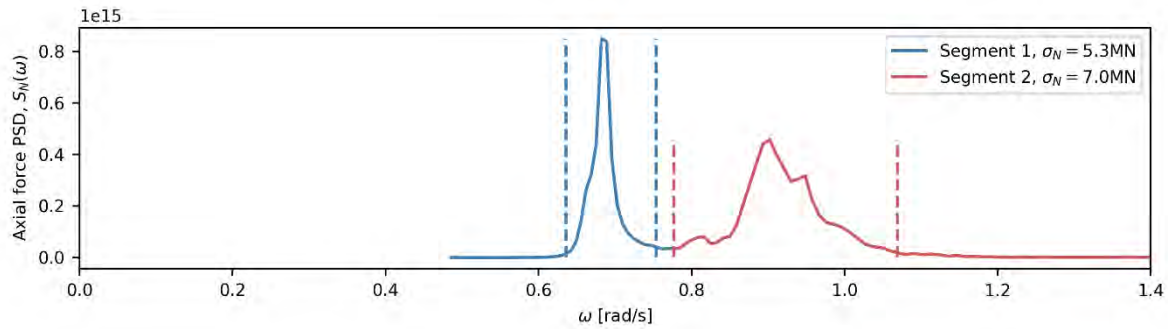
Figure 3-6. Spectral density of axial force variation on K11 due to 10000-year wind sea. The segment lines indicate what frequency ranges to consider for terminal level estimation.

3.4.3   Treatment of axial forces from wind

The above-described approach is equally valid for any source of excitation generating an axial force spectral density. However, the nature of the spectral density resulting from wind excitation makes a simplified approach possible.

Because the spectral density of wind excitation is typically decaying smoothly with respect to frequency due to its wide-bandedness, the frequency ratios of the natural frequencies are considered sufficient to study the parametric resonance; the frequency content of the forced vibration of a mode is considered to coincide quite closely to the resonant one. This is indicated in Figure 3-7.

By assessing all modes with natural frequency ratios of 0.5, 1.0, and 2.0, including an uncertainty of 10% on both values, as suggested in [2], the mode pairs likely to cause parametric resonance can be identified. The relevant mode pairs are visualized as a matrix showing all combinations and frequency ratios (cross-β matrix) as exemplified in Figure 3-8, showing the results for K11. The critical harmonic amplitudes were established for all triggered modes, and compared to the standard deviations of the applied axial force provided from a modal wind analysis in Novaframe.
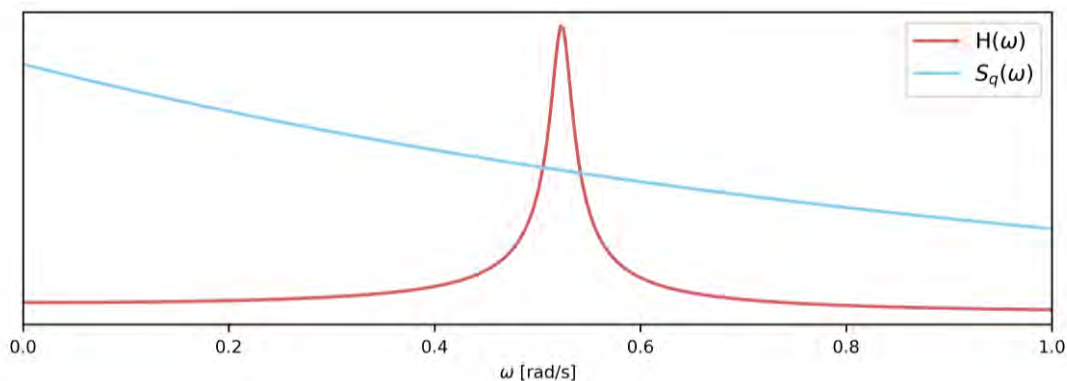

Figure 3-7. Example of an SDOF frequency-domain transfer, $H(\omega)$ and a wide banded excitation spectral density, $S_q(\omega)$, corresponding to a wind excitation.
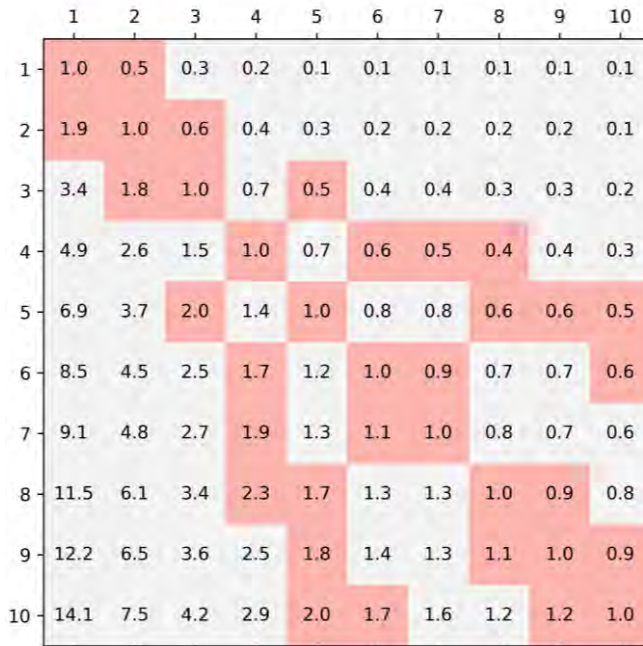
Figure 3-8. Cross-β matrix with ratios close to 0.5, 1.0 and 2.0 marked red. Example from K11.

3.5 Verification by Monte Carlo simulations

Monte Carlo simulations of the studied modes (SDOF systems) are used as a validation tool, to verify the results obtained from the simplified methods.

3.5.1 Effect of external forces

The external force applied in addition to the parameter variation shows to influence the resulting response in stochastic simulations drastically. It is therefore emphasised that this must be considered when assessing the bridges' proneness to parametric excitation. White noise, defined as a process with constant spectral density, was used because it is practical in a numerical set-up. However, the white noise merely acts as a generic stand-in for a real external load, such as wind or wave excitation. The effect is studied more in detail in Section 4.2.

3.5.2 Offsetting the response by the white noise response

By assuming that superposition is valid, the total response of the system could be assumed as follows:

$$y = y_{wn} + y_{pe} \Rightarrow y_{pe} = y - y_{wn}$$

where y_{wn} is the direct response from the white noise external forcing, and thus, y_{pe} is interpreted as the additional response resulting from the parametric excitation. Two approaches to estimate the maximum response from parametric excitation in a realization are used. The first of the approaches reads out as follows:

$$y_{pe,max} = \max(|y_{pe}|) = \max(y - y_{wn})$$

Alternatively, the extreme values can be estimated as follows:

$$y_{pe,max} = \max(|y|) - \max(|y_{wn}|)$$

For the cases where large response is induced from parametric excitation, the two approaches yield similar results. For the less drastic parametric excitation situations, where the white noise response is the largest contribution to the response, they clearly differ. The latter of the formulations can yield

negative net response from parametric excitation, which implies that the parameter variation has a destructive effect on the response. For these cases, the first approach will overestimate the response contribution from parametric excitation.

3.5.3   Relating the modal white noise spectral density amplitude to a physical quantity

The power spectral density of the external force was assumed to be characterized by a flat spectrum, indicating white noise, for the lateral components of all pontoons. This is depicted in Figure 3-9. The resulting modal forcing for mode n is established as:

$$S_q^* = \{\phi_n\}^T [S_q(\omega)]\{\phi_n\} = \{\phi_n\}^T S_0[I]\{\phi_n\} = S_0 \cdot \sum \phi_{n,i}^2$$

where $\{\phi_n\}$ is assumed to be mode shape corresponding to lateral displacements in a local coordinate system.
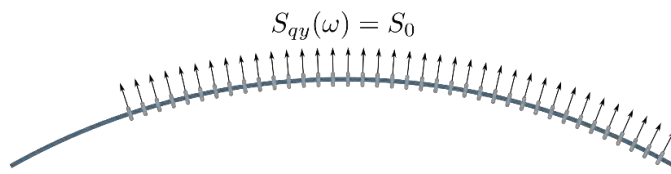

Figure 3-9. Constant amplitude of spectral density for transversal force on all pontoons.

3.5.4   Probabilistic treatment

By assuming that the parameter variation, lumped to a single harmonic component, has an amplitude that is Rayleigh distributed, as shown in Section 3.4.1, the exceedance probability can be related to the estimated terminal levels from Monte Carlo realizations. Ideally, the phenomenon should be treated in a complete probabilistic framework. A simplified treatment of the probabilities is conducted in the following; it is noted that this is introduced merely to assess the probability level.

The target annual failure (exceedance) probability is set to $q_f = 10^{-5}$, which gives a probability of failure within each realization of $p_f = \frac{q_f}{N_r}$, where N_r is the number of realizations in a year.

Furthermore, the annual probability corresponding to the applied axial force spectral density is denoted $q_{cond} = 1/R$, where R is the number of years in average between each occurrence of the condition. This is related to the following probability of it occurring in an arbitrary short-term condition: $p_{cond} = q_{cond}/N_{st}$, where N_{st} is the number of short-term conditions in a year. Multiple realizations are simulated based on a condition specified by an annual probability level q_{cond}. The exceedance probability in an arbitrary realization given the chosen condition is denoted p. The total probability of failure in each realization can be approximated as follows:

$$p_f = p_{cond} \cdot p$$

$$\Rightarrow \frac{q_f}{N_r} = \frac{q_{cond}}{N_{st}} \cdot p$$

$$\Rightarrow p = \frac{N_{st}}{N_r}\frac{q_f}{q_{cond}} = \frac{1\text{yr}/T_{st}}{1\text{yr}/T_r}\frac{q_f}{q_{cond}} = \frac{T_r}{T_{st}}\frac{q_f}{q_{cond}},$$

where T_r is the duration of each realization and T_{st} is the short-time duration corresponding to the specified condition. A choice of realization duration T_r larger than the short-term duration T_{st} might be needed in the Monte Carlo simulations to capture the parametric excitation.

Based on the equations given above, the response level exceeded in average by one out of $1/p$ realizations is interpreted as the response level with the specified annual probability of failure $q_f =$

10^{-5}. In this manner, the response due to conditions with different return period can be compared on similar grounds. As an example, a 10000-year axial load condition simulated with 3-hour realizations will correspond to $p = (3\text{hr}/1\text{hr}) \cdot (10^{-5}/10^{-4}) = 30\,\%$, whereas for a 100-year condition we have $p = (3\text{hr}/1\text{hr}) \cdot (10^{-5}/10^{-2}) = 0.3\,\%$. The more severe condition is thereby given a larger exceedance probability p. An illustration is given in Figure 3-10, where 10000 realizations are simulated for both a 100-year and a 10000-year axial load condition and the realization whose maximum is exceeded by a fraction p of the maximum values from the other realizations is shown. In both cases, the axial load maximum value with an annual exceedance probability 10^{-5} is estimated at 30 MN. It should be noted that although the adjustment of the probability yields very similar results for the maximum value, the results may differ more when the response due to the parameter variation is considered.
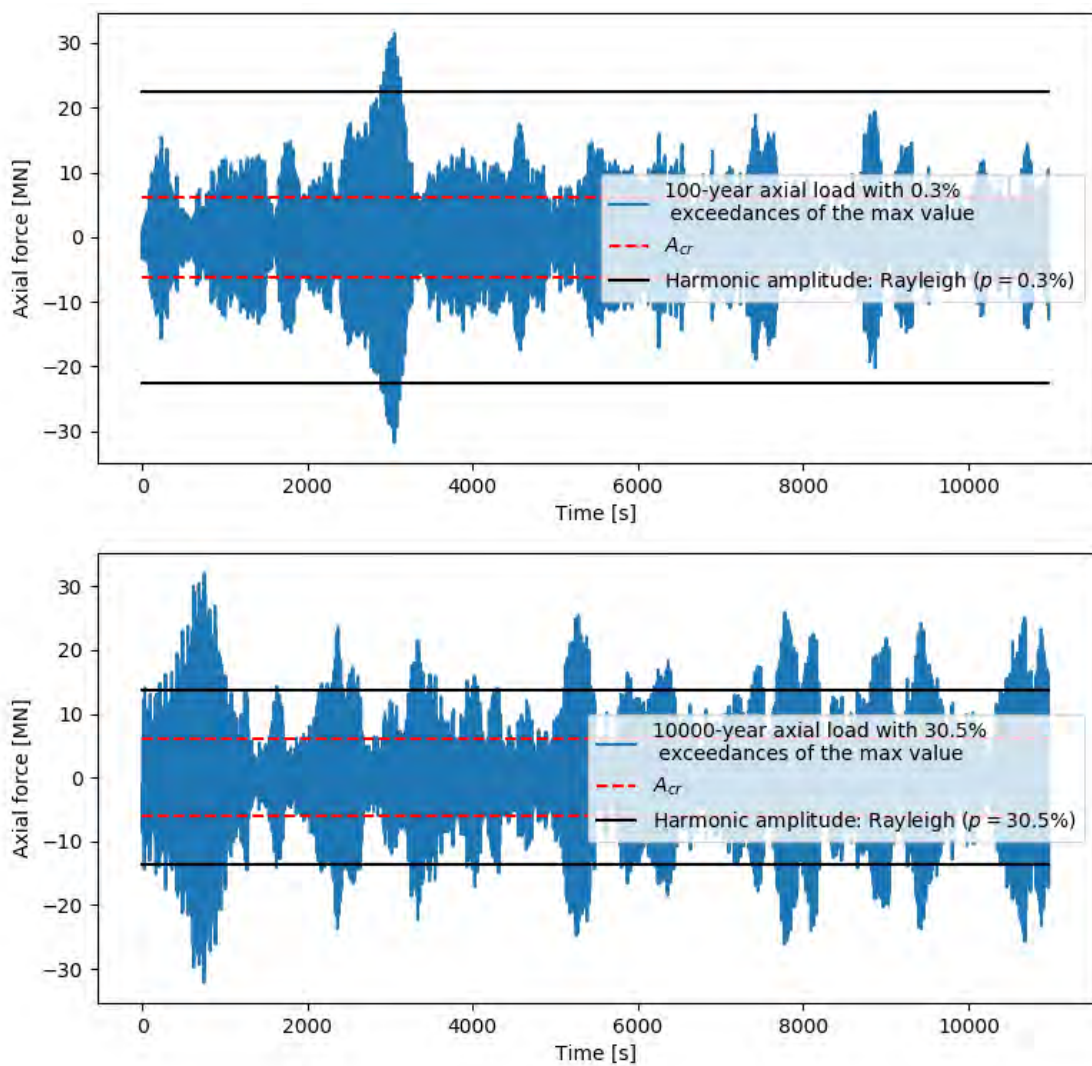

Figure 3-10. Realizations of axial load which correspond to an annual exceedance probability of 10^{-5} for the max value. A 100-year condition (upper) and a 10000-year condition (lower) is considered.

3.6 Establishing modal parameters

The modes of the full system, including hydrodynamic and aerodynamic frequency-dependent contributions to mass, damping and stiffness, can be solved according to the methodology in [8]. This relies on the solution of the complex eigenvalue problem, which does not assume anything about the damping in the system, and thus gives a more complete picture of the modes at play.

The modal analysis procedure is described in more detail in Appendix F, Section 6.2. The estimation procedures required to establish necessary modal parameters for the simplified methods are given in the two following sub-sections.

3.6.1 Modal quadratic damping

The quadratic drag force for a single component i can be written as follows:

$$f_{drag,i} = C_{quad,i} |\dot{u}_i| \dot{u}_i$$

For a body with effective cross-sectional area A_i, drag coefficient $C_{d,i}$ and water density ρ, the factor is given as follows:

$$C_{quad,i} = \frac{1}{2}\rho C_{d,i} A_i$$

The anchor line damping is provided as direct values of $C_{quad,i}$, based on the method presented in Appendix F, Enclosure 2. By assuming that the drag forces are independent of each other, i.e., that the quadratic drag damping matrix is diagonal, it can be simplified as follows:

$$\{f_{drag}\} = [C_{quad}]\mathrm{diag}(\{|\dot{u}|\})\{\dot{u}\}$$

where $\left[C_{quad}\right] = \mathrm{diag}(C_{quad,i})$ is a diagonal matrix describing the coefficients for all relevant degrees of freedom (DOFs). For a single-mode motion described by $\{u_n\} = \{\phi_n\}y_n$; where $\{u_n\}$ are the relevant physical DOFs, $\{\phi_n\}$ the mode shape of the selected mode, and y_n is the generalized coordinate of the selected mode; this can be rewritten as:

$$\{f_{drag}\} = [C_{quad}]\mathrm{diag}(\{|\phi_n|\})|\dot{y}_n|\{\phi_n\}\dot{y}_n$$

The modal contribution, $\tilde{f}_{drag,n} = \{\phi_n\}^T\{f_{drag}\}$, is furthermore computed as follows:

$$\tilde{f}_{drag,n} = c_{quad,n}|\dot{y}_n|y_n$$

$$= \{\phi_n\}^T[C_{quad}]\mathrm{diag}(\{|\phi_n|\})\{\phi_n\}|\dot{y}_n|\dot{y}_n$$

which implies that the modal quadratic damping coefficient can be established by the following expression:

$$c_{quad,n} = \{\phi_n\}^T[C_{quad}]\mathrm{diag}(\{|\phi_n|\})\{\phi_n\}$$

Furthermore, an equivalent linear damping per cycle of a harmonic motion can be established through:

$$c_{quad,n,eq} = c_{quad,n}|\dot{y}_{n,0}| \cdot \frac{8}{3\pi}$$

Or, since $|\dot{y}_n| = |y_n|\omega_d$:

$$c_{quad,n,eq} = c_{quad,n}|y_{n,0}|\omega_d \cdot \frac{8}{3\pi}$$

The procedure given above is verified in Enclosure 3.

3.6.2   Geometric stiffness estimation

The geometric element stiffness is approximated in a self-developed code as follows:

$$[k_{11}] = \begin{bmatrix} 0 & 0 & 0 & 0 & 0 & 0 \\ 0 & \frac{6}{5} & 0 & 0 & 0 & \frac{L}{10} \\ 0 & 0 & \frac{6}{5} & 0 & -\frac{L}{10} & 0 \\ 0 & 0 & 0 & 0 & 0 & 0 \\ 0 & 0 & -\frac{L}{10} & 0 & \frac{2L^2}{15} & 0 \\ 0 & \frac{L}{10} & 0 & 0 & 0 & \frac{2L^2}{15} \end{bmatrix}, [k_{12}] = \begin{bmatrix} 0 & 0 & 0 & 0 & 0 & 0 \\ 0 & -\frac{6}{5} & 0 & 0 & 0 & \frac{L}{10} \\ 0 & 0 & -\frac{6}{5} & 0 & -\frac{L}{10} & 0 \\ 0 & 0 & 0 & 0 & 0 & 0 \\ 0 & 0 & \frac{L}{10} & 0 & \frac{2L^2}{15} & 0 \\ 0 & -\frac{L}{10} & 0 & 0 & 0 & -\frac{2L^2}{15} \end{bmatrix}, [k_{22}] = \begin{bmatrix} 0 & 0 & 0 & 0 & 0 & 0 \\ 0 & \frac{6}{5} & 0 & 0 & 0 & -\frac{L}{10} \\ 0 & 0 & \frac{6}{5} & 0 & \frac{L}{10} & 0 \\ 0 & 0 & 0 & 0 & 0 & 0 \\ 0 & 0 & \frac{L}{10} & 0 & \frac{2L^2}{15} & 0 \\ 0 & -\frac{L}{10} & 0 & 0 & 0 & \frac{2L^2}{15} \end{bmatrix}$$

$$[k_g] = \frac{N}{L} \begin{bmatrix} [k_{11}] & [k_{12}] \\ [k_{12}]^T & [k_{22}] \end{bmatrix}$$

and is established with a unit axial force $N = 1$, which implies $[k_g] = [\hat{k}_g]$, for all elements in the girder of the bridge concepts. The global matrix $[K_g]$ is furthermore established after transforming to global coordinates and summing all the contributions. The resulting modal geometric stiffness is finally established straightforwardly through $[K_g^*] = [\phi]^T[K_g][\phi]$, where $[\phi]$ is the full total modal transformation matrix resulting from the eigenvalue solution.

The calculation of the geometric stiffness was verified by comparing the ratio $k/\hat{k}_g$ with results from the RM Bridge-model of K11, based on applying a constant axial force in the girder. The ratio can be shown to be expressed as follows:

$$\frac{k}{\hat{k}_g} = \frac{N}{1 - \alpha^2}, \qquad \alpha = \frac{\omega_{mod}}{\omega_{ref}}$$

where ω_{ref} is the circular frequency without any axial force and ω_{mod} is the corresponding frequency with an applied constant axial force N, respectively, for the mode of interest. The resulting ratio is compared with the result obtained directly for various axial forces applied in the RM Bridge model in Figure 3-11.
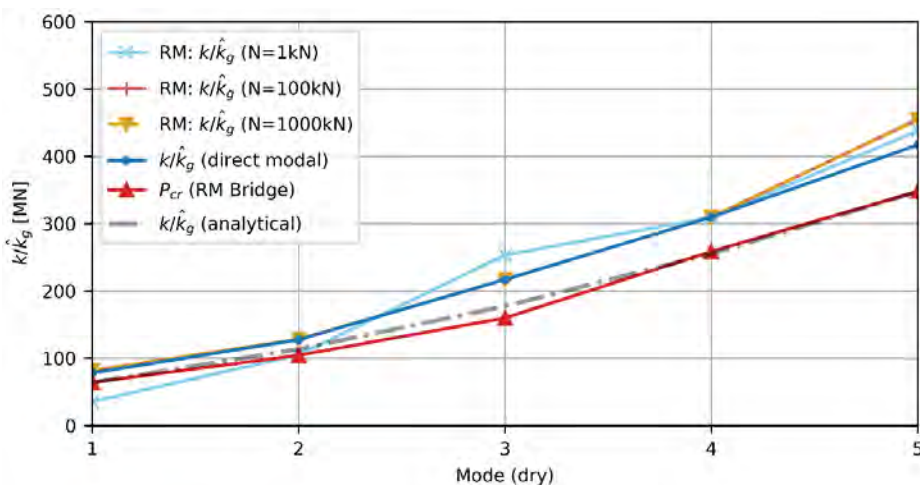

Figure 3-11. Verification of $k/\hat{k}_g$ for the first five dry modes of K11.

4 Important special topics

4.1 Assessment of the validity of modal decoupling

As described in more detail in Appendix G, Section 6.2, the full damping of the systems is non-classical, implying non-diagonal modal damping matrices. This causes the resulting modes, both eigenvalues and eigenvectors, to become complex-valued. It is therefore important to critically evaluate how diagonal the matrices are before conducting analyses based on the modal solution. The referred section indicates that all modes considered for parametric excitation is close to fully decoupled, which allows for a traditional mode-by-mode approach.

4.2 Effect of external force amplitude

The amplitude of the external force $p(t)$ shown in Equation 2 affects the response triggered by parametric excitation. The external force is defined as a white noise process, i.e., with a constant power spectral density with a given constant spectral density value or a standard deviation (result will depend on frequency axis used). The external noise is not solely a fictious source to induce the instability; it could represent a real-life excitation as well, with wind excitation as an obvious example. Increasing the white noise amplitude has three effects:

- Larger amplitude in most realizations for stochastic simulations

- Systems exposed to stochastic parameter variation shows an improved fit to the Gumbel distribution, and is more well-behaved

- The largest amplitude occurs earlier for harmonic cases and is more evenly distributed, meaning it is not more likely to occur after a certain time

The topic is more discussed in the following sub-sections.

4.2.1 Harmonic parameter variation

First, the effect of external excitation on top of a harmonic parameter variation is considered. Figure 4-1 shows the response of a system similar to mode 4 of K11, exposed to a selected harmonic parameter variation and an external harmonic excitation with four different amplitudes. It is obvious that the response amplitude is not affected by the external force (other than the direct response from it). However, the response build-up happens faster for a system with larger external force. To verify the observed effects in the SDOF analyses, an OrcaFlex model of K11 was exposed to a modal load of the triggered mode 4 together with the regular waves with twice the frequency, causing parametric excitation, where the hydrodynamic damping and added mass were both simplified as *in*dependent of frequency. The modal load at each pontoon was set to $A = 0kN$ and $A = 4kN$ with the individual pontoons' sway mode shape amplitude. Figure 4-2 and Figure 4-3 show the axial force, bending moments and transverse displacement for a modal force of 0kN and 4kN, respectively. The envelopes of maximum displacement for all analyses conducted are shown in Figure 4-4. The plots indicate that the direct external force does not affect the maximum response, but does affect the time of its occurrence, as for the SDOF analyses.
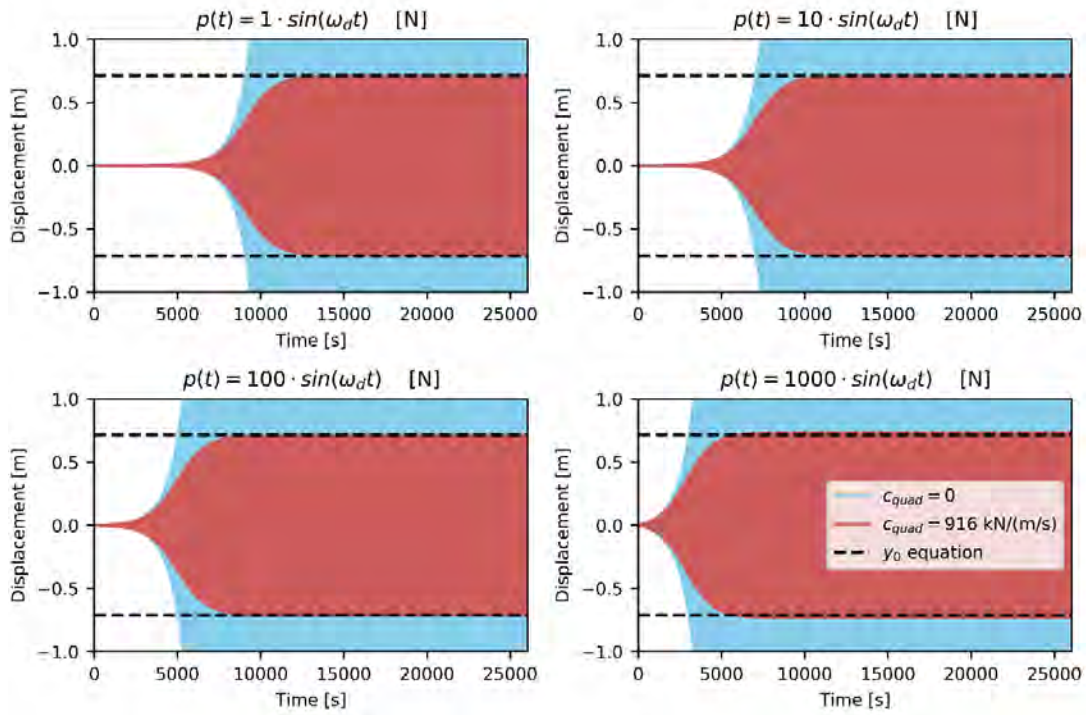
Figure 4-1. SDOF simulations with various external harmonic excitation amplitudes.
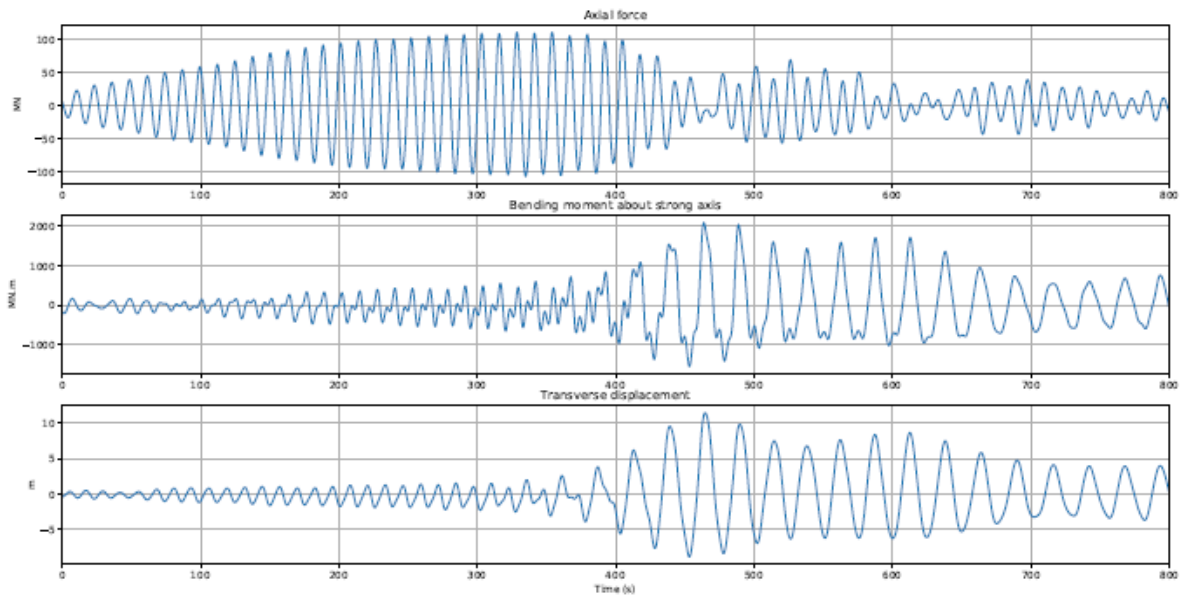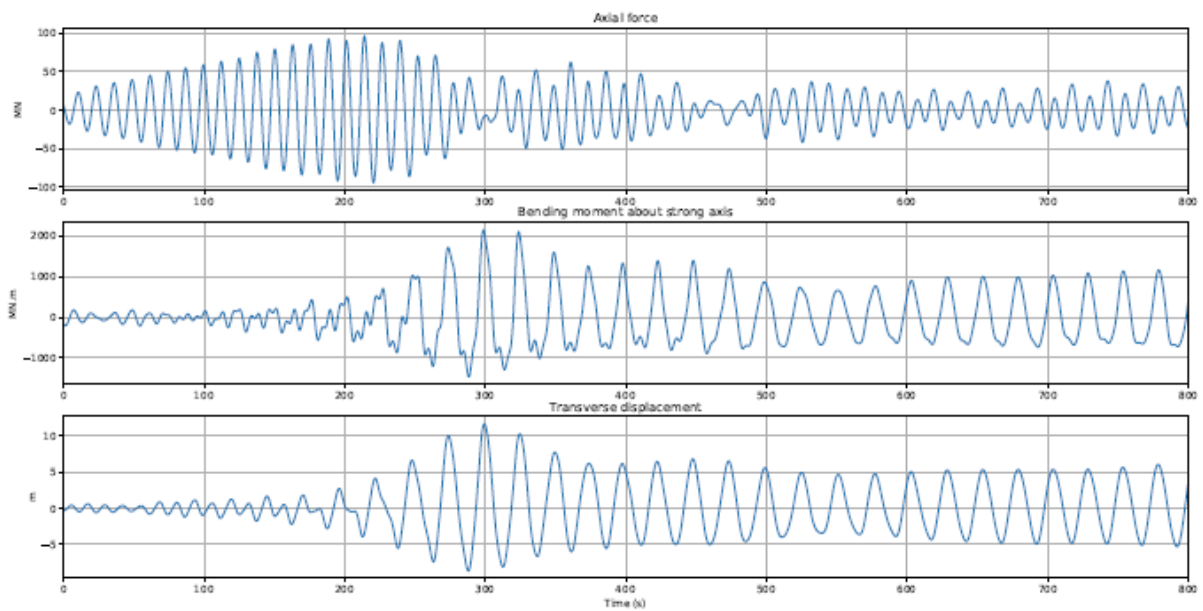

Figure 4-2. $A = 0$.

Figure 4-3. $A = 4.0\ kN$.
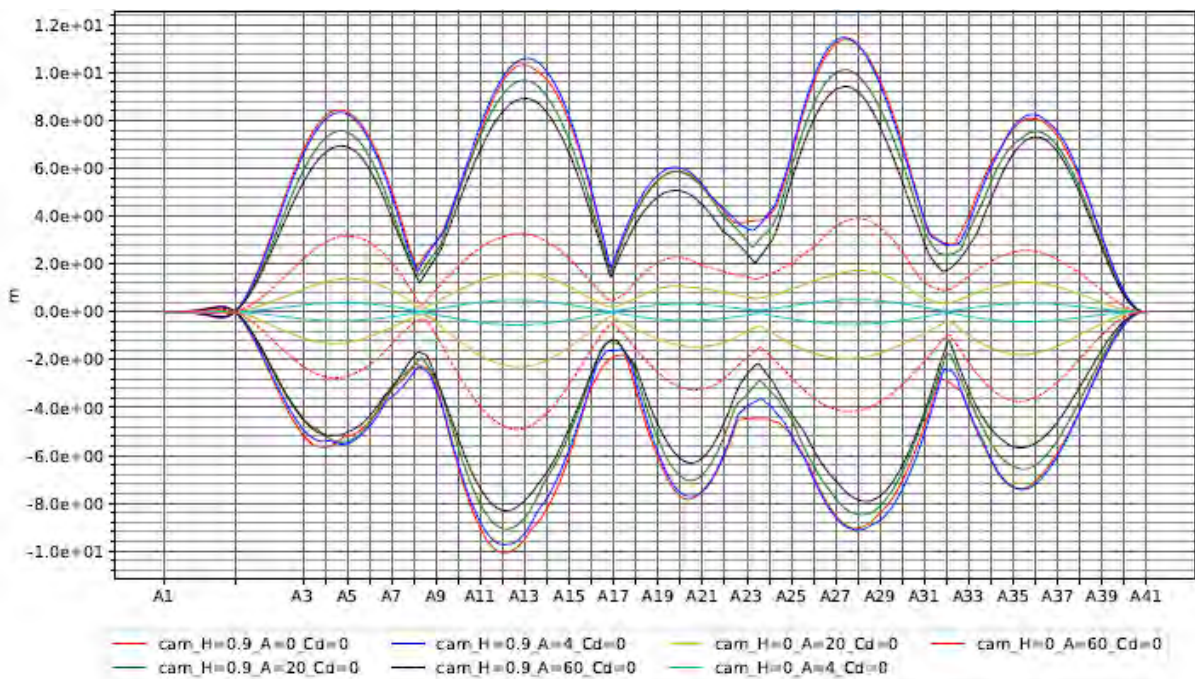
Figure 4-4. Envelopes showing the maximum displacement along the bridge girder for different external (modal) excitation amplitudes. The value A in the legend refers to the amplitude of the modal load. H refers to the wave height of the regular wave, at twice the frequency of the triggered mode 4, causing parametric excitation.

4.2.2   Stochastic parameter variation

To assess the effect of external force amplitude on a system exposed to stochastic parameter variation, mode 4 of K11 was used as an example. The properties of mode 4 of K11 are given in Table 6-1. The axial force response is estimated using the global analysis OrcaFlex model and a 10000-year swell condition; the resulting axial force response is described by the spectral density in Figure 4-5. Six different amplitudes of white noise external forcing are simulated, characterized by six different constant spectral density levels. Figure 4-6 shows the resulting Gumbel probability paper for the increase of maximum response due to parametric excitation. The figure reveals that the additional

maximum response is growing for an increased external white noise, until a certain level, where it drops again. At this level, the white noise is dominating the response, and is not really representing realistic or reasonable conditions. It is apparent that by increasing the external white noise, the system becomes more well-behaved with respect to the parameter variation, and the Gumbel fit (linear trend, not indicated by fit) is improved drastically. By applying a white noise process, the system will act as a filter, to yield a response with energy around the natural frequency of the system; the system appears to be pushed into resonance. Also, the likelihood of the next realization being much worse than the previous ones is reduced by doing so; the process appears to be more predictable and less sensitive to small variations in the realization.

To verify this result, similar analyses are conducted in OrcaFlex. A selected realization of a 10000-year swell condition with and without white noise is shown in Figure 4-7. No direct specification of the amplitude of the white noise amplitude used in OrcaFlex is given, for compactness, because its definition in OrcaFlex is not straightforward; however, it may be inferred from the amplitude of the white noise response. The selected realization from the global analysis model indicates an increase of the maximum response by a factor close to four (from 0.5 metres to 2.0 metres) from the introduction of the external white noise, which qualitatively supports the findings from the SDOF analyses.

In sum, the response due to parametric excitation is highly dependent on the external force applied directly to the mode being triggered and must therefore be carefully considered before relying on the results from predictions. Also, the system is seemed to behave more predictably under such circumstances. It is worth noting that it appears more challenging to select proper white noise excitation levels for cases barely being parametrically excited.
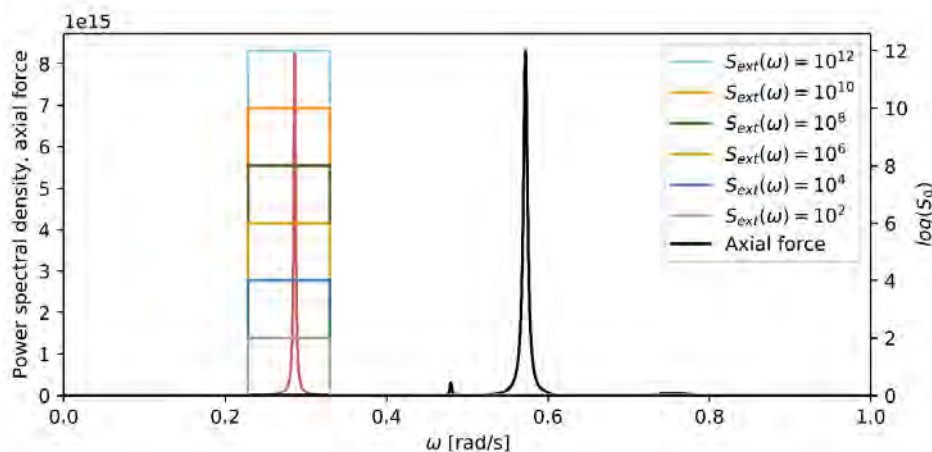
Figure 4-5. Axial force spectral density, due to a 10000-year swell condition on K11 and the square of the transfer function of mode 4, together with various levels of white noise excitation. The spectral density of the axial force is adjusted such that the peak is located at two times the frequency of the natural frequency of the mode. Note that the power spectral density of the axial force is corresponding to the left side axis, whereas the external white noise excitation is corresponding to the right-side, logarithmic, axis.
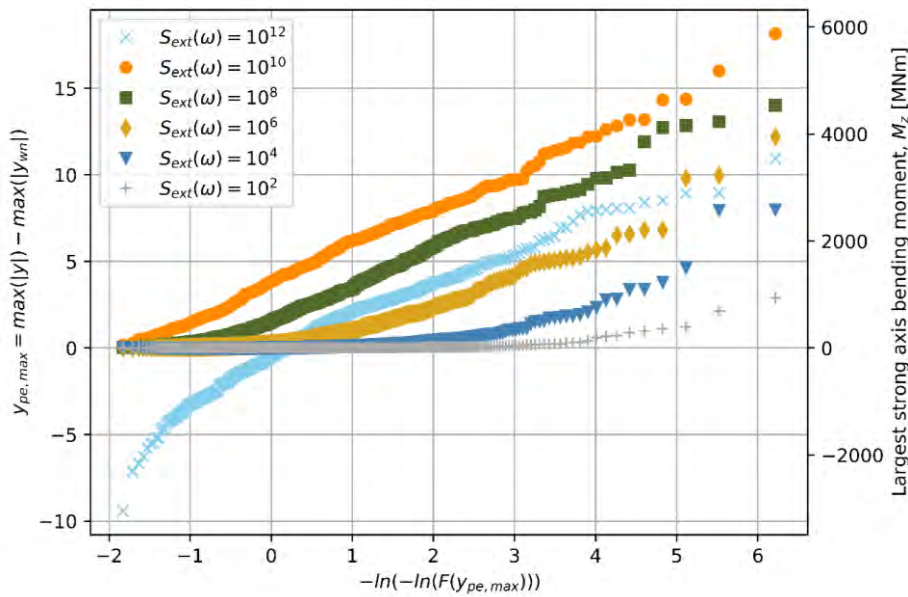
Figure 4-6. Gumbel probability paper for 500 realizations with varying external white noise excitation amplitudes. The colours correspond to the levels shown in Figure 4-5.
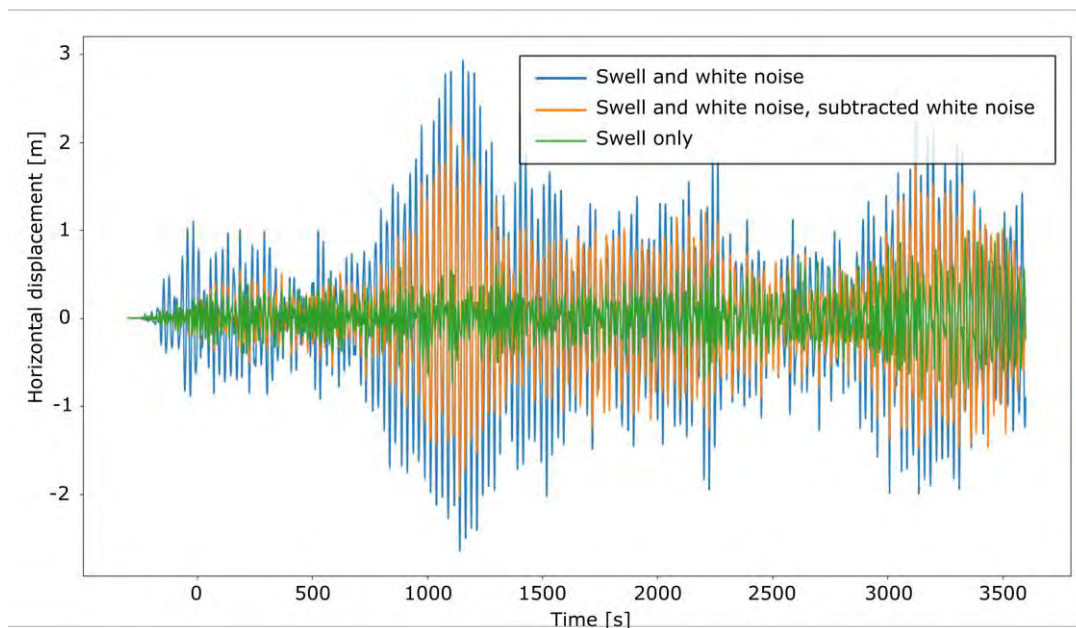
Figure 4-7. Selected realization from OrcaFlex with 10000-year swell conditions and external white noise.

4.3   Comparison between single-degree-of-freedom response and OrcaFlex response

Figure 4-8 and Figure 4-9 show axial force variations and the resulting displacements in the bridge girder of K11 due to a harmonic wave simulated in OrcaFlex, with drag coefficient 0.4 and regular wave heights 1.8m and 2.7m, respectively. Figure 4-10 shows the similar plots for drag coefficient 1.0 and regular wave height 2.7m. The figures furthermore show the simulated SDOF responses due to the axial force variation characterized by the (lowpass-filtered) axial force response from OrcaFlex. An external white noise force is also applied to the SDOF system. The axial force variation results in excitation of mode 4, which is half the frequency of the applied axial force. It is clear that the axial force induced initially drops when the parametric excitation initiates, and the energy of the system is moved from modes around the wave excitation frequency to the parametrically excited mode 4. By

assuming that the linear axial force response (prior to response drop) is applied to the mode to be parametrically excited, too large response will be predicted; this is thus deemed to be a conservative approach. When applying the stationary or steady-state axial force variation simulated in OrcaFlex, the response levels in the global analysis model and the SDOF model (defined by the modal parameters of mode 4 from the global analysis model) are on the safe side for the usage of an SDOF model.
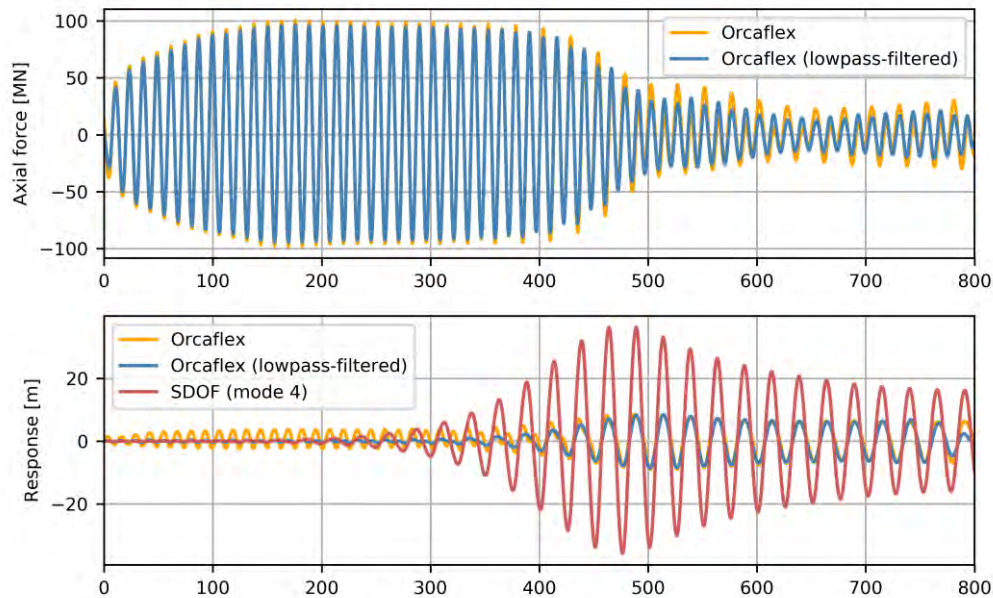

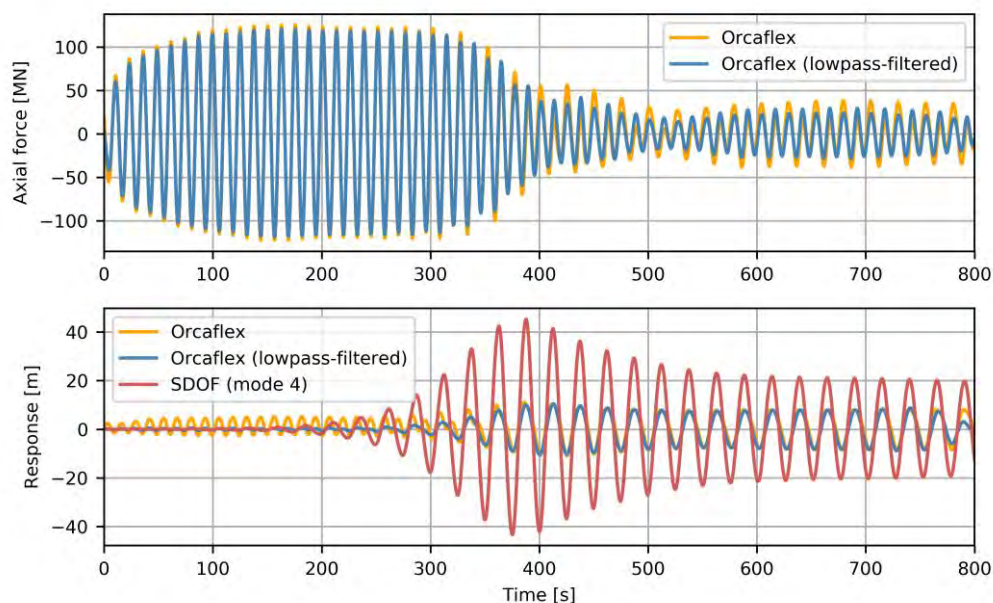*Figure 4-8. $C_d = 0.4$ and harmonic amplitude $H = 1.8m$.*

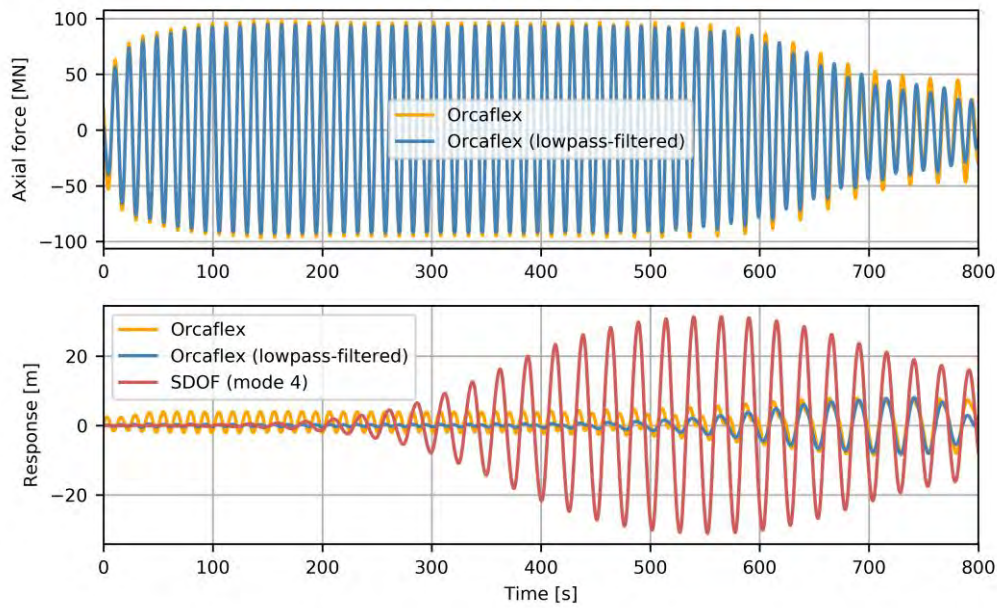*Figure 4-9. $C_d = 0.4$ and harmonic amplitude $H = 2.7m$.*

Figure 4-10. $C_d = 1.0$ and harmonic amplitude $H = 2.7m$.

4.4 Effect of wide-bandedness

4.4.1 Tri-harmonic representation of the parameter variation

In order to investigate the effect of wide-bandedness, the stochastic axial force variation can be approximated as a sum of three harmonic components at frequencies ω_1, ω_2 and ω_3:

$$N(t) = U_1\sigma_1 \cos(\omega_1 t) + U_2\sigma_2 \cos(\omega_2 t) + U_3\sigma_3 \cos(\omega_3 t) \qquad (5)$$
$$+U_4\sigma_1 \sin(\omega_1 t) + U_5\sigma_2 \sin(\omega_2 t) + U_6\sigma_3 \sin(\omega_3 t)$$

The spectral density $S_N(\omega)$ of the axial force is then segmented into three parts, as illustrated in Figure 4-11 and Figure 4-12 for a narrow and wide banded spectrum, respectively. The variance σ_N^2 is thereby divided into three parts:

$$\sigma_N^2 = \int_0^\infty S_N(\omega)d\omega = \int_0^{\omega_1} S_N(\omega)d\omega + \int_{\omega_1}^{\omega_3} S_N(\omega)d\omega + \int_{\omega_3}^\infty S_N(\omega)d\omega = \sigma_1^2 + \sigma_2^2 + \sigma_3^2.$$

The frequencies ω_1, ω_2 and ω_3 of the harmonic components are placed as close to $2\omega_d$ as possible within each part, i.e. at $\omega_1 = 2\omega_d - \Delta\omega$, $\omega_2 = 2\omega_d$ and $\omega_3 = 2\omega_d + \Delta\omega$ where $\Delta\omega$ is varied. The coefficients $U_1, U_2, U_3, U_4, U_5, U_6$ are independent standard normal random variables, such that the axial force variation $N(t)$ as given by Equation 5 represents a Gaussian stochastic process. Realizations of the stochastic process can then be obtained by drawing $U_1, U_2, U_3, U_4, U_5, U_6$ from a standard normal distribution.

The response of the SDOF system can be obtained for a given realization of $N(t)$ by solving the equation of motion with a small initial displacement (0.001 m) and no external load. Examples of realizations of the axial load $N(t)$, along with the corresponding responses, are shown in Figure 4-13 and Figure 4-14 for the spectra given in Figure 4-11 and Figure 4-12, respectively. It appears that also in the tri-harmonic case, the response reaches a terminal level y_0 when the axial force is sufficiently large.
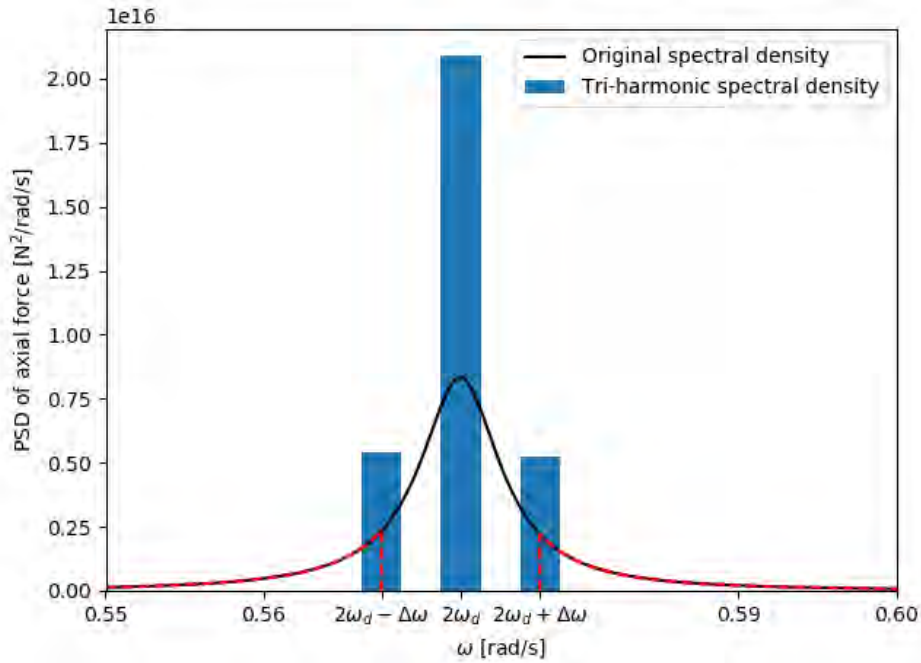
Figure 4-11 Narrow banded spectrum ($\Delta\omega = 0.005\ rad/s$): The power spectral density of the axial force is segmented into three parts which are placed at different frequencies as illustrated by the bars.
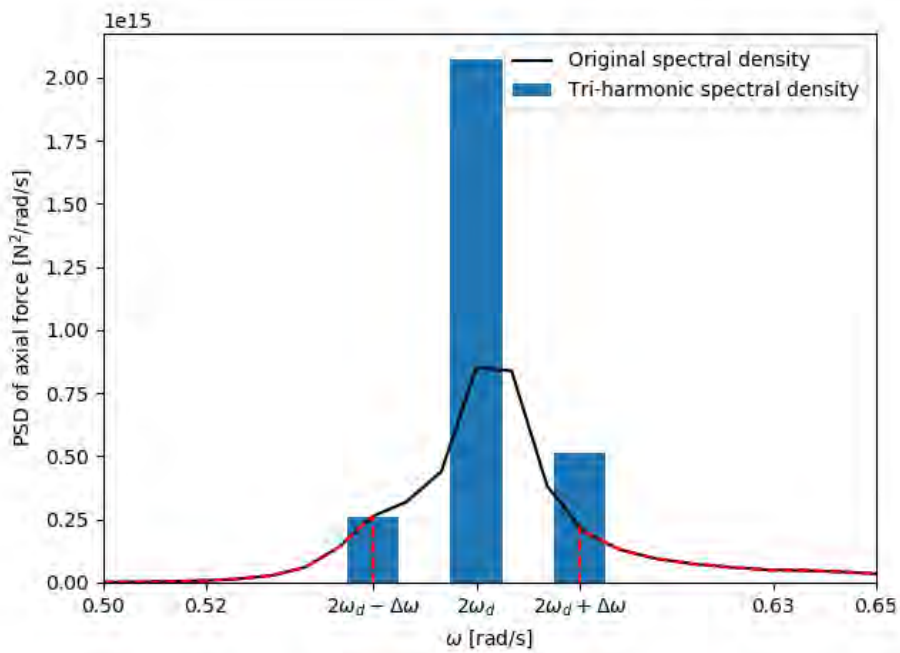
Figure 4-12 Wide banded spectrum ($\Delta\omega = 0.02\ rad/s$): The power spectral density of the axial force is segmented into three parts which are placed at different frequencies as illustrated by the bars.

Figure 4-13 Narrow banded spectrum ($\Delta\omega = 0.005\ rad/s$): An example of a realization of the axial force, along with the corresponding response. Note the different time axes in the plots.
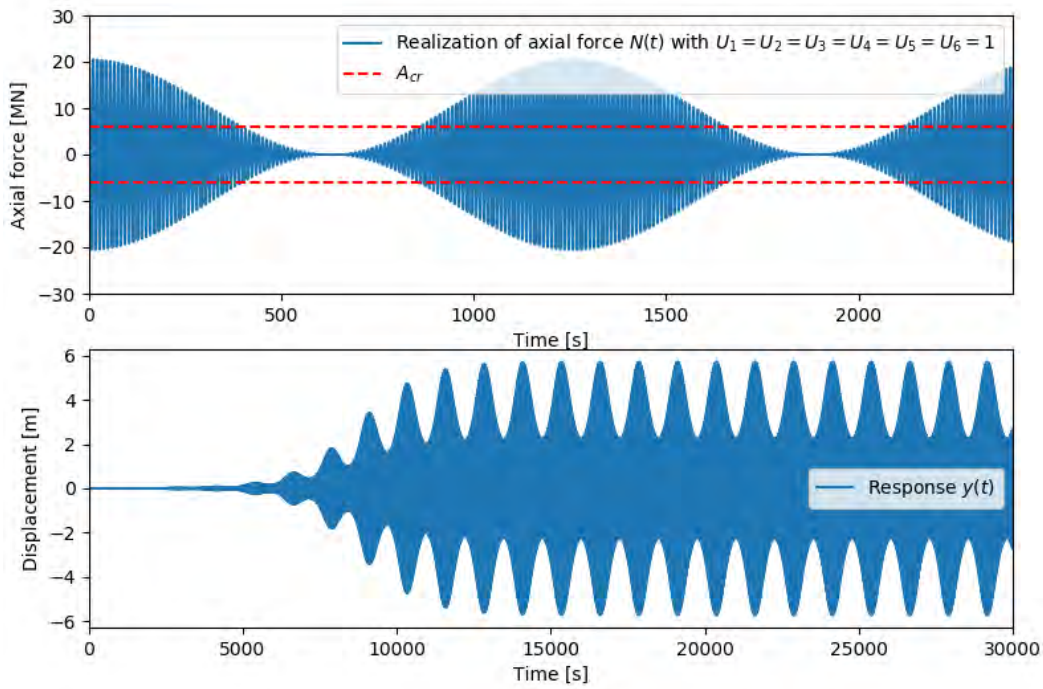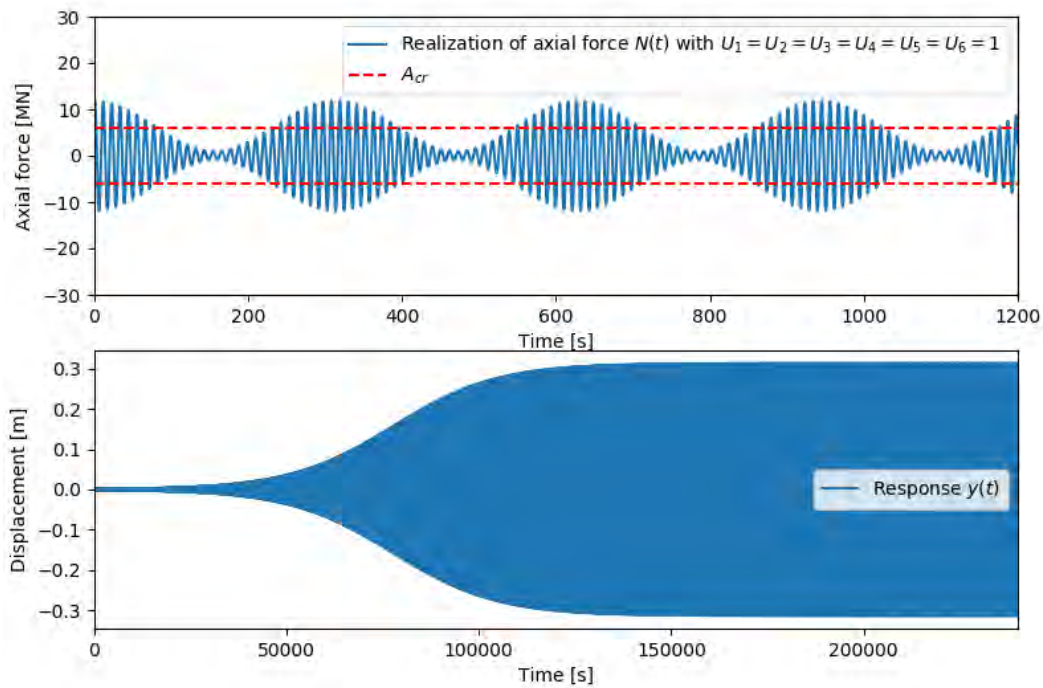

Figure 4-14 Wide banded spectrum ($\Delta\omega = 0.02\ rad/s$): An example of a realization of the axial force, along with the corresponding response. Note the different time axes in the plots.

4.4.2 Estimating terminal response level for tri-harmonic parameter variation

The terminal response level will depend on the amplitudes of the harmonic components, and we assume that it is given by a function $y_0(U_1, U_2, U_3, U_4, U_5, U_6)$. The terminal response level y_p with a specified exceedance probability p is given by the equation

$$P[y_0(U_1, U_2, U_3, U_4, U_5, U_6) > y_p] = p.$$

Using an IFORM (inverse first-order reliability method) approach, approximating $y_0(U_1, U_2, U_3, U_4, U_5, U_6)$ by a linear function, the level y_p can be estimated by solving the constrained optimization problem

$$y_p \approx \max y_0(U_1, U_2, U_3, U_4, U_5, U_6), \text{ subject to } U_1^2 + U_2^2 + U_3^2 + U_4^2 + U_5^2 + U_6^2 = \beta_{IFORM}^2,$$

where $\beta_{IFORM}^2 = -\Phi^{-1}(p)$ with $\Phi(\cdot)$ being the standard normal cumulative distribution function (CDF). This means that y_p is estimated by the largest terminal response level obtained when the amplitudes of the harmonic components are limited by the constraint $U_1^2 + U_2^2 + U_3^2 + U_4^2 + U_5^2 + U_6^2 = \beta_{IFORM}^2$ corresponding to the specified probability p.

In general, it is difficult to conclude whether the linear approximation in the IFORM approach gives an under- or overestimation of the level y_p. In this case, however, it appears that the IFORM approach can give a rather large underestimation of the response level. This can be seen by considering the special case where $\Delta\omega \to \infty$, i.e. $\sigma_1 = \sigma_3 = \sigma_4 = \sigma_6 = 0$. This corresponds to the harmonic case

$$N(t) = U_2 \sigma_N \cos(\omega_2 t) + U_5 \sigma_N \sin(\omega_2 t) = \sqrt{U_2^2 + U_5^2}\, \sigma_N \cos(\omega_2 t + \epsilon(U_2, U_5)),$$

and the terminal response level is given as

$$y_0(U_1, U_2, U_3, U_4, U_5, U_6) = 3\pi \frac{\sqrt{U_2^2 + U_5^2}\, \sigma_N \cdot \hat{k}_g - 2c_{lin}\omega_n}{16c_{quad}\omega_n^2}.$$

Since U_2 and U_5 are standard normal random variables, the amplitude $\sqrt{U_2^2 + U_5^2}\, \sigma_N$ will be Rayleigh distributed, and the terminal response level y_p can be found exactly as the terminal response corresponding to an amplitude $\sqrt{U_2^2 + U_5^2}\, \sigma_N = \sqrt{-2\ln(p)}\, \sigma_N$. Using the IFORM approach, on the other hand, would give the constraint $U_2^2 + U_5^2 = \beta_{IFORM}^2$, and the estimate of y_p would correspond to and amplitude $\sqrt{U_2^2 + U_5^2}\, \sigma_N = \beta_{IFORM}^2 \sigma_N = -\Phi^{-1}(p)\sigma_N$. The IFORM amplitude is smaller than the Rayleigh amplitude ($p = 0.3$ gives $-\Phi^{-1}(p) = 0.524$ and $\sqrt{-2\ln(p)} = 1.55$), and IFORM therefore underestimates the terminal response level.

An improvement of the linear approximation in the IFORM approach can be obtained by approximating the tri-harmonic terminal response level $y_0(U_1, U_2, U_3, U_4, U_5, U_6)$ by a function of the form $\bar{y}_0\left(\sqrt{U_2^2 + U_5^2}\right)$. Using this simplification, the estimate of y_p is obtained in the exact same manner as for the IFORM approach, with a slightly modified optimization problem

$$y_p \approx \max y_0(U_1, U_2, U_3, U_4, U_5, U_6), \text{ subject to } U_1^2 + U_2^2 + U_3^2 + U_4^2 + U_5^2 + U_6^2 = \beta_{Rayleigh}^2,$$

where $\beta_{Rayleigh} = \sqrt{-2\ln(p)}$.

The optimization problem was solved iteratively, using an initial guess given by U_4, U_5 or U_6 equal to $\beta_{Rayleigh}$ (and $U_i = 0$ for the other five), depending on which gave the largest response. In Figure 4-15 and Figure 4-16, examples of the maximal terminal response and corresponding axial force are shown for the spectra given in Figure 4-11 and Figure 4-12.

Figure 4-15 Narrow banded spectrum ($\Delta\omega = 0.005\ rad/s$): The maximum terminal response corresponding to the probability level $p = 0.3$ ($\beta = \beta_{Rayleigh} = 1.55$), and the maximizing axial force.
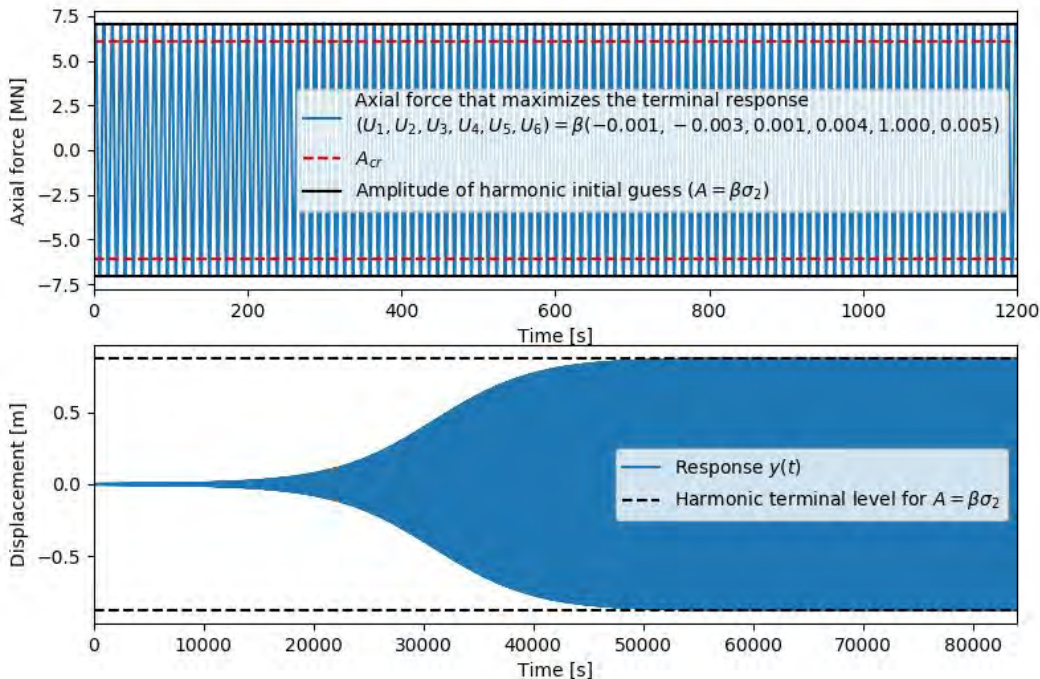
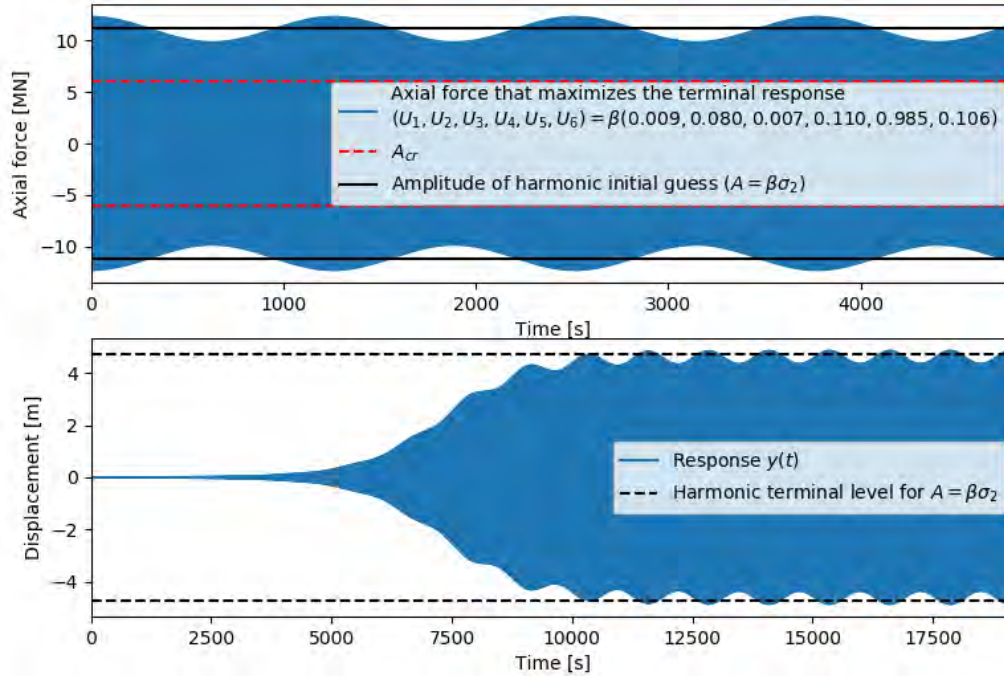*Figure 4-16 Wide banded spectrum ($\Delta\omega = 0.02\ rad/s$): The maximum terminal response corresponding to the probability level $p = 0.3$ ($\beta = \beta_{Rayleigh} = 1.55$), and the maximizing axial force.*

4.4.3   Effect of varying $\Delta\omega$ in the tri-harmonic representation of the parameter variation

The terminal response values corresponding to a probability level $p = 0.3$ for different values of $\Delta\omega$ obtained are shown in Figure 4-17 for the narrow-banded spectrum given in Figure 4-11. It is seen that the terminal response is reduced compared to the harmonic case, and the reduction depends strongly on the value of $\Delta\omega$. Considering the harmonic terminal level from an amplitude of $A = \beta\sigma_2$ (i.e. only the centre part of the spectrum in Figure 4-11 is included), we see that this will provide a good estimate of the tri-harmonic terminal level for $\Delta\omega$ above a certain level. Similarly, the terminal response values corresponding to a probability level $p = 0.3$ for different values of $\Delta\omega$ obtained are shown in Figure 4-17 for the wide banded spectrum given in Figure 4-12. In this case we also observe a reduction of the terminal response, and the effect of using a tri-harmonic approximation is larger compared to the narrow-banded case. For the points in Figure 4-18 that appear to have zero terminal response, the initial displacement of 0.001 m is either never exceeded or only slightly amplified due to the parametric excitation, and the response never reaches a terminal response level. Also, for the wide banded case we see that the harmonic terminal level from an amplitude $A = \beta\sigma_2$ can be used to predict the terminal response for $\Delta\omega$ above a certain level. This indicates that the part of the spectrum that is located outside some frequency band can be neglected when the terminal response is determined.

Figure 4-17 Narrow banded spectrum: The maximum terminal response corresponding to the probability level $p = 0.3$ ($\beta = \beta_{Rayleigh} = 1.55$) for different values of $\Delta\omega$.

Figure 4-18 Wide banded spectrum: The maximum terminal response corresponding to the probability level $p = 0.3$ ($\beta = \beta_{Rayleigh} = 1.55$) for different values of $\Delta\omega$.
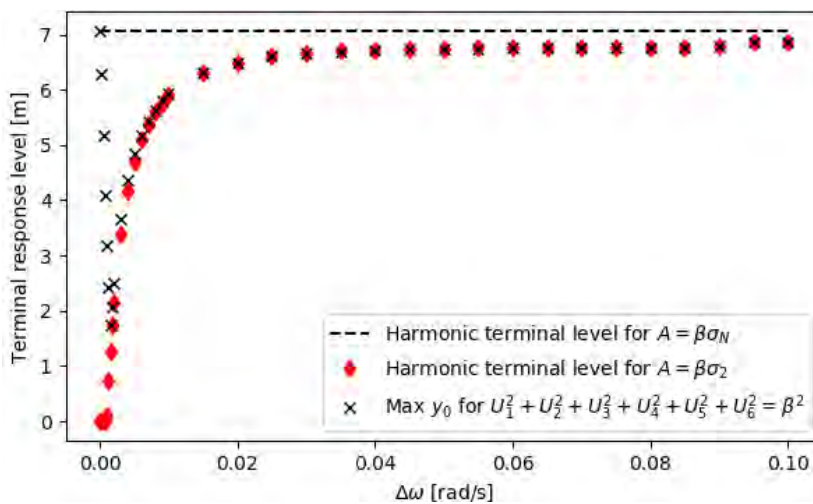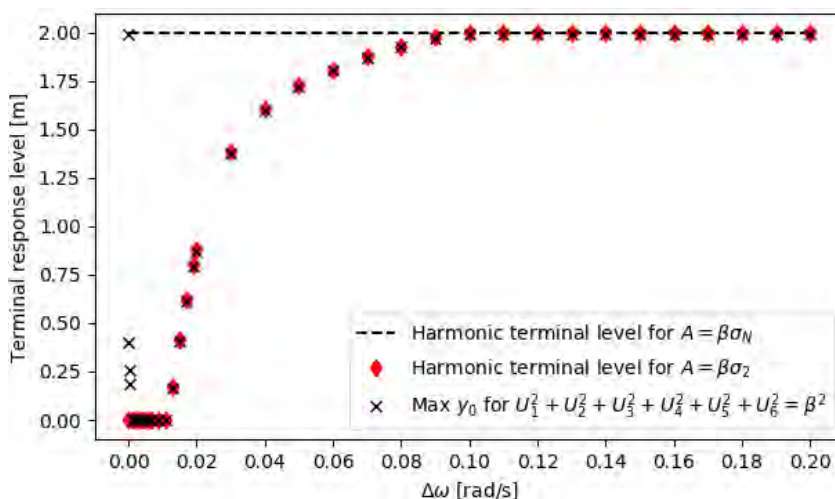
5 Global axial force response

5.1 Introduction and overview

The global axial force responses are input for the parametric excitation evaluation presented in Section 6, where the spectral densities of the axial force response are analysed in the SDOF evaluations.

The global analysis models established in OrcaFlex and Novaframe are used to analyse the global axial force response. The dynamic axial force response has been calculated for the individual load groups wind sea, swell and wind. Even though the client has informed the group that there is a correlation between the wind, wind sea and swell, it is believed to be more robust to evaluate the load groups individually, which enables us to do more screening of the individual sea states in the frequency domain.

Through the screening of the sea states, it is identified that for the K11 concept, a swell sea state around 13 seconds results in a high dynamic axial force, where the response is characterized by an eigenmode with high modal force and very low damping. The axial force response in the same frequency range is significantly reduced for the K12 and K14 concept because of the damping contributions from the mooring lines.

K13, especially when the bridge girder is monolithically connected to the abutment, is not prone to a build-up of net dynamic axial forces in the bridge girder in contrast to the other concepts. Thus, it does not give significant global variation of the geometric stiffness. Also, we see that the axial force response from swell, wind sea and wind is substantially lower than the other concepts, as presented in Section 5.4. K13 will fulfil the onset criterion and is therefore not evaluated in the succeeding sections.

5.1.1 Model description

A thorough description of the OrcaFlex and Novaframe model is given in Appendix F. The eigenmodes, damping, and the RAOs of the OrcaFlex model are also given in Appendix F and characterize the main characteristics for the dynamic response.

The structural damping of the bridge girder is assumed at 0.5% of the critical damping, according to [9]. In the OrcaFlex model, this is implemented as a stiffness- and mass-proportional Rayleigh damping, where the critical damping is 0.5% at 2 seconds and 0.5% at the longest eigenperiod of the concept (for K11 around 120s, for K12 and K14 around 40 seconds). The Rayleigh damping curve is depicted in Figure 5-1. Consequently, the OrcaFlex model underestimates the structural damping for most of the response.
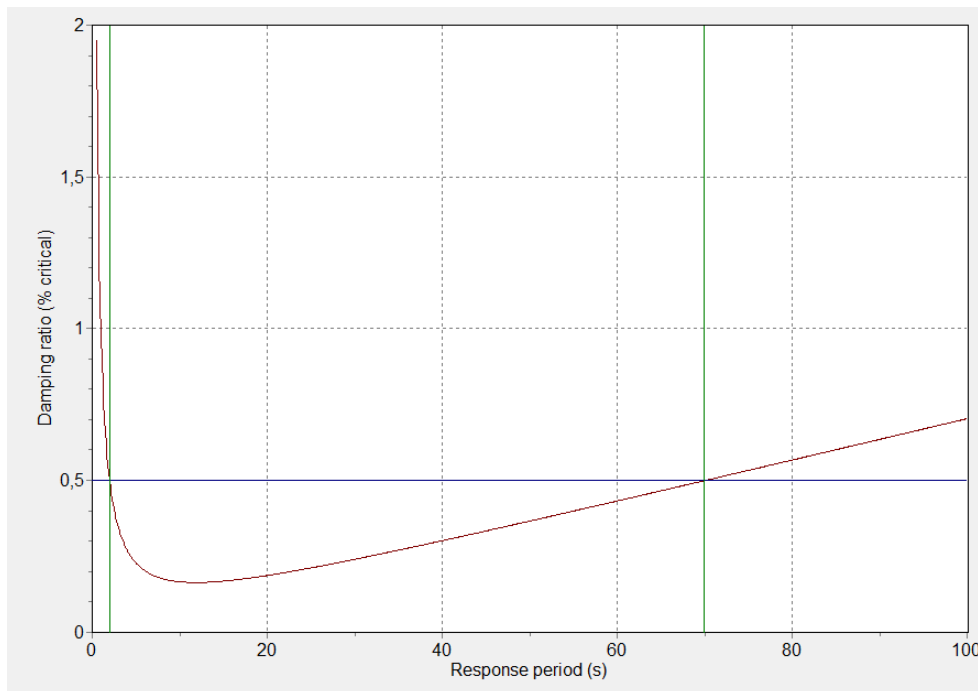
Figure 5-1: Plot of the applied structural damping in the numerical model.

5.1.2   Wind sea and swell response

A thorough sea state screening for K11, K12 and K14 has been performed to determine which sea states that yields the highest dynamic axial force response. In Appendix G, a sensitivity of the wave spectrum peakedness is presented, with respect to both the directional and frequency spreading. Generally, we find that the maximum peakedness yields the highest response, with the exception of the directional spreading of the swell sea. For the swell sea states, only given in the NW sector, there is a higher response when the wave direction is in the perpendicular direction to the bridge and therefore the lowest directional peakedness shape is selected.

In Appendix G, a sensitivity of the discretization of the frequency and directional spectrum is presented. Depending on the level of damping, the response may be vulnerable to the selection of frequency and direction components. For a low level of damping and few wave components the response may be significantly overestimated or underestimated, either by a too large weight of one / a few frequency component in resonance, or by not evaluating an important frequency range within the wave spectrum. Consequently, more frequency and directional components have been used to evaluate K11 (1500 components in each direction) as compared to K12 and K14 (300 components in each direction).

A directional screening of the 100-year and 10 000-year wind sea state conditions with the highest significant wave height and corresponding wave height as given in the Metocean design basis [3] has been assessed by a sea state screening. Also, lower peak periods have been evaluated, where the conclusion is that the highest peak period results in the highest maximum response in the wind sea frequency range, see Figure 5-3. The actual contour for the different return periods has not been evaluated, and at the next stage these should be evaluated, as the global response may be vulnerable to a further increase in peak period with an associated lower significant wave height. The contours provided in the design basis [3] are given in Figure 5-2.

The contours of swell, as defined in [3], have been evaluated by sea state screening. Only the 10 000-year return period has been considered, except for K12 where the screening results for both return periods are presented. The comparison of the response for K12 for the two return periods indicate

that a linear scaling between the 100-year and 10 000-year values is valid for screening of the swell sea states, see Figure 5-9 and Figure 5-10.
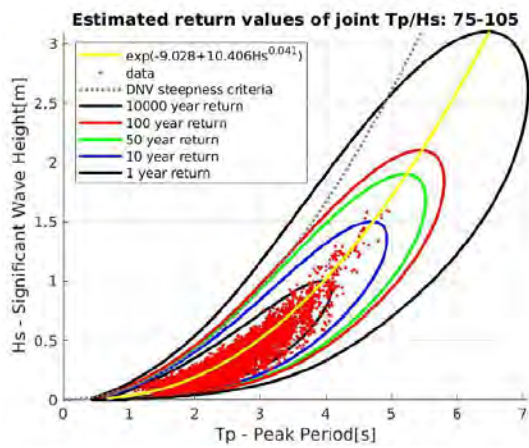
Figure 5-2. Example of the wind sea contours for different return periods for the east sector (75° − 105°) [3]. Only the peak value is used.
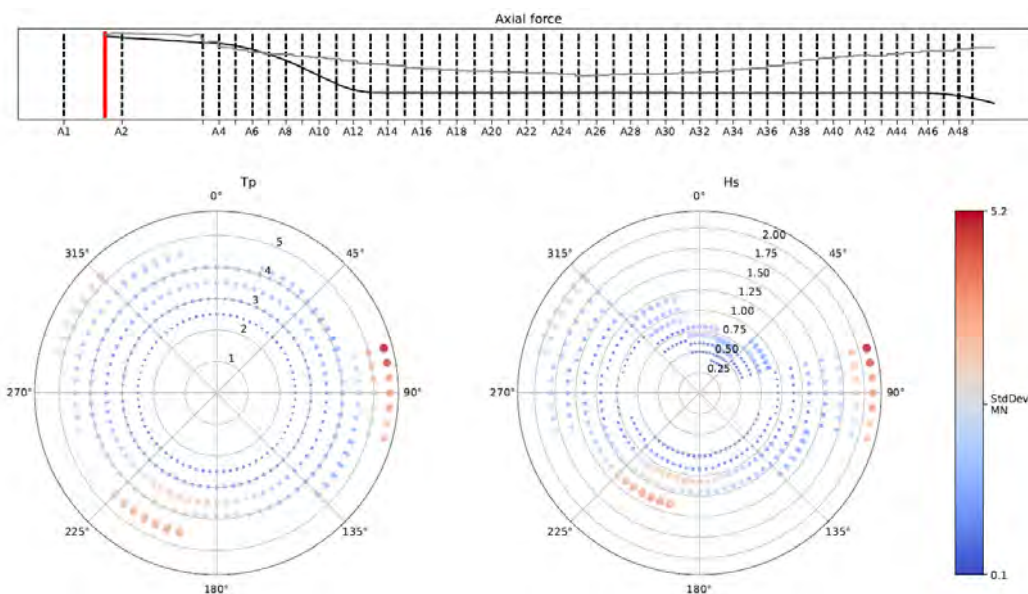
Figure 5-3. Sensitivity of axial force response for lower peak periods in wind sea, K11.

5.1.3   Wind response

The dynamic wind response has been analysed in Novaframe, where the modal axial force contribution is calculated from the defined wind spectrum. The results from the linear Novaframe model have been benchmarked with the results from the non-linear OrcaFlex model to validate the modal analysis results. The dynamic wind axial force is only considered to be important to evaluate in the frequency domain below the swell range. The dynamic axial force response from wind in the swell and wind sea frequency domain is low, compared to the swell and wind sea response. Thus, the waves will dominate the axial force for all concepts in this frequency range. However, the associated aerodynamic damping that is expected to occur in combination with wind sea is of importance to estimate in this frequency range, and has been evaluated for a set of directions, see Section 7.1.

5.1.4   Chapter outline

The following sub-sections does not provide figure references or other supporting text, for simplicity. The figures and the figure labels are assumed to sufficiently describe the process of establishing the worst-case conditions and the resulting spectral densities. The resulting power-spectral densities are shown when applied, in Section 6.

5.2   K11

5.2.1   Swell

Figure 5-4: Resulting global response from the swell sea state screening for K11, 10000-year return period. The sector plots illustrate the H_s, T_p and the global response (given by the colour scale and size of circles). The evaluated point along the bridge is given by the vertical red line. The envelope values along the bridge is given by the grey solid line along the arclength of the bridge given by the solid black curve. The largest response Is obtained for $H_s = 0.46m$, $T_p = 12.75s$, and $\theta_0 = 300°$.

5.2.2   Wind sea

Figure 5-5: Resulting global response from the 100-year wind sea state screening for K11. The sector plots illustrate the H_S, T_p and the global response (given by the colour scale and size of circles). The evaluated point along the bridge is given by the vertical red line. The envelope values along the bridge is given by the grey solid line along the arclength of the bridge given by the solid black curve. The largest response is obtained for $\theta_0 = 75°$.

Figure 5-6: Resulting global response from the 10 000-year wind sea state screening for K11. The sector plots illustrate the H_S, T_p and the global response (given by the colour scale and size of circles). The evaluated point along the bridge is given by the vertical red line. The envelope values along the bridge is given by the grey solid line along the arclength of the bridge given by the solid black curve. The largest response is obtained for $\theta_0 = 75°$.

5.2.3   Wind

Table 5-1: Modal aerodynamic damping as a fraction of critical damping and the modal standard deviation for the 100-year wind conditions for the K11 concept.

	Aerodynamic critical damping ratio, ξ_{aero}		Standard deviation of axial force, σ_N [MN]	
	From west	From east	From west	From east
Mode 1	0.0392	0.0387	-	-
Mode 2	0.0230	0.0214	1.42	1.27
Mode 3	0.0140	0.0125	-	-
Mode 4	0.0093	0.0082	0.93	-
Mode 5	0.0066	0.0058	-	-
Mode 6	0.0037	0.0033	2.29	1.90
Mode 7	0.0044	0.0038	-	
Mode 8	0.0033	0.0029	-	-
Mode 9	0.0030	0.0025	0.94	0.91
Mode 10	0.0025	0.0022	-	-
Mode 11	0.0034	0.0010	-	0.78
Mode 12	0.0011	0.0009	-	-
Total			3.35	2.99

Table 5-2. Modal aerodynamic damping as a fraction of critical damping and the modal standard deviation for the 10000-year wind conditions for the K11 concept.

	Aerodynamic critical damping ratio, ξ_{aero}		Standard deviation of axial force, σ_N [MN]	
	From west	From east	From west	From east
Mode 1	0.0460	0.0487	-	-
Mode 2	0.0272	0.0265	2.40	1.88
Mode 3	0.0167	0.0154	-	-
Mode 4	0.0111	0.0101	1.69	1.23
Mode 5	0.0079	0.0071	-	-
Mode 6	0.0045	0.0039	4.22	2.99
Mode 7	0.0054	0.0046	-	-
Mode 8	0.0038	0.0036	1.70	-
Mode 9	0.0037	0.0031	1.66	1.33
Mode 10	0.0031	0.0027	-	-
Mode 11	0.0024	0.0047	-	-
Mode 12	0.0012	0.0016	-	-
Total			6.26	4.37
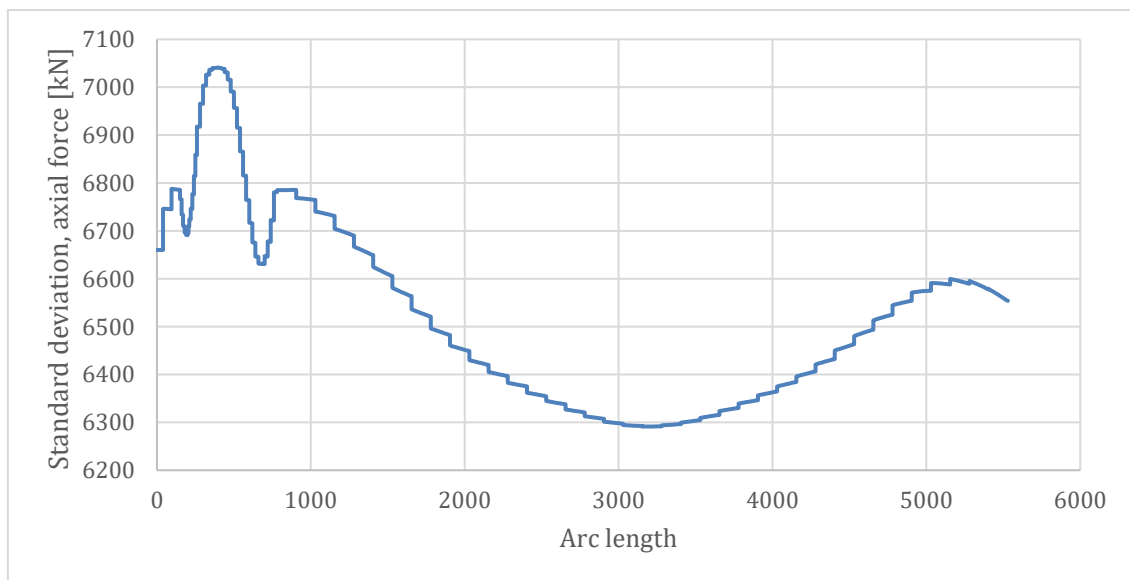
Figure 5-7: Standard deviation of axial force response, worst of 10 realizations for a 10000-year (west) wind condition, K11, from OrcaFlex.
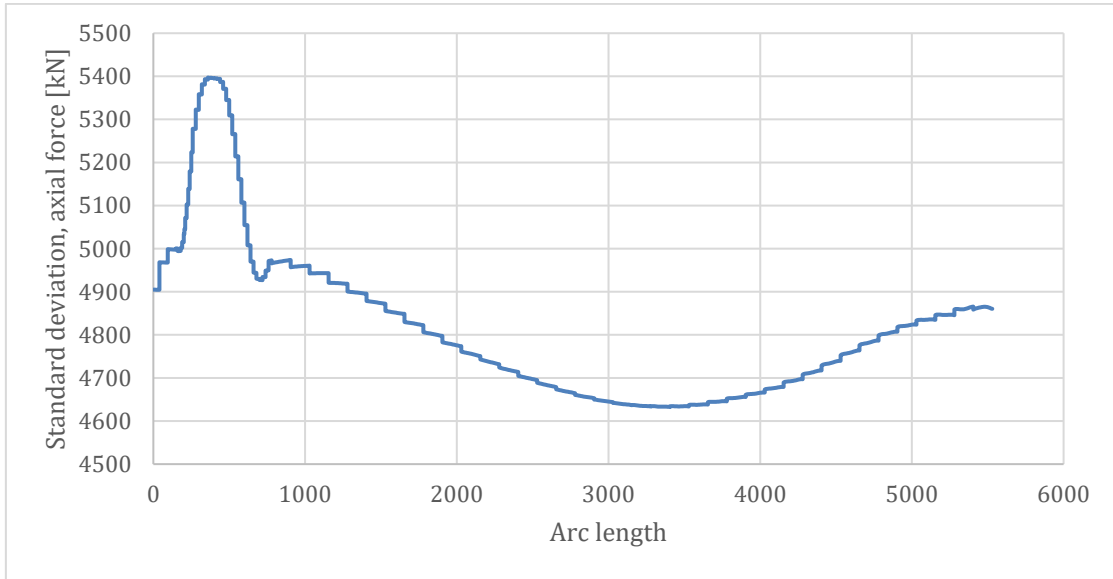
Figure 5-8: Standard deviation of axial force response, worst of 10 realizations for a 10000-year (east) wind condition, K11, from OrcaFlex.
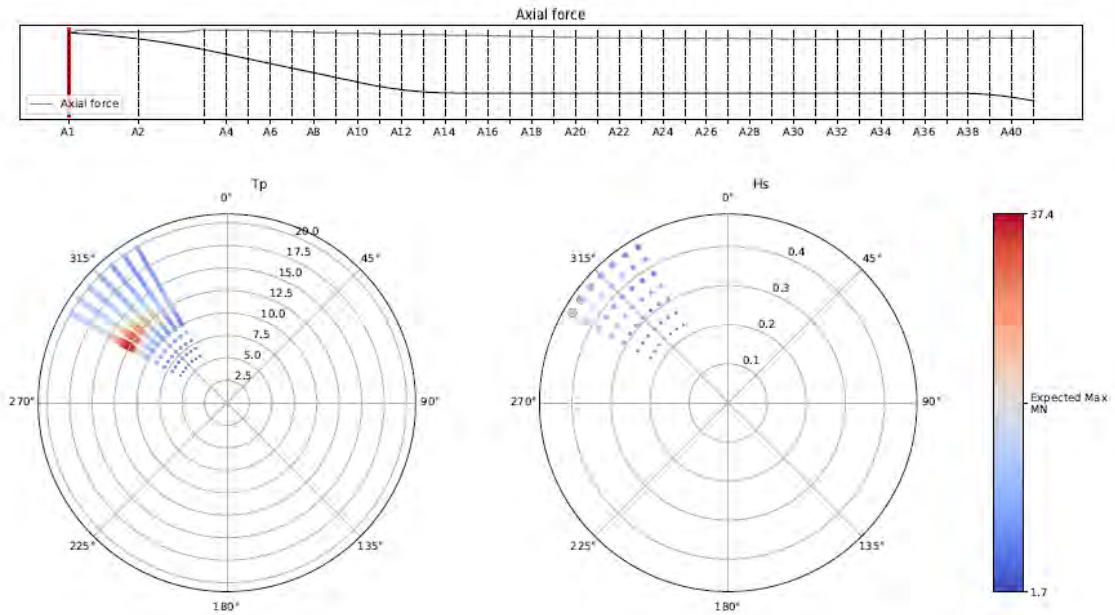
5.3   K12

5.3.1   Swell
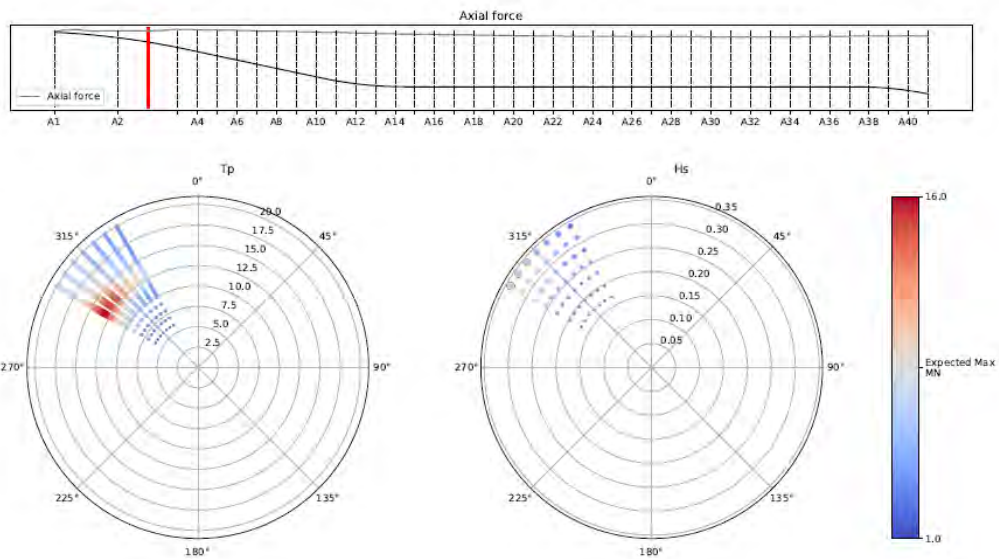
Figure 5-9: Resulting global response from the swell sea state screening for K12, 100-year return period. The sector plots illustrate the H_s, T_p and the global response (given by the colour scale and size of circles). The evaluated point along the bridge is given by the vertical red line. The envelope values along the bridge is given by the grey solid line along the arclength of the bridge given by the solid black curve. The largest response is obtained for $H_s = 0.34m$, $T_p = 13.5s$, $\theta_0 = 300°$.
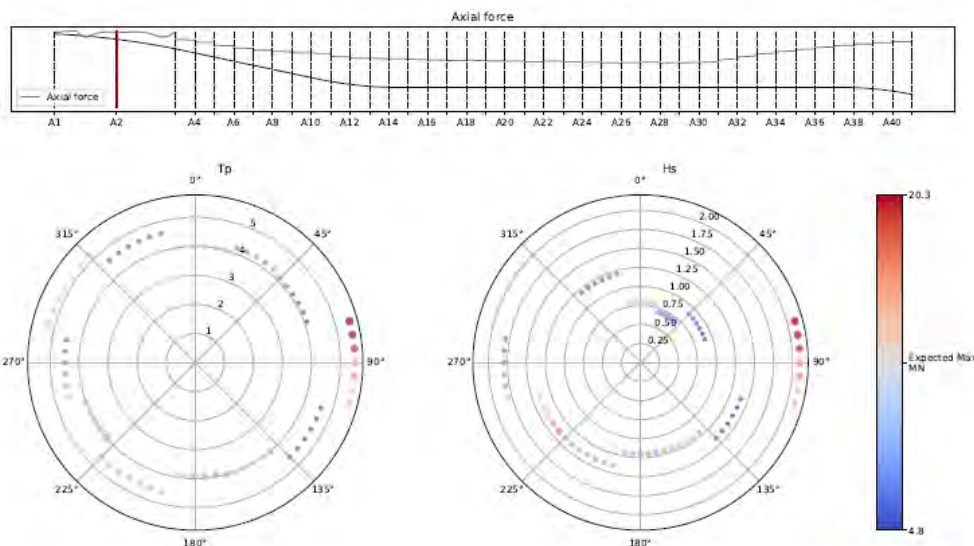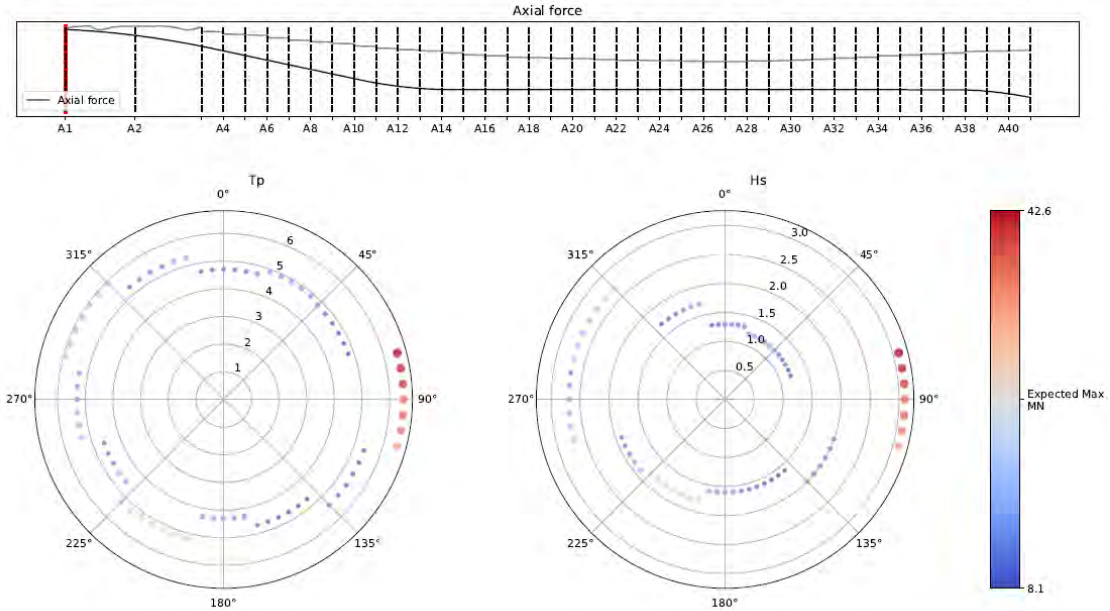
Figure 5-10: Resulting global response from the swell sea state screening for K12, 10 000-year return period. The sector plots illustrate the H_s, T_p and the global response (given by the colour scale and size of circles). The evaluated point along the bridge is given by the vertical red line. The envelope values along the bridge is given by the grey solid line along the arclength of the bridge given by the solid black curve. The largest response is obtained for $H_s = 0.46m$, $T_p = 13.5s$, $\theta_0 = 300°$.

5.3.2   Wind sea

Figure 5-11. Resulting global response from the 10 000-year wind sea state screening for K12. The sector plots illustrate the H_s, T_p and the global response (given by the colour scale and size of circles). The evaluated point along the bridge is given by the vertical red line. The envelope values along the bridge is given by the grey solid line along the arclength of the bridge given by the solid black curve. The largest response is obtained for $\theta_0 = 75°$.
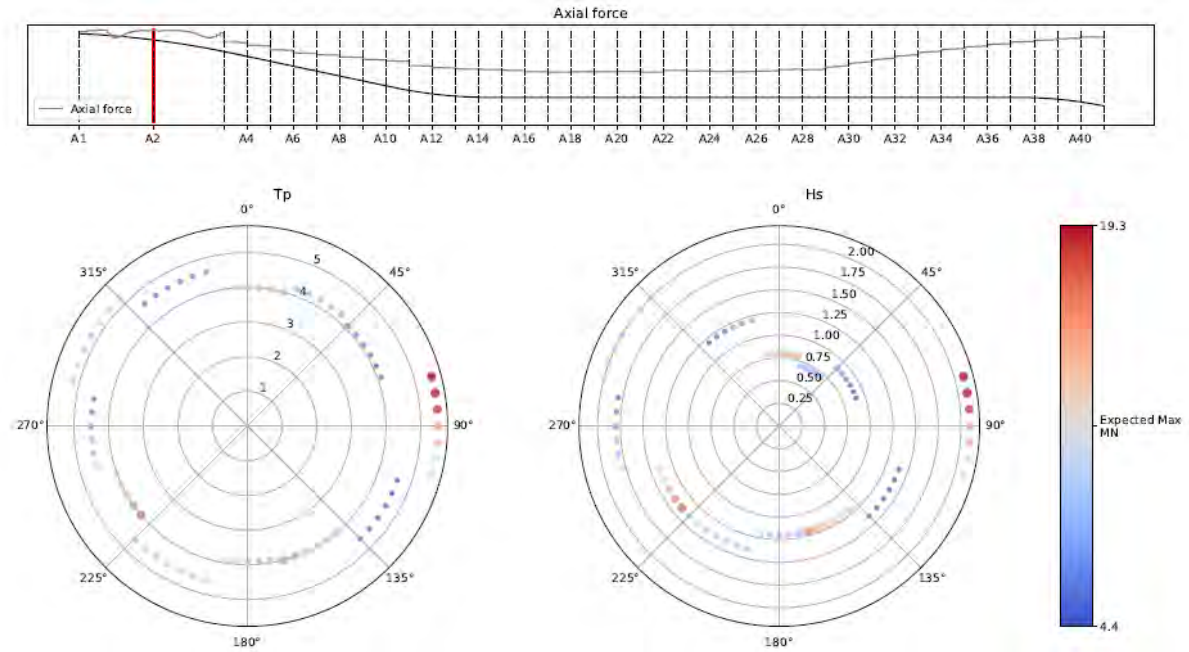
Figure 5-12: Resulting global response from the 100-year wind sea state screening for K12. The sector plots illustrate the H_s, T_p and the global response (given by the colour scale and size of circles). The evaluated point along the bridge is given by the vertical red line. The envelope values along the bridge is given by the grey solid line along the arclength of the bridge given by the solid black curve. The largest response is obtained for $H_s = 3.1m$, $T_p = 6.5s$, and $\theta_0 = 75°$.

5.3.3 Wind

Table 5-3: Modal aerodynamic damping as a fraction of critical damping and the modal standard deviation for the 100-year wind conditions for the K12 concept.

	Aerodynamic critical damping ratio, ξ_{aero}		Standard deviation of axial force, σ_N [MN]	
	From west	From east	From west	From east
Mode 1	0.0126	0.0107	-	-
Mode 2	0.0117	0.0100	-	-
Mode 3	0.0096	0.0082	-	-
Mode 4	0.0087	0.0074	0.59	0.41
Mode 5	0.0052	0.0044	-	-
Mode 6	0.0037	0.0031	1.25	0.86
Mode 7	0.0031	0.0027	1.29	0.88
Mode 8	0.0028	0.0024	-	-
Mode 9	0.0026	0.0022	0.89	0.61
Mode 10	0.0023	0.0020	-	-
Mode 11	0.0027	0.0023	-	-
Mode 12	0.0012	0.0010	0.84	0.59
Total			2.53	1.75

Table 5-4: Modal aerodynamic damping as a fraction of critical damping and the modal standard deviation for the 10 000-year wind conditions for the K12 concept.

	Aerodynamic critical damping ratio, ξ_{aero}		Standard deviation of axial force, σ_N [MN]	
	From west	From east	From west	From east
Mode 1	0.0260	0.0237	-	-
Mode 2	0.0215	0.0199	-	-
Mode 3	0.0151	0.0138	-	-
Mode 4	0.0101	0.0091	0.86	0.58
Mode 5	0.0086	0.0078	-	-
Mode 6	0.0066	0.0060	2.47	1.39
Mode 7	0.0052	0.0043		0.96
Mode 8	0.0044	0.0039	-	-
Mode 9	0.0036	0.0031	1.72	1.20
Mode 10	0.0033	0.0029	-	-
Mode 11	0.0016	0.0014	-	-
Mode 12	0.0018	0.0017	0.78	0.57
Total			4.00	2.71
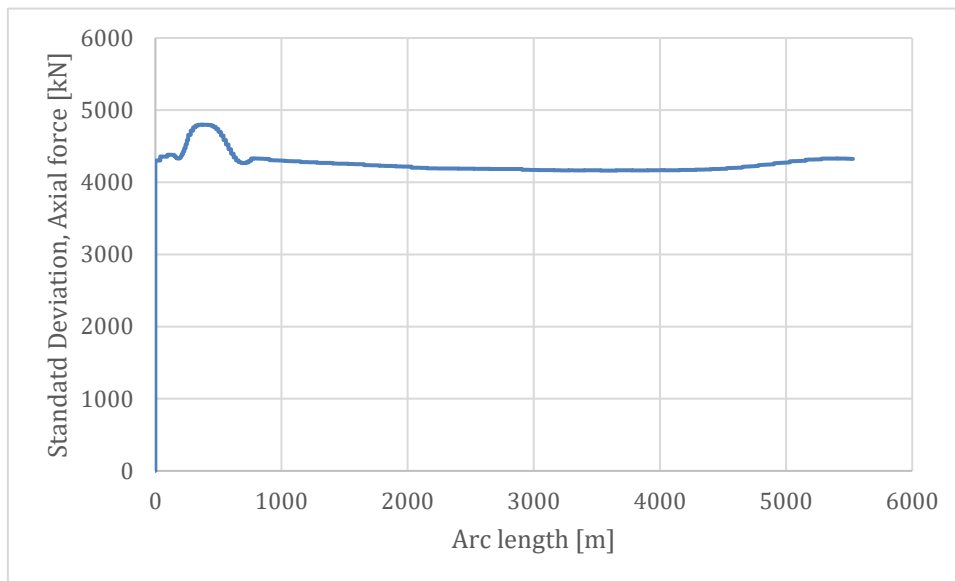
Figure 5-13: Standard deviation of axial force response, worst of 10 realizations for a 10000-year (west) wind condition, K12, from OrcaFlex.
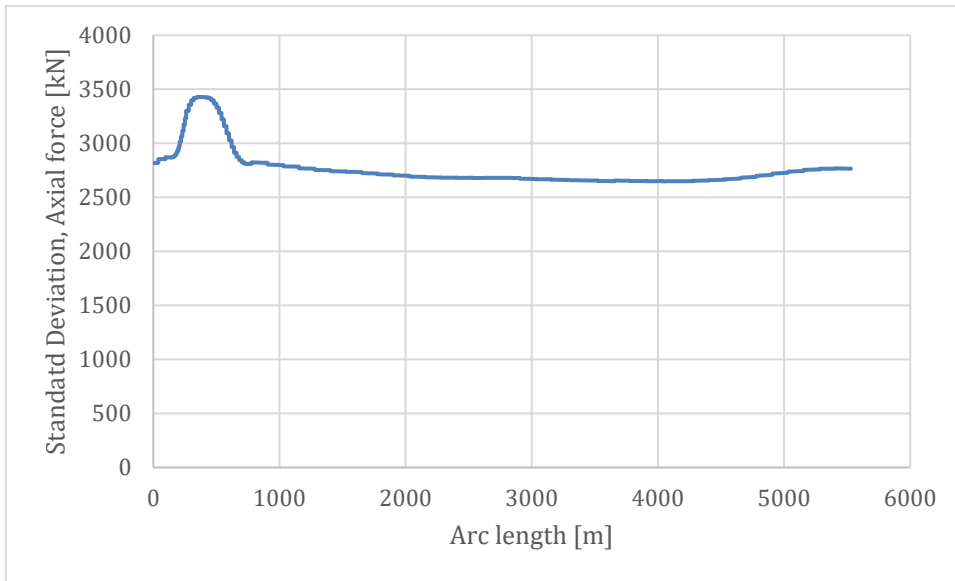
Figure 5-14: Standard deviation of axial force response, worst of 10 realizations for a 10000-year (east) wind condition, K12, from OrcaFlex.
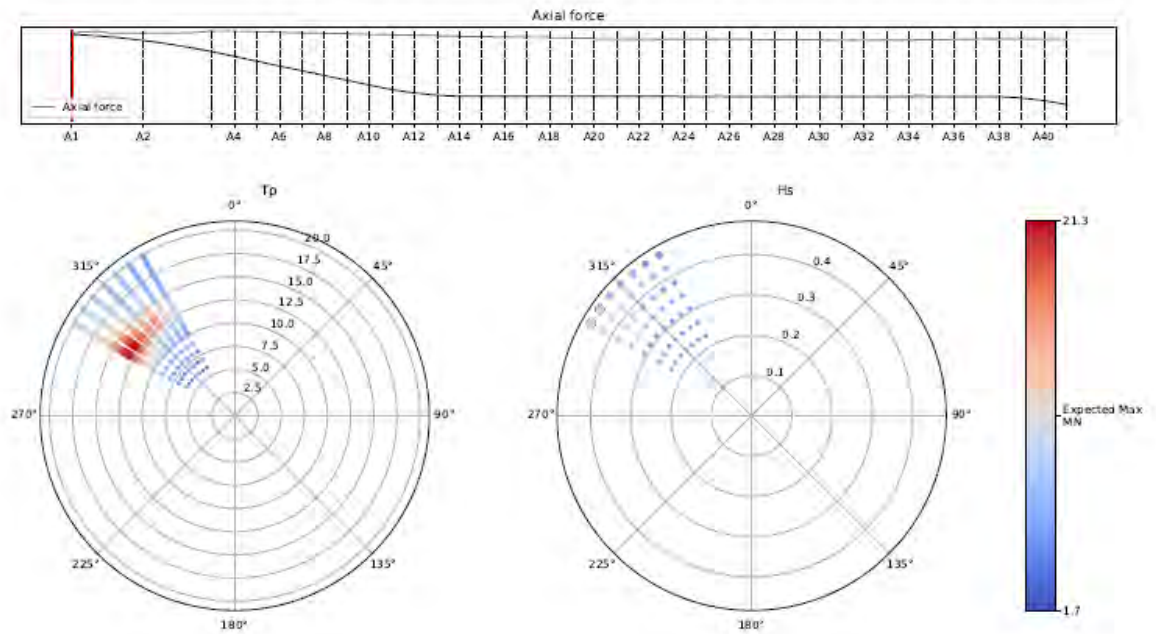
5.4   K13
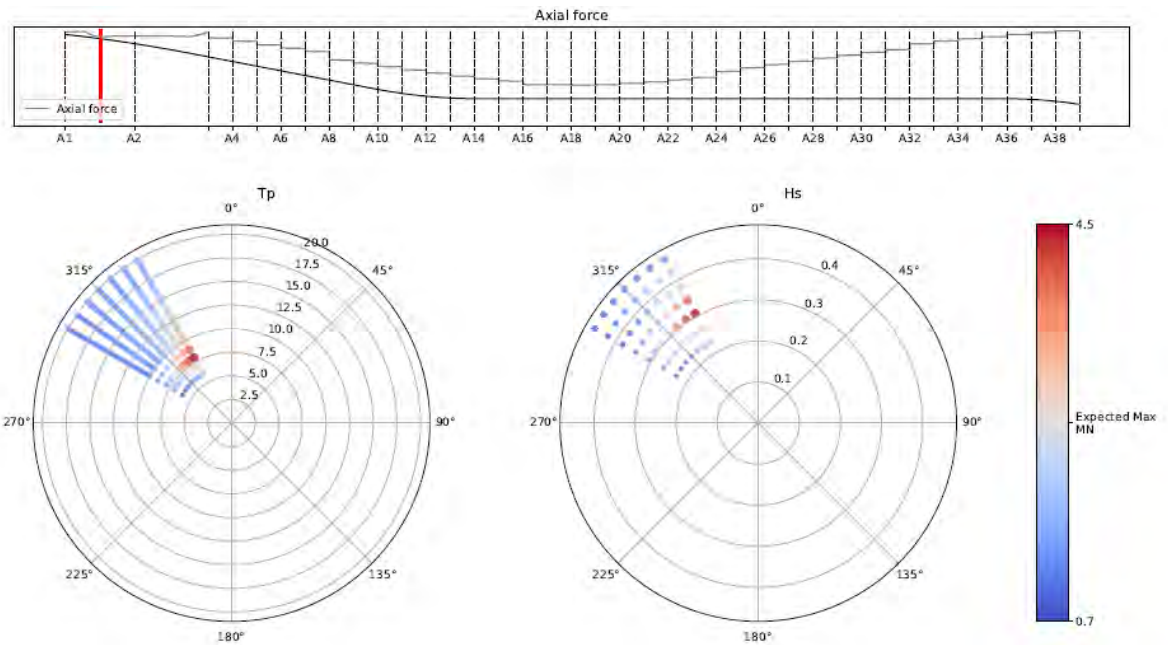
Figure 5-15: Resulting global response from the swell sea state screening for K13, 10 000-year return period. The sector plots illustrate the H_s, T_p and the global response (given by the colour scale and size of circles). The evaluated point along the bridge is given by the vertical red line. The envelope values along the bridge is given by the grey solid line along the arclength of the bridge given by the solid black curve. The largest response is obtained for $H_s = 0.31m$, $T_p = 8s$, $\theta_0 = 330°$.
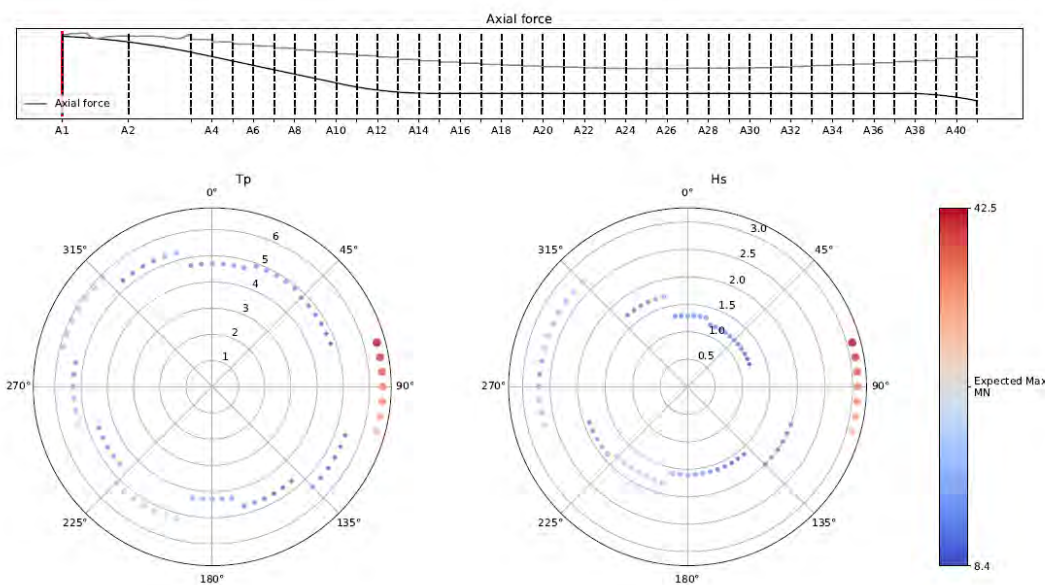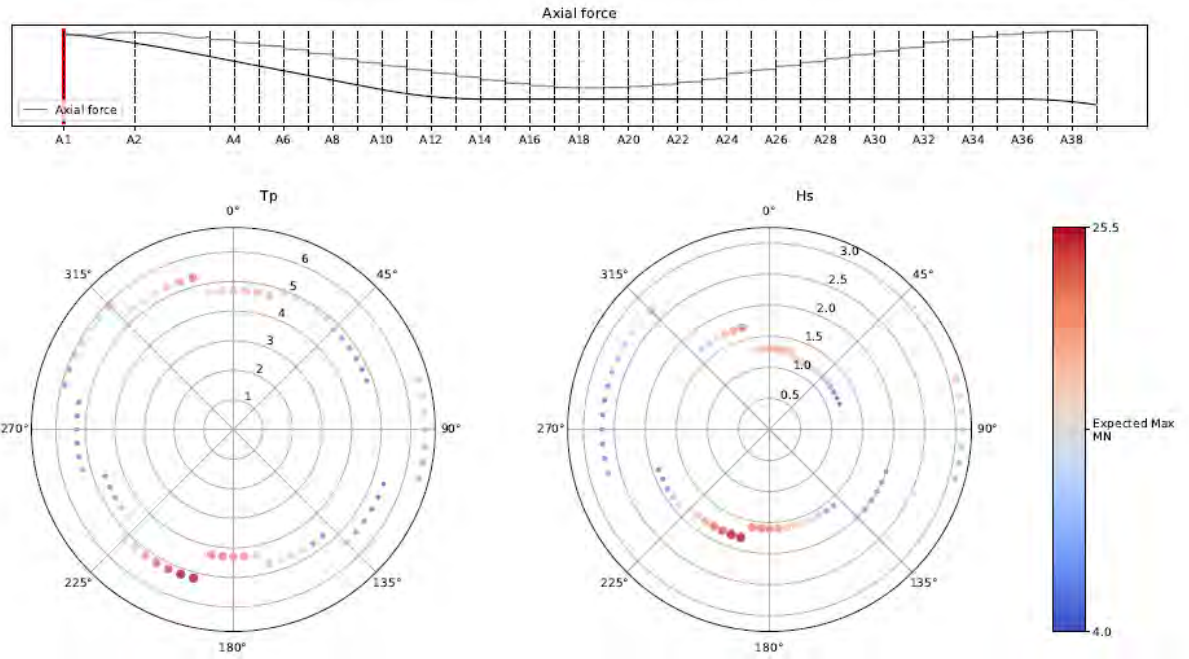
Figure 5-16. Resulting global response from the 10 000-year wind sea state screening for K13. The sector plots illustrate the H_s, T_p and the global response (given by the colour scale and size of circles). The evaluated point along the bridge is given by the vertical red line. The envelope values along the bridge is given by the grey solid line along the arclength of the bridge given by the solid black curve. The largest response is obtained for $\theta_0 = 195°$.
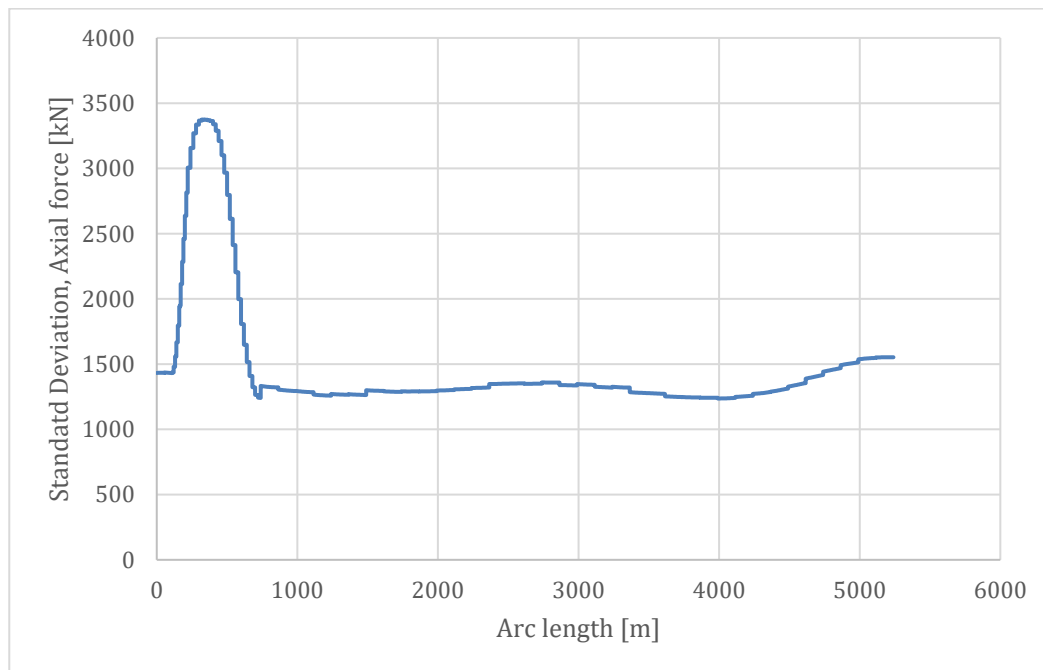

Figure 5-17: Standard deviation of axial force response, worst of 10 realizations for a 10000-year (east) wind condition, K13, from OrcaFlex.

5.5   K14

5.5.1   Swell
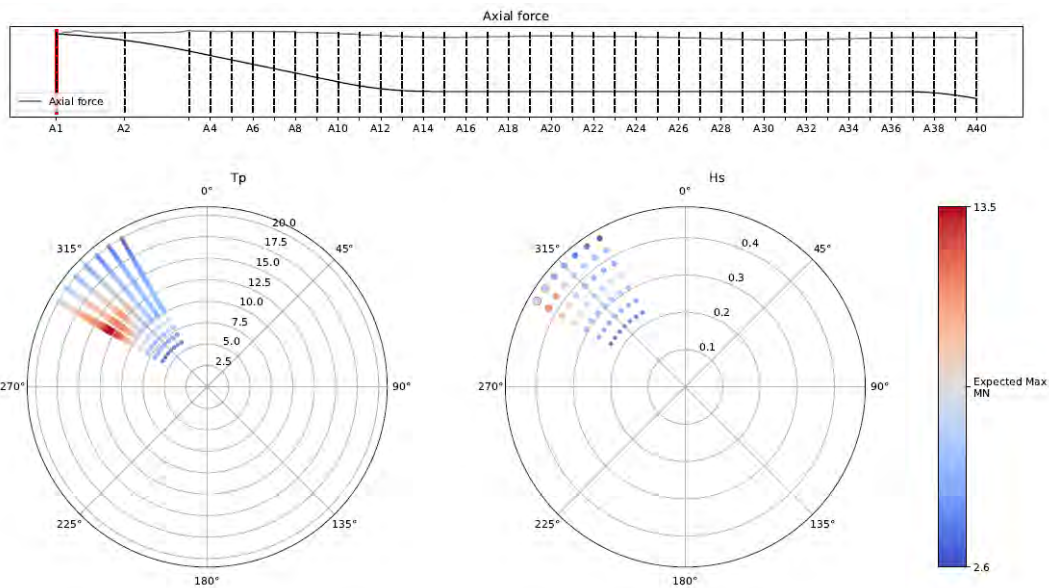
Figure 5-18: Resulting global response from the swell sea state screening for K12. The sector plots illustrate the H_s, T_p and the global response (given by the colour scale and size of circles). The evaluated point along the bridge is given by the vertical red line. The envelope values along the bridge is given by the grey solid line along the arclength of the bridge given by the solid black curve. The largest response is obtained for. $H_s = 0.46m$, $T_p = 13.25s$, $\theta_0 = 300°$.

5.5.2   Wind sea
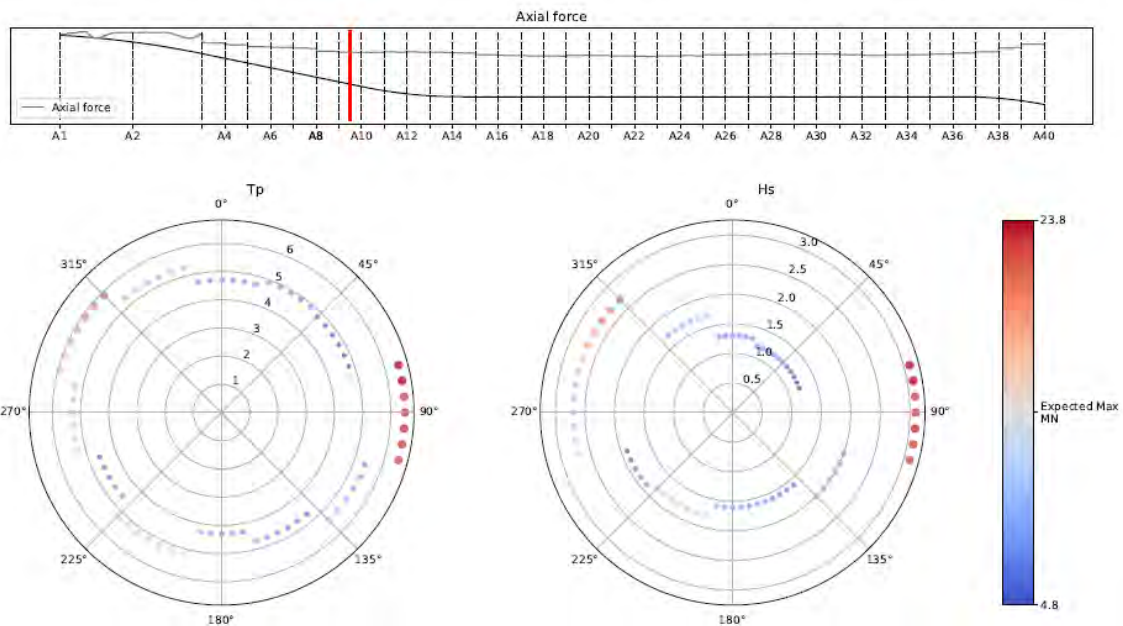
Figure 5-19: Resulting global response from 10 000-year wind sea state screening for K14. The sector plots illustrate the H_s, T_p and the global response (given by the colour scale and size of circles). The evaluated point along the bridge is given by the vertical red line. The envelope values along the bridge is given by the grey solid line along the arclength of the bridge given by the solid black curve. The maximum response is obtained for $H_s = 3.1m$, $T_p = 6.5s$, $\theta_0 = 75°$.
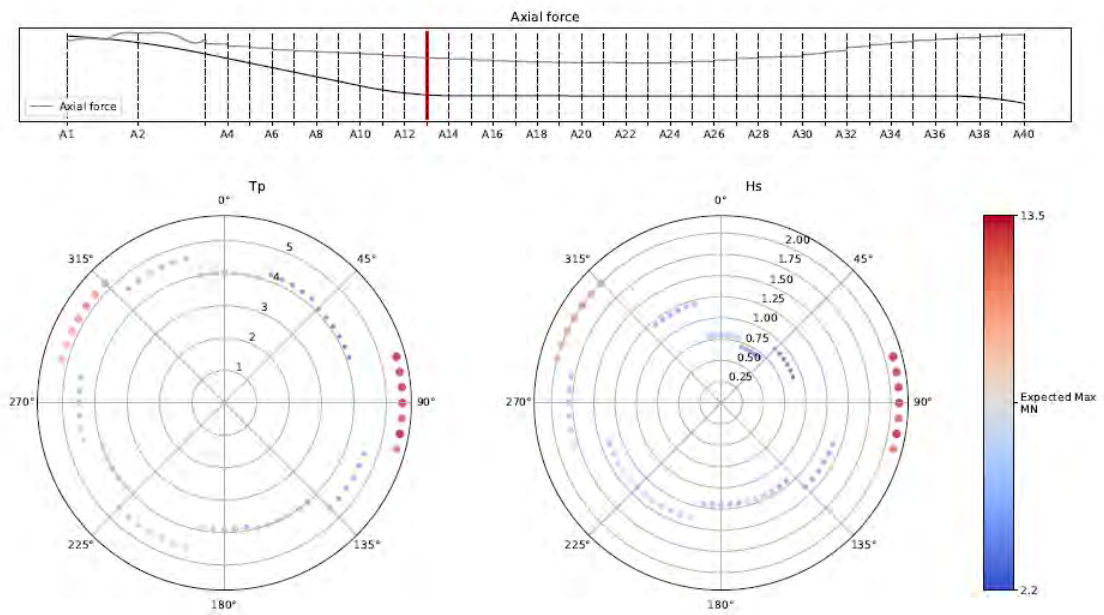
Figure 5-20: Resulting global response from 100 year wind sea state screening for K14. The sector plots illustrate the H_s, T_p and the global response (given by the colour scale and size of circles). The evaluated point along the bridge is given by the vertical red line. The envelope values along the bridge is given by the grey solid line along the arclength of the bridge given by the solid black curve. The maximum response is obtained for $\theta_0 = 75°$.

5.5.3   Wind

Table 5-5: Modal aerodynamic damping as a fraction of critical damping and the modal std deviation for the 100-year wind conditions for the K14 concept

	Aerodynamic critical damping ratio, ξ_{aero}		Standard deviation of axial force, σ_N [MN]	
	From west	From east	From west	From east
Mode 1	0.0142	0.0125	-	-
Mode 2	0.0140	0.0118	-	-
Mode 3	0.0117	0.0098	-	-
Mode 4	0.0091	0.0077	-	-
Mode 5	0.0062	0.0052	0.49	0.42
Mode 6	0.0045	0.0038	0.67	0.58
Mode 7	0.0028	0.0029	-	0.57
Mode 8	0.0033	0.0028	-	-
Mode 9	0.0028	0.0032	0.66	
Mode 10	0.0025	0.0021	-	-
Mode 11	0.0017	0.0008	-	-
Mode 12	0.0015	0.0022		
Total			1.54	1.21

Table 5-6: Modal aerodynamic damping as a fraction of critical damping and the modal std deviation for the 10000-year wind conditions for the K14 concept

| | Aerodynamic critical damping ratio, ξ_{aero} | | Standard deviation of axial force, σ_N [MN] | |
	From west	From east	From west	From east
Mode 1	0.0179	0.0152	-	-
Mode 2	0.0171	0.0144	-	-
Mode 3	0.0142	0.0119	-	-
Mode 4	0.0111	0.0093	-	-
Mode 5	0.0075	0.0064	1.22	0.85
Mode 6	0.0054	0.0046	1.69	1.18
Mode 7	0.0035	0.0040		
Mode 8	0.0041	0.0034	-	-
Mode 9	0.0034	0.0029	1.63	1.11
Mode 10	0.0029	0.0025	-	-
Mode 11	0.0011	0.0010	-	-
Mode 12	0.0012	0.0099		
Total			3.48	2.42
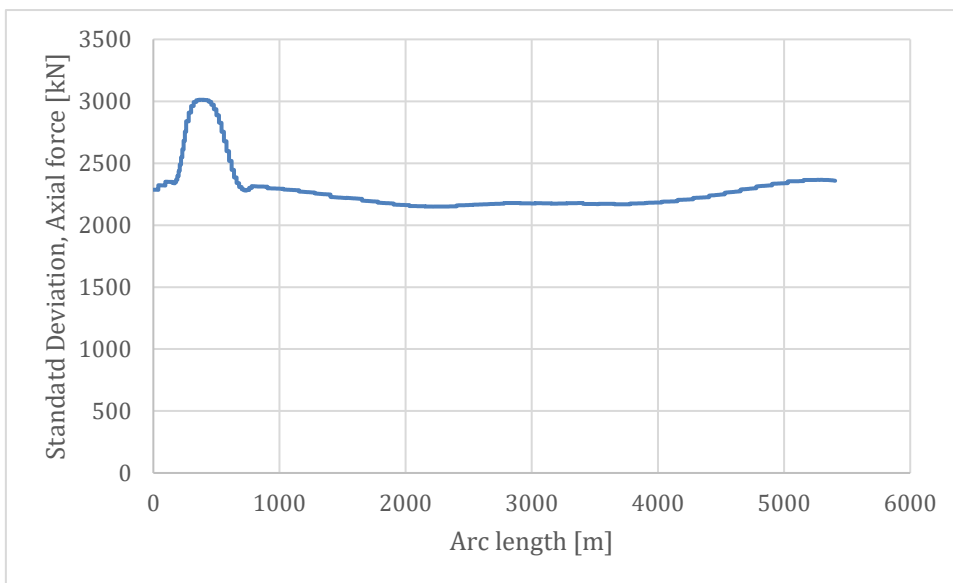
Figure 5-21: Standard deviation of axial force response, worst of 10 realizations for a 10000-year (east) wind condition, K14, from OrcaFlex.
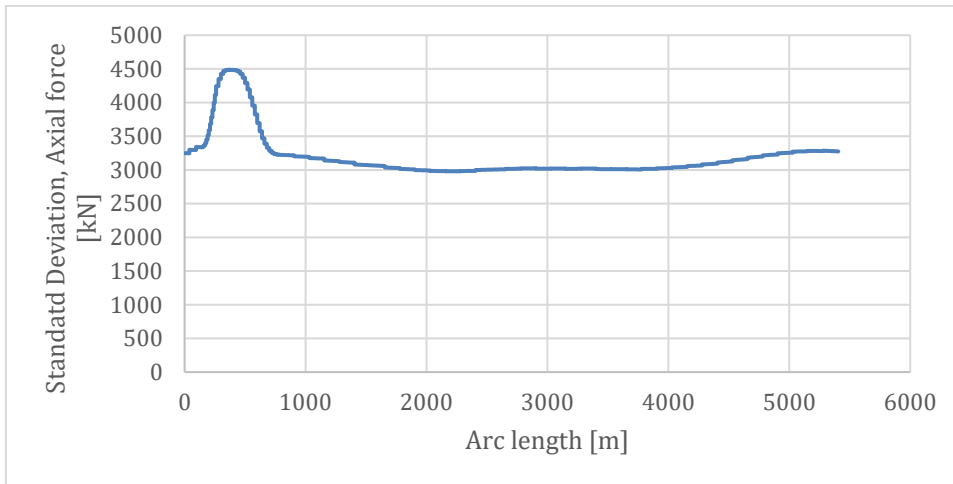
Figure 5-22: Standard deviation of axial force response, worst of 10 realizations for a 10000-year (west) wind condition, K14, from OrcaFlex.

5.6 Static axial forces

Table 5-7 shows the axial force response of K11, K12 and K14, from various static loads. The corresponding envelope values along the bridge are provided in Appendix G. By comparing the static loads with the amplitudes of the ratio $k/\hat{k}_g$ for the various modes, the effect of the static loads on the robustness against parametric resonance can be studied. When static compression axial forces are present in the structure, the linearized stiffness change is $k_g = -\hat{k}_g N$, such that the net stiffness of a mode is $k_{tot} = k - \hat{k}_g N$. This implies that the linearized modal buckling load is $N_{cr} = \frac{k}{\hat{k}_g}$, under the assumption that the mode shapes of buckling and vibration are identical.

A more in-depth investigation into the effect of static forces will be made on the prioritized concept in the next stage. By linearizing the dynamic model about the conditions provided by all static loads, a more accurate conclusion of the effect of static forces could be drawn.

The static forces may also greatly affect the pretension and therefore the mooring characteristics, including the nonlinear damping coefficient applied in the evaluation of parametric resonance. In Appendix G, Section 8.1, this topic is addressed, showing that a 20-25% reduction of the damping coefficient may occur for a temperature and tidal static load. This topic should be investigated further to ensure that all critical combinations of static forces and dynamic responses are evaluated.

The effect of static axial forces is studied more in detail for K12 in Enclosure 6.

Table 5-7. Static axial force response.

	K11 with $C_d = 0.4$	K11 with $C_d = 1$	K11 with $C_d = 2$	K12 with $C_d = 0.4$	K14 with $C_d = 0.4$
Current	6.5MN	15MN	29MN	6MN	<1MN
Wind from east	15MN	15MN	15MN	14MN	3MN
Mean drift	2MN	2MN	2MN	2MN	<1MN
Temperature, 100 year return period	-	-	-	14 MN	10MN
Total	23.5MN	32MN	46MN	36MN	14MN

6   Concept assessments: critical amplitudes and terminal level estimates

6.1   Simulation set-up and assumptions

6.1.1   Simulation parameters

A drag coefficient of $C_d = 0.3$ is used for all concepts, both to establish axial force spectral densities in the global analyses and to the estimate the quadratic pontoon drag damping contributions which is used in the SDOF predictions.

6.1.2   Spectral densities

The considered axial force spectral densities are the worst-case conditions identified in the screening analyses presented above, according to a pre-set annual occurrence probability, q_{cond}. Both 100-year conditions and 10000-year conditions are considered for both wind sea, swell and wind excitation. The full spectral densities were used for Monte Carlo simulations; the segmentation of the spectral densities is therefore only relevant for the computation of the terminal level estimates.

6.1.3   Terminal response estimates

The critical amplitudes corresponding to $\beta = 2.0$ are the only relevant, as the critical amplitudes for the other frequency ratios are not exceeded by the axial force response in any of the modes. The full result listing concerning parametric excitation generated from the analysis of all concepts are provided in Enclosure 2, for reference. The results obtained with frequency ratios $\beta = 1.0$ and $\beta = 0.5$ are also given there. In some cases, the estimated terminal response level is larger than zero even though the onset criterion is not exceeded, i.e., where $\sigma_N < 0.4 A_{cr}$. This is a consequence of the fact that the harmonic amplitude with a chosen exceedance probability might be larger than $\sigma_N / 0.4$. Note that the terminal level estimates of such cases are not given any significance in the interpretation of the results.

As pointed out in Section 4, the terminal level estimation from wind sea excitation is most likely over-conservative in the following assessment; due to the broadbandedness of it, much of the energy in the spectral density is not relevant for parametric resonance, as it is located too far from the critical frequency (ratio of 2, typically). A more refined treatment of the wind sea excitation could be preferable. However, to compare the concepts, the treatment following below is considered reasonable.

6.1.4   Adjustments for Monte Carlo simulation

The Monte Carlo simulations were all carried out by shifting the peak frequency of the dominating segment of the axial force variation such that it was precisely located at the frequency ratio determined as critical in the linear terminal level estimate procedure. The number of realizations vary for the different cases, and is therefore indicated throughout the chapter.

The realization durations were defined such that a total of 500 cycles of vibration of the considered modes were simulated, in hope of enabling the systems to reach parametric resonance. Thus, for the treatment of the results in a statistical manner, the scaling of the short-term probability, as given in Section 3.5.4, was applied. Due to different natural frequencies, different durations can be observed throughout the section. Note that the short-term conditions corresponding to durations of 1h where applied, even though the simulation durations were longer; in reality, the short-term conditions would be less harsh for longer durations, if the two alternatives are to refer to the same probability level.

6.2   Overview of the concepts

The most important modal properties involved in the analysis of the robustness against parametric excitation are compared between all concepts in Figure 6-1 (ratios between stiffness and force-normalized axial force) and Figure 6-2 (critical damping ratios), which result in the critical amplitudes provided in Figure 6-3. The results are given for maximum displacements of the girder from each mode equal to 3m and 0m (no quadratic drag damping contribution). The figures reveal that the side-anchored concepts provide significantly larger linearized critical damping ratios, and thus, critical amplitude compared to K11 (beyond onset). Furthermore, K12 has the best robustness for the critical mode 4, which is potentially parametrically excited by swell, whereas K14 and K13 show a significantly better robustness for mode 5.

In principle, the anchor lines' proneness to parametric excitation should also be investigated for the moored concepts. A crude assessment of the risk and consequence of parametric excitation of mooring lines is therefore given in Enclosure 5, indicating that this will not be a relevant problem. A more refined analysis should follow at a later stage of the project.
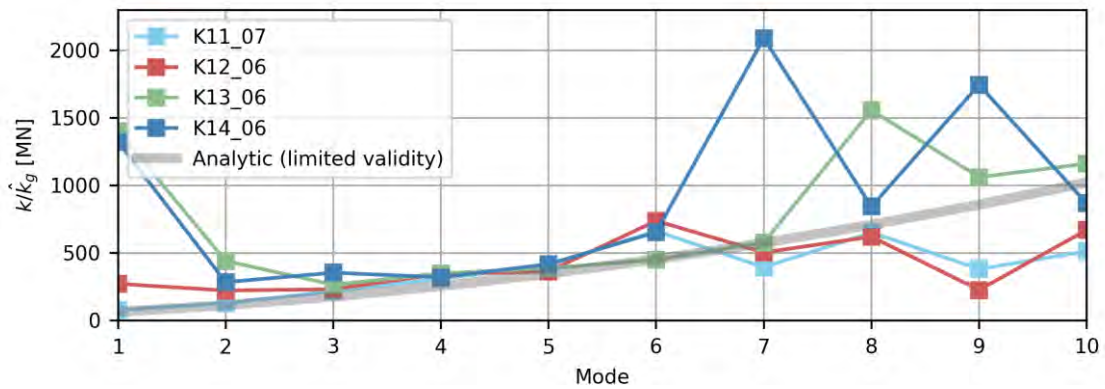
Figure 6-1. $k/\hat{k}_g$ for all concepts.
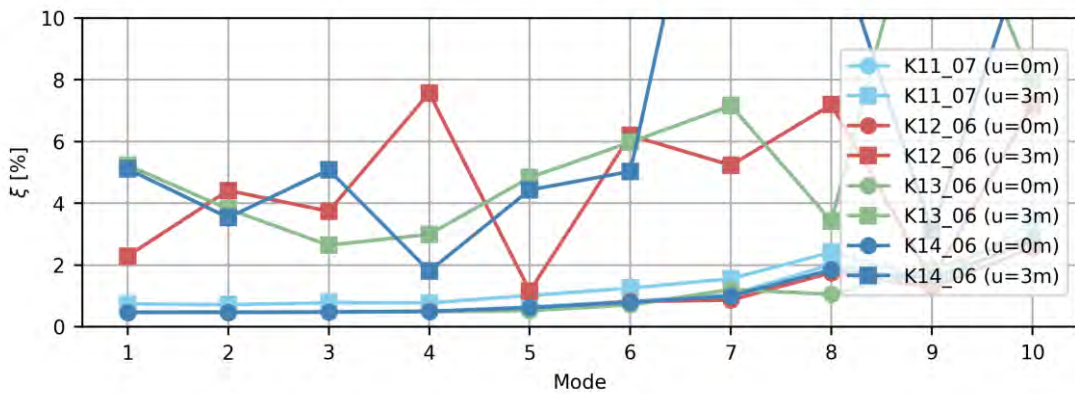
Figure 6-2.Critical damping ratio ξ for all concepts, corresponding to maximum girder displacements of 0m and 3m (linearized quadratic damping included).
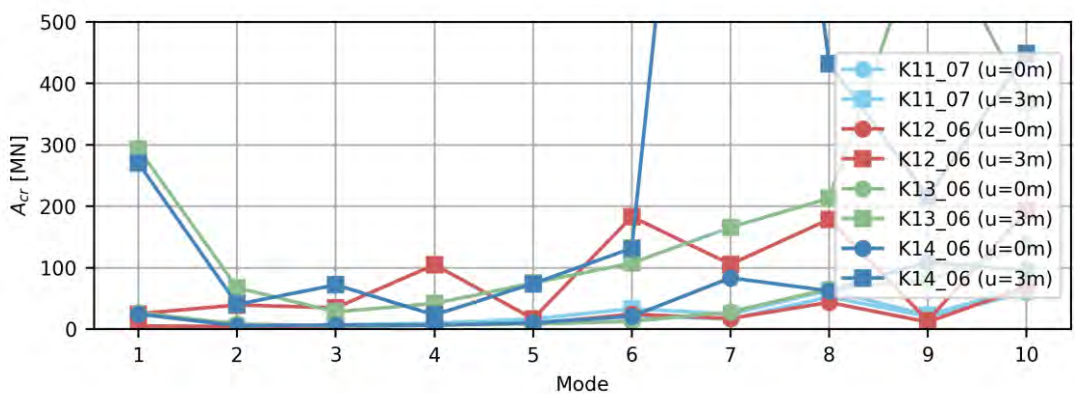
Figure 6-3. Critical axial force amplitude resulting from $k/\hat{k}_g$ in Figure 6-1 and ξ in Figure 6-2.

Concept development, floating bridge E39 Bjørnafjorden

Appendix S – Parametric excitation – K12 .... 6 Concept assessments: critical amplitudes and terminal level estimates

6.3 K11

The ten first modes of K11 are presented in Figure 6-4 and Table 6-1. The succeeding sub-sections study the robustness regarding parametric excitation from swell, wind sea and wind.
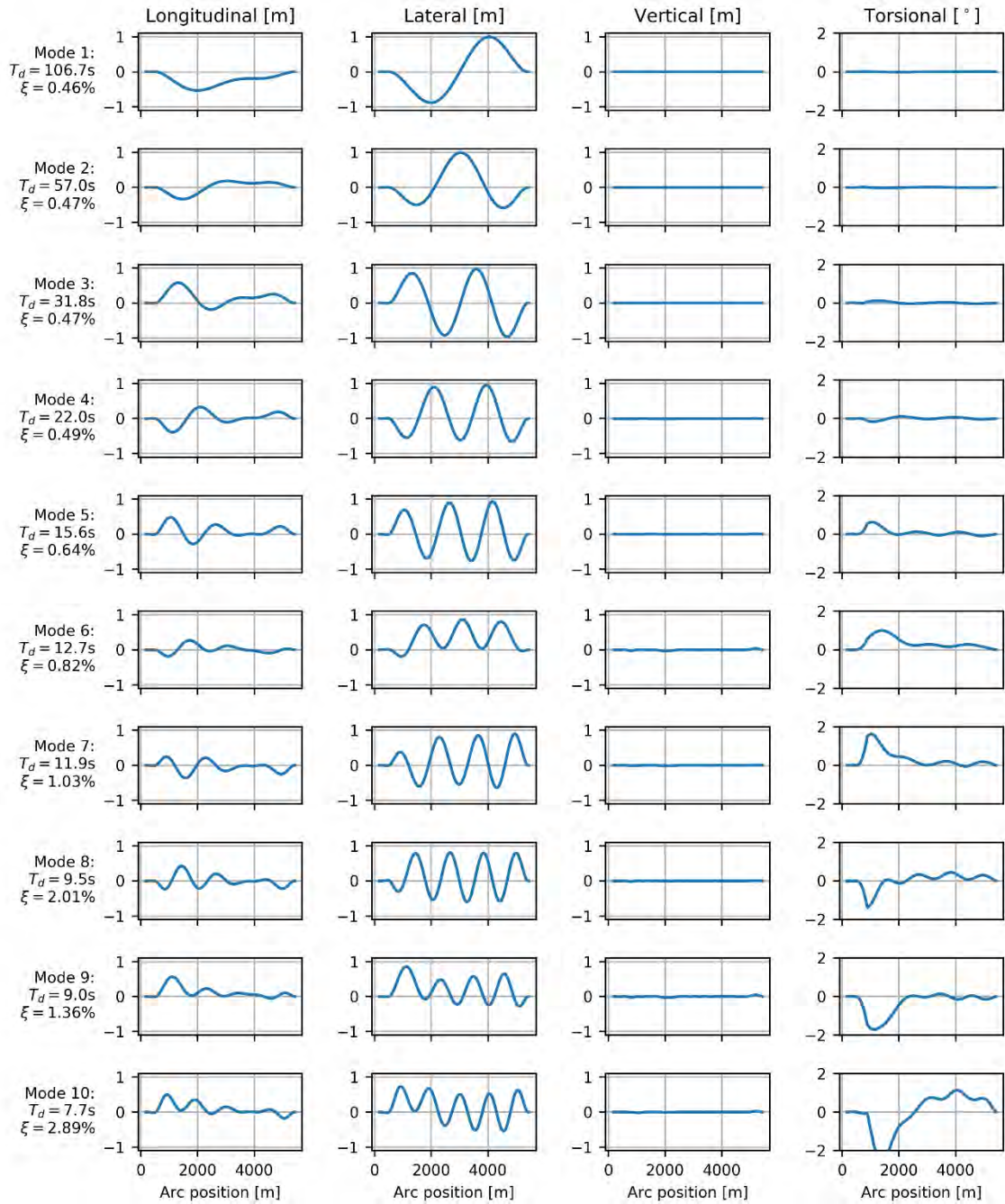
Figure 6-4. First 10 modes of K11_07.

Table 6-1. Modal parameters of K11_07. The aerodynamic damping is not included in the critical damping ratios listed, because they are dependent on the mean wind speed. It is also assumed that a swell condition can occur without the presence of wind.

Mode	ω_d [rad/s]	T_d [s]	ξ[%]	m [$10^6 kg$]	k [MN/m]	$\frac{k}{k_g}$ [MN]	c_{quad} [kN/(m/s)²]	A_{cr} [MN] $\beta = 0.5$	$\beta = 1$	$\beta = 2$
1	0.06	106.7	0.46	86.86	0.3	77.9	182.7	32.72	15.00	1.44
2	0.11	57.0	0.47	50.72	0.6	127.4	97.2	53.70	24.66	2.39
3	0.20	31.8	0.47	84.22	3.3	217.6	194.8	91.86	42.21	4.09
4	0.29	22.0	0.49	57.03	4.7	309.3	117.8	132.72	61.48	6.11
5	0.40	15.6	0.64	69.97	11.4	409.7	188.6	191.80	92.79	10.51
6	0.50	12.7	0.82	53.49	13.2	662.6	156.0	336.64	169.67	21.72
7	0.53	11.9	1.03	71.05	19.7	393.8	262.0	216.18	113.26	16.29
8	0.66	9.5	2.01	60.21	26.6	651.3	154.0	446.18	261.13	52.35
9	0.70	9.0	1.36	38.00	18.7	380.9	35.2	228.85	125.44	20.65
10	0.82	7.7	2.89	59.52	39.7	512.3	157.2	396.34	246.51	59.31

6.3.1 Swell

6.3.1.1 100-year

The considered axial force spectral density due to a 100-year swell condition on K11 is shown in Figure 6-5, together with the frequency range corresponding to the peak of the spectral density for a specified 95% drop from the peak value. More details about the specific values corresponding to the segment are given in Table 6-2.

An analysis of the robustness of K11 due to the given axial force spectral density was conducted, in line with the presented procedure in Section 3. The results based on a frequency ratio $\beta = 2$ are summarized in Table 6-3. As indicated in the table, mode 4 exceeds the onset criterion by a significant amount. Due to the fact that the quadratic damping of the studied mode is low, the resulting estimated terminal response level is clearly unacceptable. The sensitivity to an increase in axial force of 20% and a reduction of the quadratic damping of 20%, denoted by an asterisk in the table, is also significant.
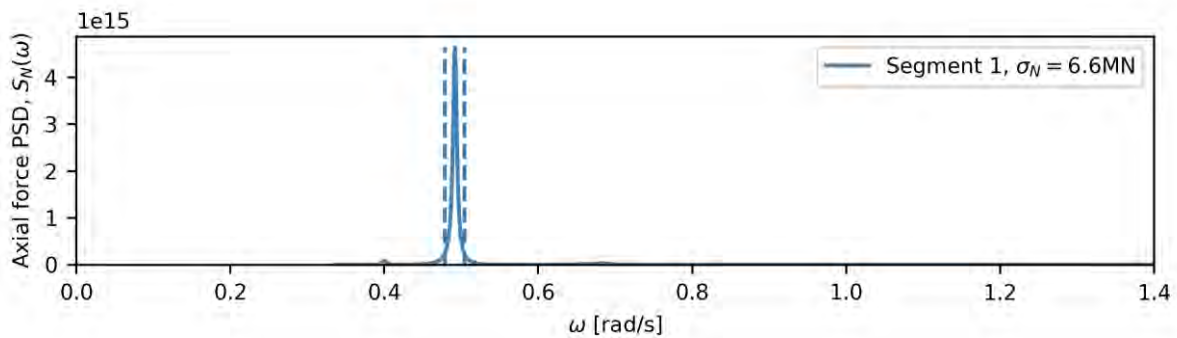
Figure 6-5. Spectral density of axial force variation on K11 due to 100-year swell. The segment lines indicate what frequency ranges to consider for terminal level estimation.

Table 6-2. Segments defined from spectral density of axial force variation on K11 due to 100-year swell.

Segment	σ_N [MN]	Harmonic, N [MN]	ω_p [rad/s]	Trigger ranges [rad/s]		
				$\beta = 0.5$	$\beta = 1.0$	$\beta = 2.0$
1	6.6	24.65	0.4918	0.9566–1.0087	0.4783–0.5044	0.2392–0.2522

Table 6-3. Harmonic results for $\beta = 2.0$, for 100-year swell on K11. The listed β-value corresponds to the frequency ratio between the peak of the axial force spectral density and damped natural frequency of the listed mode. y_0 denotes the generalized response, whereas S_z denotes the bending stress about the strong axis. The asterisk-denoted response values are corresponding to results including uncertainty, characterized by an increase of σ_N of 20% and decrease of quadratic damping (c_{quad}) of 20%. The harmonic amplitude N is established based on an exceedance probability of 10^{-3}.

Mode	ω_d +/- 20% [rad/s]	Segment	β	A_{cr} [MN]	$\sigma_N/0.4$ [MN]	Onset	N [MN]	y_0 (y_0^*)	S_z (S_z^*) [MPa]
4	0.229–0.343	1	1.72	6.11	16.58	fails	24.6	17.09 (27.05)	475.26 (752.05)

To assess the validity of the observed results, a Monte Carlo simulation of mode 4 was conducted with axial force variation characterized by the spectral density from the selected 100-year swell condition. Prior to Monte Carlo simulation, the spectral density was adjusted to have a frequency ratio to mode 4 of exactly 2.0, as indicated in Figure 6-6. The external flat-spectrum force power spectral density, characterizing the external white-noise excitation applied, is also indicated in the figure. The difference between the maximum generalized response with and without parameter variation from all simulations are shown in the probability paper in Figure 6-7. It is highlighted that the probability paper indicated in the figure is close-to linear (not illustrated). The estimated terminal level, due to a Rayleigh distribution with exceedance probability of 0.3%, corresponding to an exceedance probability of 0.1% of a 1hr simulation (scaled to ensure 500 cycles), is shown in the same figure. The time series corresponding to the specified exceedance probability of 0.3% (8th largest response) and the largest response in all 2500 realizations are shown in Figure 6-8 and Figure 6-9, respectively. The strong axis bending moments generated by the white noise response alone is shown in Figure 6-10, which indicates that the level of the white noise is plausible and represents a state that realistically could occur. Overall, a decent agreement is observed. In sum, the estimated terminal level is larger than all observed simulated values; however, the Monte Carlo simulation also yields results indicating an unacceptable response due to parametric excitation (almost 200 MPa in strong axis bending stress).
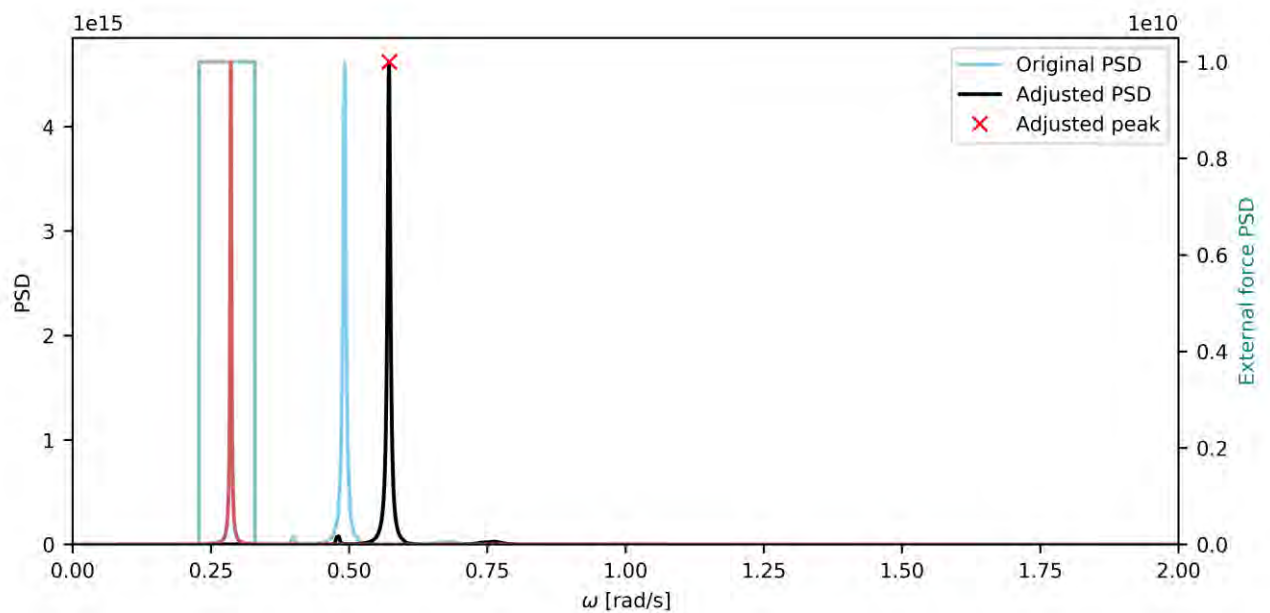
Figure 6-6. Power spectral densities of axial force variation due to 100-year swell conditions and the evenly distributed lateral external force, adjusted to trigger parametric resonance in mode 4 of K11. The red curve indicates the shape and frequency position of the frequency response function of the mode under investigation.
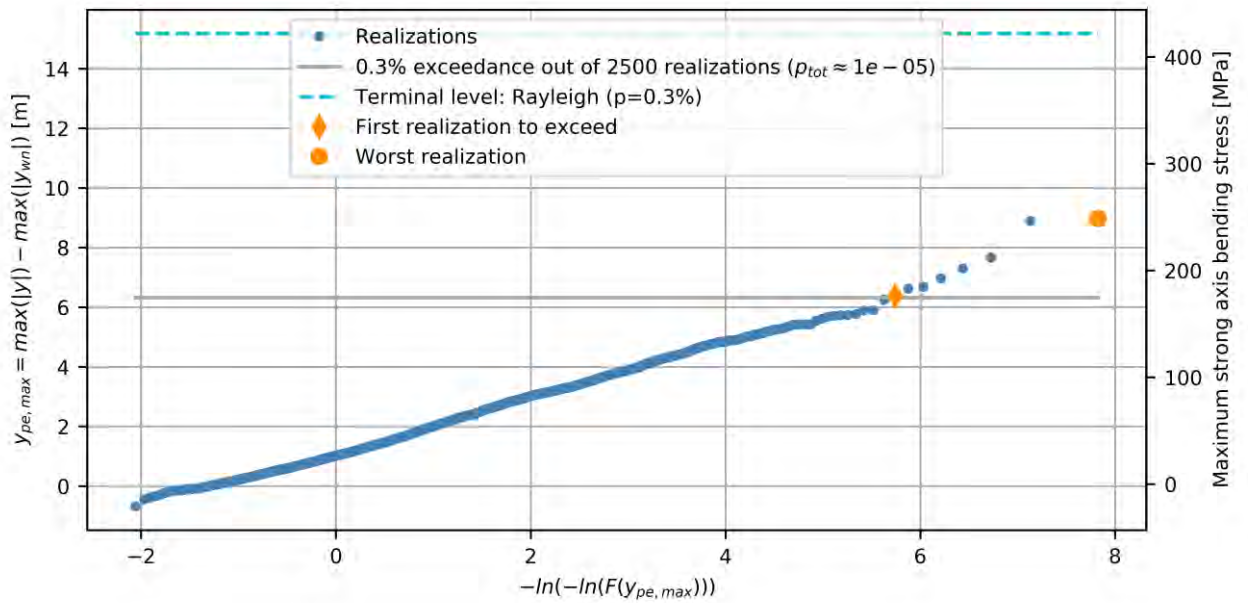
Figure 6-7. Gumbel probability paper of maximum response due to parametric resonance, due to simulated axial force spectral density given in Figure 6-6, which is resulting from a 100-year swell condition. The maximum response from the realization with approximate exceedance probability $p = 0.3\%$ corresponds to the 8th largest realization (out of 2500 realizations in total).

Figure 6-8. The 8th largest response, or the response corresponding to exceedance probability $p = 0.3\%$, corresponding to (♦) in Figure 6-11.
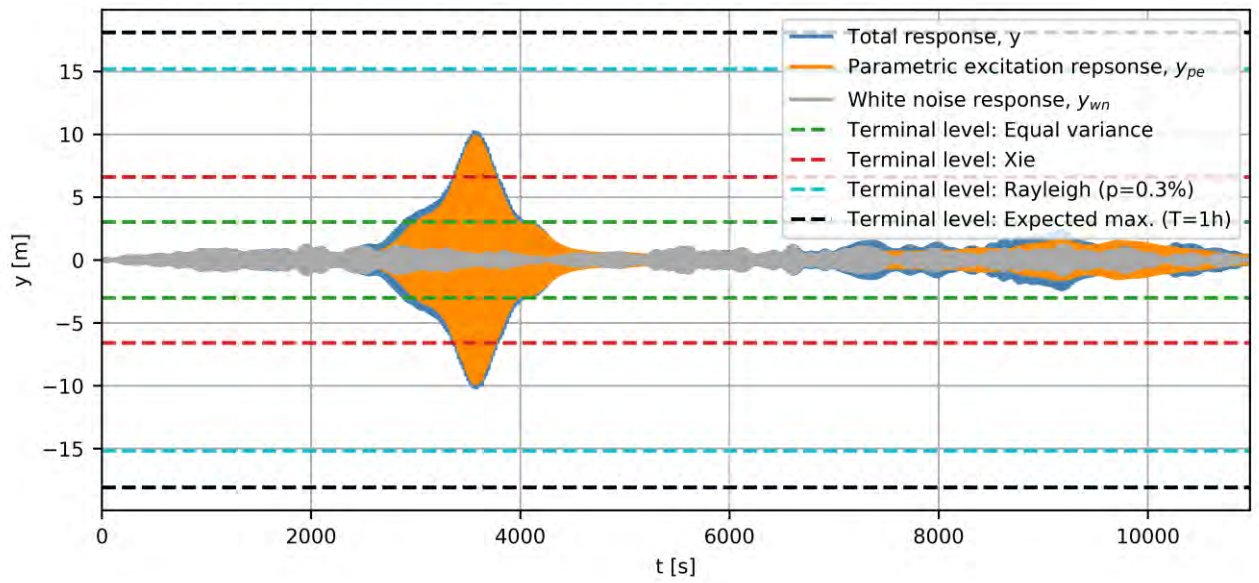
Figure 6-9. Worst realization, corresponding to (•) in Figure 6-11.
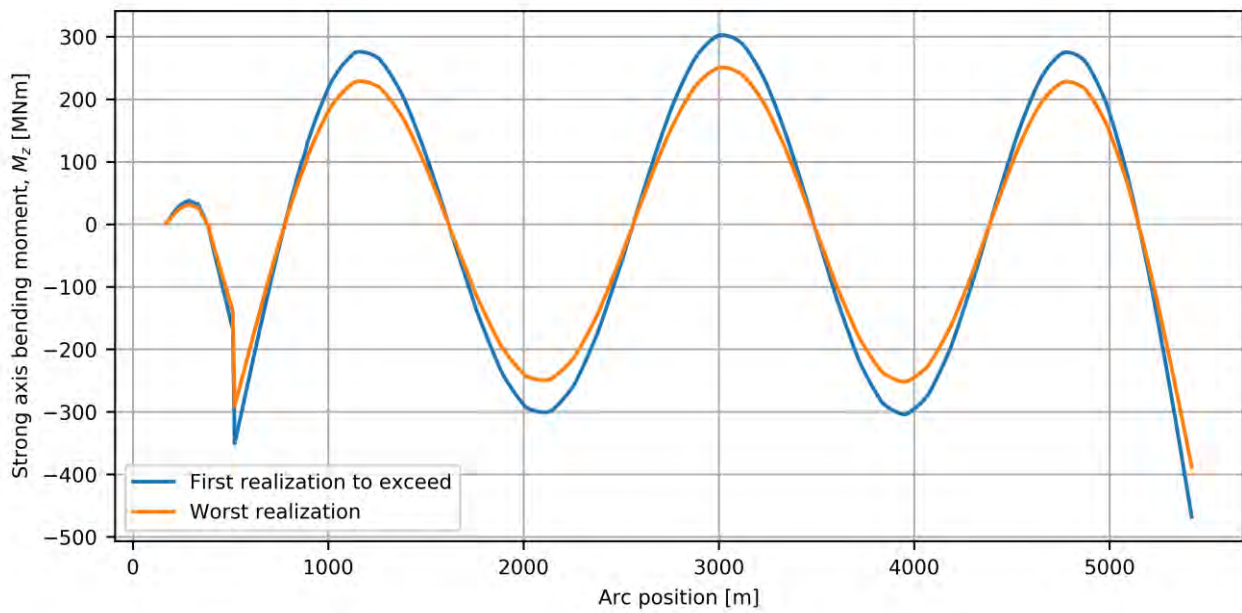
Figure 6-10. Strong axis bending moments due to the applied white noise, for the two selected realizations.

6.3.1.2   10000-year

The considered axial force spectral density due to a 10000-year swell condition on K11 is shown in Figure 6-11, together with the frequency range corresponding to the peak of the spectral density for a specified 95% drop from the peak value. More details about the specific values corresponding to the segment are given in Table 6-4.

Mode 4 is located within the specified range corresponding to $\beta = 2.0$ for the 10000-year swell condition as well, likely to result in parametric excitation. The results are summarized in Table 6-5, and the full results from the analysis are found in Enclosure 2. As for the 100-year swell condition, the onset criterion is exceeded. A slightly lower, yet still unacceptable, terminal response is estimated. The reduced estimate is obtained due to a much lower exceedance probability in the Rayleigh distribution used to establish the harmonic amplitude.
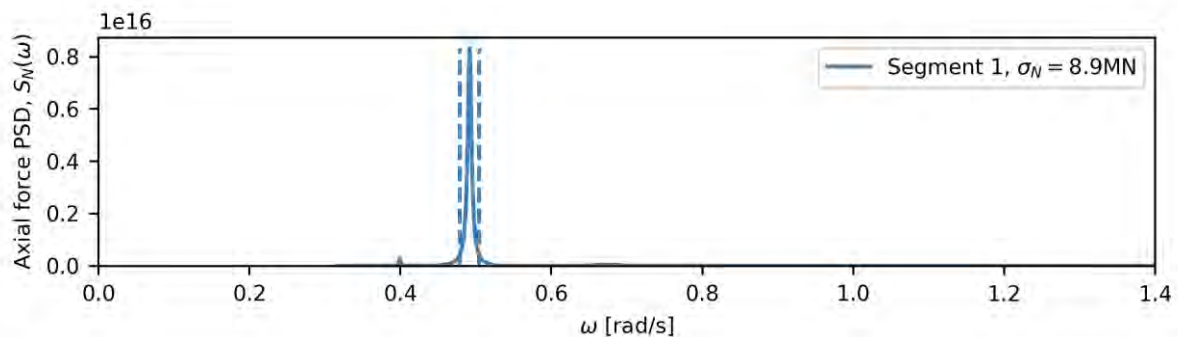
Figure 6-11. Spectral density of axial force variation on K11 due to 10000-year swell. The segment lines indicate what frequency ranges to consider for evaluation of parametric resonance.

Table 6-4. Segments defined from spectral density of axial force variation on K11 due to 10000-year swell.

Segment	σ_N [MN]	Harmonic, N [MN]	ω_p [rad/s]	$\beta = 0.5$	$\beta = 1.0$	$\beta = 2.0$
				Trigger ranges [rad/s]		
1	8.9	19.05	0.4919	0.9570–1.0089	0.4785–0.5045	0.2393–0.2522

Table 6-5. Harmonic results for $\beta = 2.0$, for 10000-year swell on K11. The listed β-value corresponds to the frequency ratio between the peak of the axial force spectral density and damped natural frequency of the listed mode. y_0 denotes the generalized response, whereas S_z denotes the bending stress about the strong axis. The asterisk-denoted response values are corresponding to results including uncertainty, characterized by an increase of σ_N of 20% and decrease of quadratic damping (c_{quad}) of 20%. The harmonic amplitude N is established based on an exceedance probability of 10^{-1}.

Mode	ω_d +/- 20% [rad/s]	Segment	β	A_{cr} [MN]	$\sigma_N/0.4$ [MN]	Onset	N [MN]	y_0 (y_0^*)	S_z (S_z^*) [MPa]
4	0.229–0.343	1	1.72	6.11	22.19	fails	19.05	11.93 (19.30)	331.67 (536.66)

As for the 100-year condition, a Monte Carlo simulation was conducted for mode 4 with the axial force corresponding to the 10000-year swell condition. Prior to Monte Carlo simulation, the spectral density was adjusted to have a frequency ratio to mode 4 of exactly 2.0, as indicated in Figure 6-12. The external flat-spectrum force power spectral density, characterizing the external excitation applied, is also indicated in the figure. The difference between the maximum generalized response with and without parameter variation are shown from all simulations as a probability paper in Figure 6-13. The estimated terminal level, due to a Rayleigh distribution with exceedance probability of 30.5%, corresponding to an exceedance probability of 10% of a 1hr simulation (scaled to ensure 500 cycles), is shown in the same figure. It is highlighted that the probability paper indicated in the figure is close-to linear. The time series corresponding to the specified exceedance probability of 30.5% (3050th largest response) and the largest response in all 10000 realizations are shown in Figure 6-14 and Figure 6-15, respectively. The bending moments generated by the white noise response alone is shown in Figure 6-16 which indicates that the level of the white noise is plausible and represents a state that realistically could occur. A good agreement between the estimated terminal response level and the simulation corresponding to the same probability level is observed; the latter also matches the corresponding level from the 100-year condition very well. The estimated terminal level is slightly above the level estimated using the same probability level from the Gumbel plot. As for the 100-year swell condition, the Monte Carlo simulation yields results indicating an unacceptable response due to parametric excitation (almost 200 MPa in strong axis bending stress). The differences in results of the terminal response estimates from the 100-year and 10000-year swell conditions observed are explained by the treatment of the probability level and is elaborated in Section 3.5.4. The differences reveal that the choice of condition, and thus, exceedance probability, affects the terminal level estimates more than what is observed from the Monte Carlo simulations. However, the conclusion is the same for the two swell conditions considered: parametric excitation due to swell yields unacceptable response of mode 4 of K11.
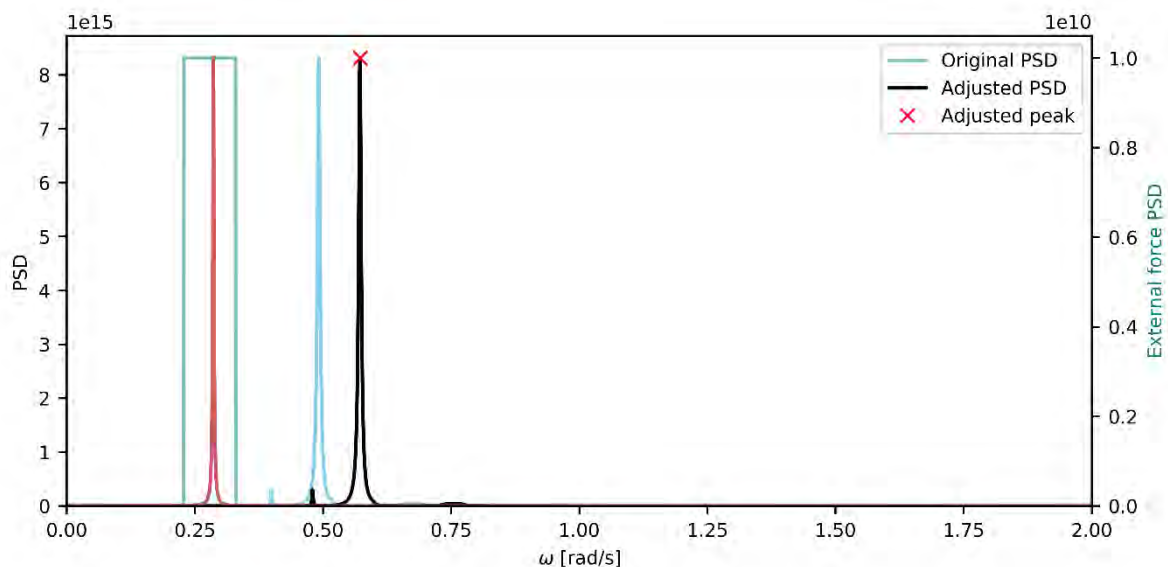
Figure 6-12. Power spectral densities of axial force variation due to 10000-year swell conditions and the evenly distributed lateral external force, adjusted to trigger parametric resonance in mode 4 of K11. The red curve indicates the shape and frequency position of the frequency response function of the mode under investigation.
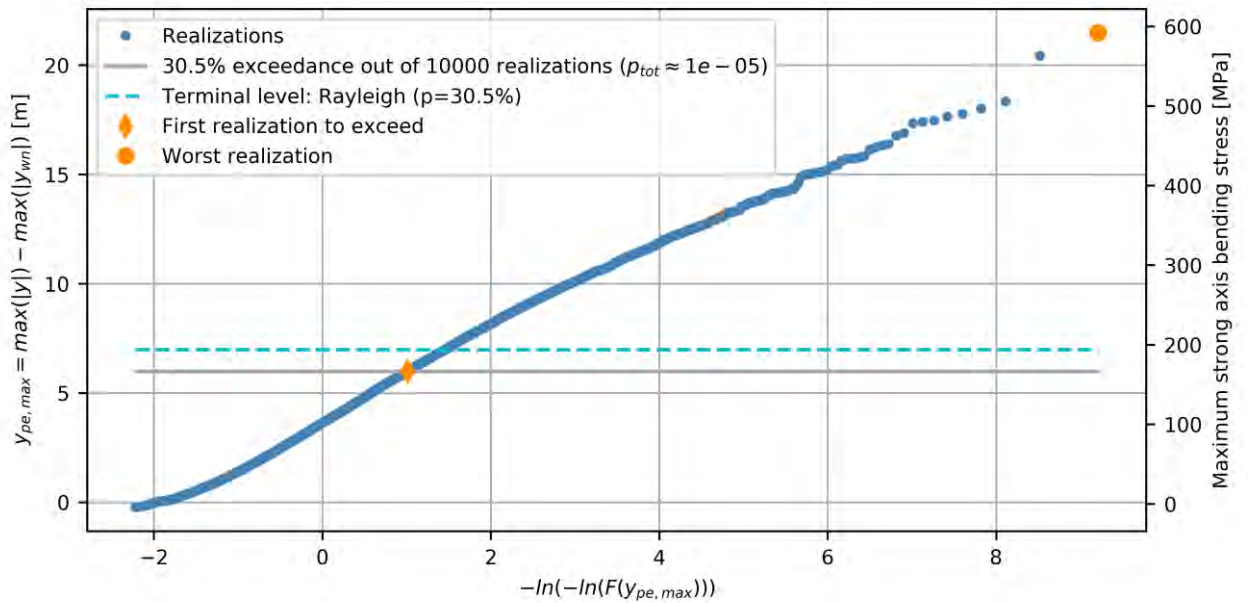
Figure 6-13. Gumbel probability paper of maximum response due to parametric resonance, due to simulated axial force spectral density given in Figure 6-12, which is resulting from a 10000-year swell condition. The maximum response from the realization with approximate exceedance probability $p = 30.5\%$ corresponds to the 30th largest realization (out of 10000 realizations in total).
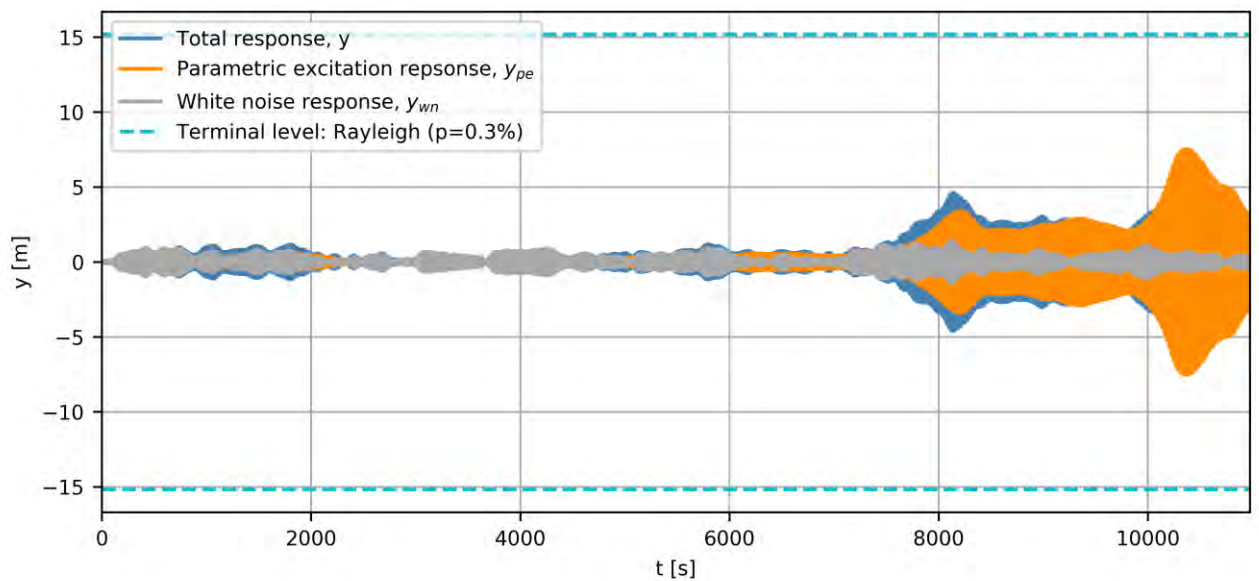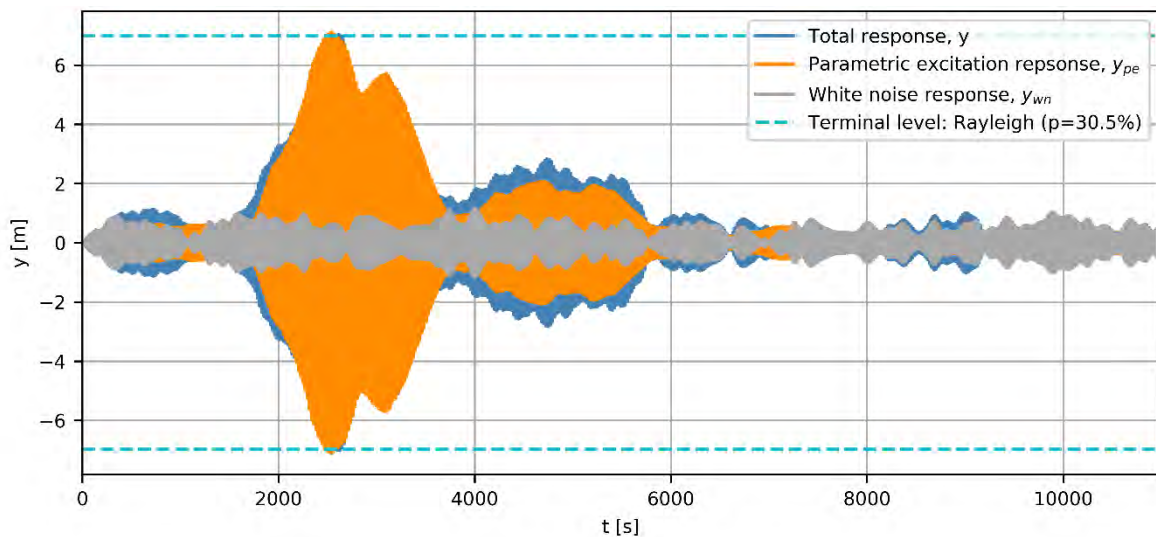

Figure 6-14. The 30th largest response, or the response corresponding to exceedance probability $p = 30.5\%$, corresponding to (♦) in Figure 6-13.
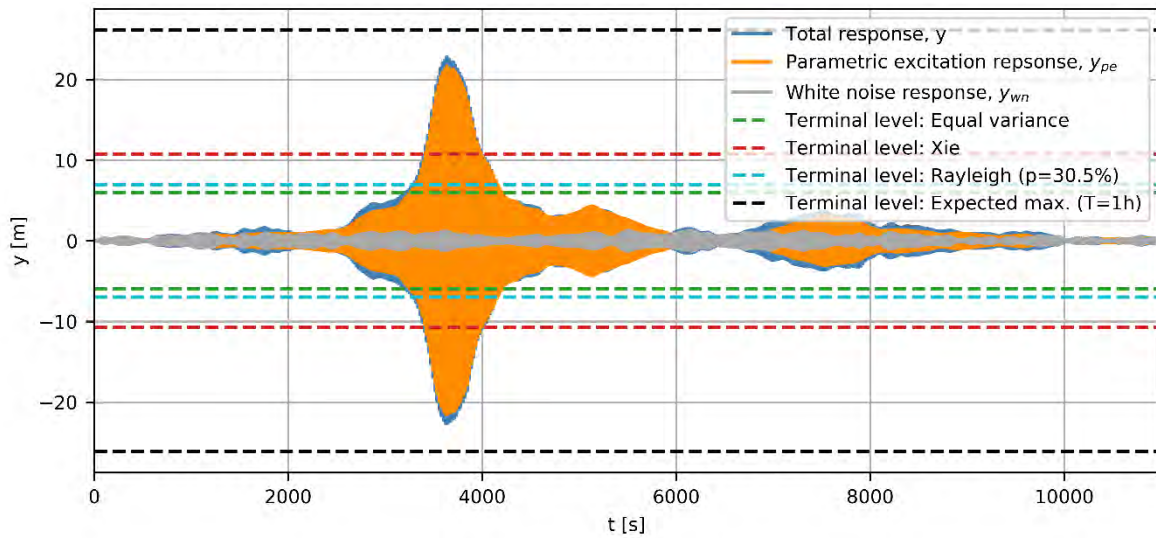
Figure 6-15. Worst realization, corresponding to (•) in Figure 6-13.
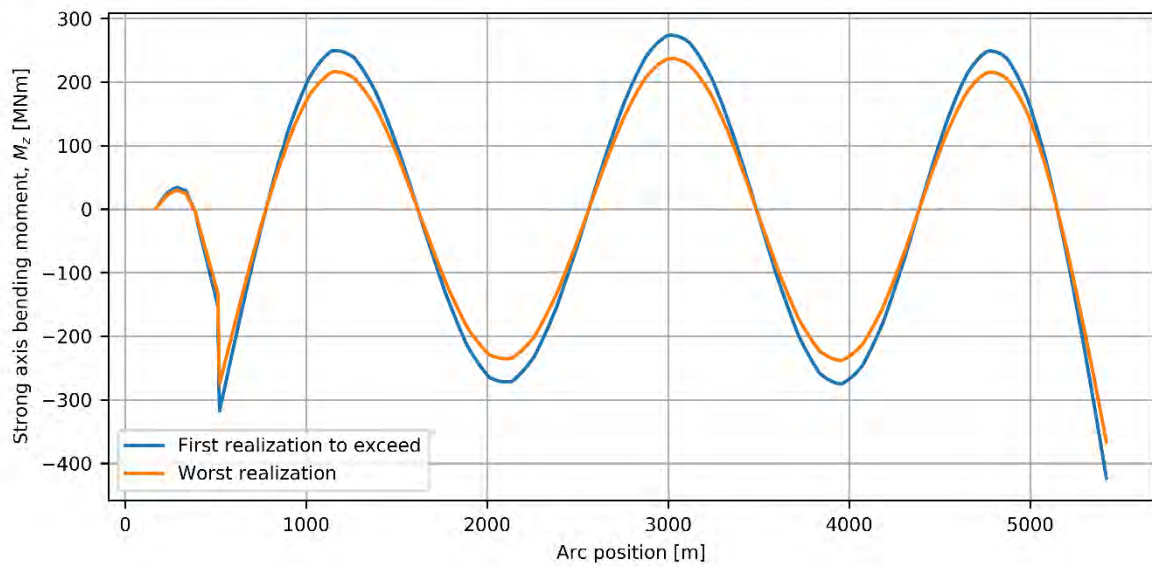
Figure 6-16. Strong axis bending moments due to the applied white noise, for the two selected realizations.

6.3.2 Wind sea

6.3.2.1 100-year

The considered axial force spectral density due to a 100-year wind sea condition on K11 is shown in Figure 6-17, together with the frequency range corresponding to the peak of the spectral density for a specified 90% drop from the peak value. More details about the specific values corresponding to the segment are given in Table 6-6. Based on the shown power spectral density, an analysis of the robustness of K11 was conducted, in line with the presented procedure in Section 3. The results based on a frequency ratio $\beta = 2$ are summarized in Table 6-7. As indicated, when including the aerodynamic damping (see Section 6.6 for details), no modes are exceeded by the onset criterion.
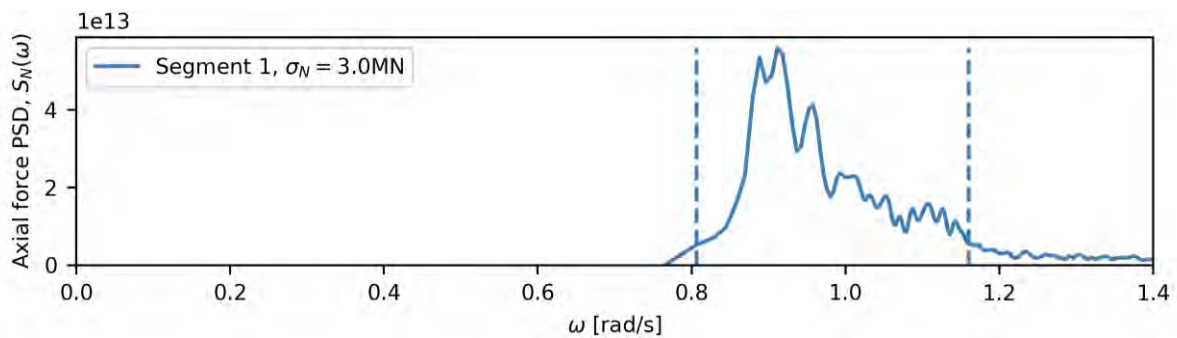
Figure 6-17. Spectral density of axial force variation on K11 due to 100-year wind sea. The segment lines indicate what frequency ranges to consider for evaluation of parametric resonance.

Table 6-6. Segments defined from spectral density of axial force variation on K11 due to 100-year wind sea.

Segment	σ_N [MN]	Harmonic, N [MN]	ω_p [rad/s]	Potential triggering ranges [rad/s]		
				$\beta = 0.5$	$\beta = 1.0$	$\beta = 2.0$
1	3.0	11.1	0.9115	1.6134–2.3207	0.8067–1.1603	0.4033–0.5802

Table 6-7. Harmonic results for $\beta = 2.0$, for 100-year wind sea on K11. The listed β-value corresponds to the frequency ratio between the peak of the axial force spectral density and damped natural frequency of the listed mode. y_0 denotes the generalized response, whereas S_z denotes the bending stress about the strong axis. The asterisk-denoted response values are corresponding to results including uncertainty, characterized by an increase of σ_N of 20% and decrease of quadratic damping (c_{quad}) of 20%. The harmonic amplitude N is established based on an exceedance probability of 10^{-3}.

Mode	ω_d +/- 20% [rad/s]	Segment	β	A_{cr} [MN]	$\sigma_N/0.4$ [MN]	Onset	N [MN]	y_0 (y_0^*)	S_z (S_z^*) [MPa]
5	0.3226–0.4839	1	2.26	20.01	7.46	ok	11.09	0	0
6	0.3967–0.5951	1	1.84	30.47	7.46	ok	11.09	0	0
7	0.4213–0.6319	1	1.73	22.27	7.46	ok	11.09	0	0
8	0.5319–0.7979	1	1.37	59.90	7.46	ok	11.09	0	0
9	0.5611–0.8416	1	1.30	24.47	7.46	ok	11.09	0	0

6.3.2.2 10000-year

Figure 6-18 shows the spectral density of the axial force variation on K11 due to the chosen 10000-year wind sea condition, divided into two different segments and assigned frequency ranges based on a 95% drop from the peak values. More details about the specific values corresponding to the segment are given in Table 6-8. The results from the harmonic analysis of parametric excitation of K11 exposed to 10000-year wind sea excitation, with frequency ratio $\beta = 2$, are summarized in Table 6-9. As indicated, no modes are exceeded by the onset criterion.
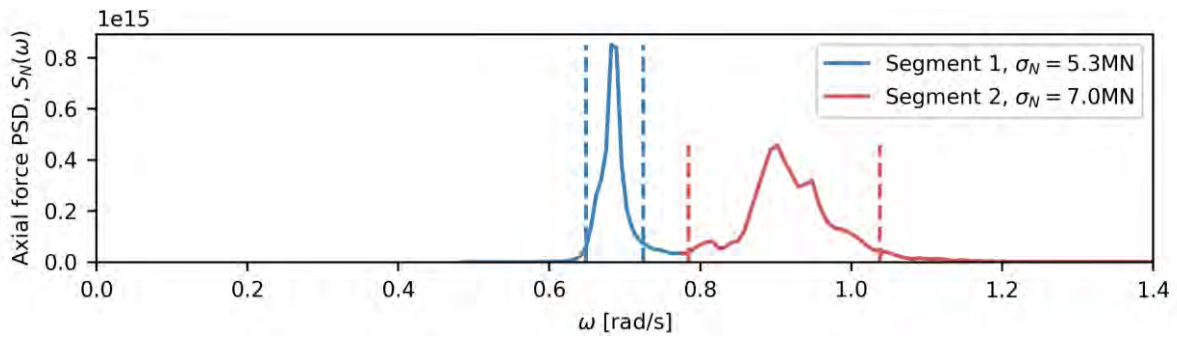
Figure 6-18. Spectral density of axial force variation on K11 due to 10000-year wind sea. The segment lines indicate what frequency ranges to consider for evaluation of parametric resonance.

Table 6-8. Segments defined from spectral density of axial force variation on K11 due to 10000-year wind sea.

| Segment | σ_N [MN] | Harmonic, N [MN] | ω_p [rad/s] | Potential triggering ranges [rad/s] | | |
				$\beta = 0.5$	$\beta = 1.0$	$\beta = 2.0$
1	5.3	11.4	0.6821	1.2978–1.4485	0.6489–0.7242	0.3244–0.3621
2	7.0	15.0	0.9022	1.5689–2.0751	0.7845–1.0375	0.3922–0.5188

Table 6-9. Harmonic results for $\beta = 2.0$, for 10000-year wind sea on K11. The listed β-value corresponds to the frequency ratio between the peak of the axial force spectral density and damped natural frequency of the listed mode. y_0 denotes the generalized response, whereas S_z denotes the bending stress about the strong axis. The asterisk-denoted response values are corresponding to results including uncertainty, characterized by an increase of σ_N of 20% and decrease of quadratic damping (c_{quad}) of 20%. The harmonic amplitude N is established based on an exceedance probability of 10^{-1}.

Mode	ω_d +/- 20% [rad/s]	Segment	β	A_{cr} [MN]	$\sigma_N/0.4$ [MN]	Onset	N [MN]	y_0 (y_0^*)	S_z (S_z^*) [MPa]
4	0.2290–0.3435	1	2.38	18.61	13.33	ok	11.45	0	0
5	0.3226–0.4839	2	2.24	22.14	17.57	ok	15.08	0	0
6	0.3967–0.5951	2	1.82	32.06	17.57	ok	15.08	0	0
7	0.4213–0.6319	2	1.71	23.53	17.57	ok	15.08	0	0

6.3.3   Wind

Figure 6-19 depicts the frequency ratios between all the combinations of the first ten modes of K11. The frequency ratios close to 0.5, 1.0 or 2.0 are highlighted; an uncertainty of 10% is considered for both natural frequencies in each combination. The two following sub-sections provide details regarding the analysis of parametric excitation of K11 due to 100-year and 10000-year wind conditions.
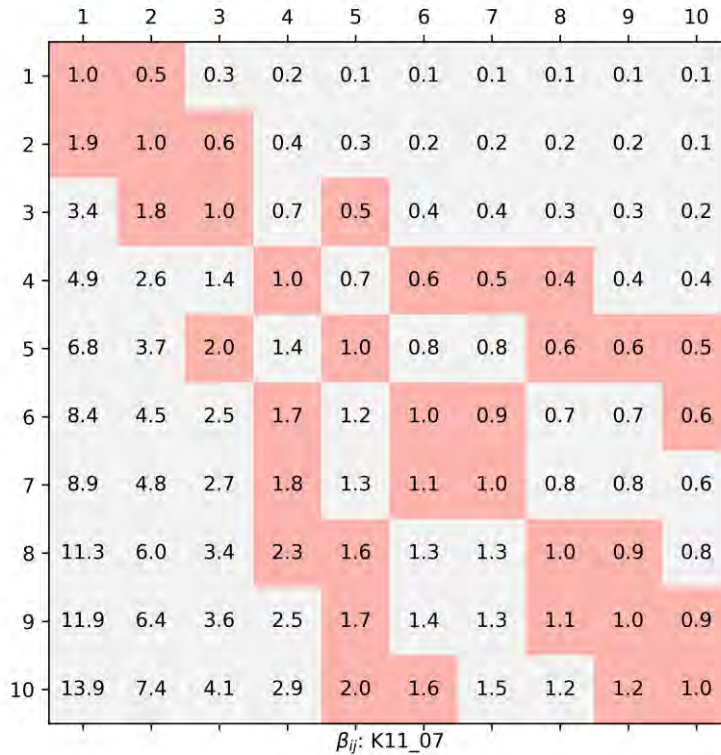
Figure 6-19. Frequency ratios between natural frequencies of K11_07. Frequency ratios close to 0.5, 1.0 or 2.0 are highlighted.

6.3.3.1 100-year

The harshest axial force response on K11 due to 100-year wind is observed for the westerly winds in Table 5-1 (except for mode 11). These standard deviations and the corresponding contribution to the critical damping coefficient from aerodynamic damping are listed in Table 6-10. The onset criterion was assessed based on the given data, producing results as indicated in Enclosure 2. Some of the most important results are given in Table 6-11. As seen, no modes on K11 are parametrically excited by the axial force spectral density resulting from the 100-year wind condition.

Table 6-10: Utilized (westerly winds) aerodynamic damping as a fraction of critical damping and the modal standard deviation for the 100-year wind conditions for K11.

	Aerodynamic critical damping ratio, ξ_{aero}	Standard deviation of axial force, σ_N [MN]
Mode 1	0.0392	-
Mode 2	0.0230	1.42
Mode 3	0.0140	-
Mode 4	0.0093	0.93
Mode 5	0.0066	-
Mode 6	0.0037	2.29
Mode 7	0.0044	-
Mode 8	0.0033	-
Mode 9	0.0025	0.94
Mode 10	0.0025	-
Mode 11	0.0034	0.78
Mode 12	0.0011	-

Table 6-11. Selected harmonic results for $\beta = 0.5, 1.0, 2.0$, for 100-year wind on K11.

Mode pair						
Axial force	Response	β	ξ including aero. [%]	A_{cr} [MN]	$\sigma_N/0.4$ [MN]	Onset
2	1	1.87	4.38	13.66	3.55	ok
6	4	1.73	1.42	17.62	5.72	ok
2	2	1.00	2.77	59.95	3.55	ok
6	7	0.94	1.47	135.23	5.72	ok

6.3.3.2 10000-year

The harshest axial force response on K11 due to 10000-year wind is observed for the westerly winds in Table 5-2. These standard deviations and the corresponding contribution to the critical damping coefficient from aerodynamic damping are listed in Table 6-12. The onset criterion was assessed based on the given data, producing results as indicated in Enclosure 2; of which some of the most important results are reproduced in Table 6-13. As for the 100-year condition, no modes on K11 are parametrically excited by the axial force spectral density resulting from the 10000-year wind condition.

Table 6-12: Modal aerodynamic damping as a fraction of critical damping and the modal standard deviation for the 10000-year wind conditions for K11.

	Aerodynamic critical damping ratio, ξ_{aero}	Standard deviation of axial force, σ_N [MN]
Mode 1	0.0460	-
Mode 2	0.0272	2.40
Mode 3	0.0167	-
Mode 4	0.0111	1.69
Mode 5	0.0079	-
Mode 6	0.0045	4.22
Mode 7	0.0054	-
Mode 8	0.0036	1.70
Mode 9	0.0037	1.66
Mode 10	0.0031	-
Mode 11	0.0024	-
Mode 12	0.0012	-

Table 6-13. Selected harmonic results for $\beta = 0.5, 1.0, 2.0$, for 10000-year wind on K11.

Mode pair						
Axial force	Response	β	ξ including aero. [%]	A_{cr} [MN]	$\sigma_N/0.4$ [MN]	Onset
2	1	1.87	5.06	15.78	6.00	ok
6	4	1.73	1.60	19.84	10.55	ok
6	7	0.94	1.57	139.74	10.55	ok

6.4 K12

The modes of K12 are presented in Figure 6-20 and Table 6-14. The succeeding sub-sections study parametric resonance of the modes from swell, wind sea and wind.

Table 6-14. Modal parameters of K12_06. The aerodynamic damping is not included in the critical damping ratios listed, because they are dependent on the wind speed. It is also assumed that a swell condition can occur without the presence of wind.

Mode	ω_d [rad/s]	T_d [s]	$\xi[\%]$	$m [10^6$ kg]	k [MN/m]	$\frac{k}{k_g}$ [MN]	c_{quad} [kN/(m/s)²]	A_{cr} [MN] $\beta = 0.5$	$\beta = 1$	$\beta = 2$
1	0.11	56.3	0.46	72.34	0.9	271.6	1029.2	113.88	52.15	5.01
2	0.14	43.7	0.47	65.16	1.3	222.3	1997.4	93.68	43.00	4.16
3	0.20	31.0	0.47	61.40	2.5	231.4	1543.3	97.80	44.95	4.37
4	0.29	21.4	0.50	56.70	4.9	345.8	3010.0	149.03	69.18	6.92
5	0.37	16.9	0.58	70.67	9.8	362.9	301.9	164.49	78.30	8.45
6	0.47	13.4	0.82	50.30	11.1	737.6	1928.7	374.52	188.71	24.14
7	0.49	12.7	0.86	77.40	18.9	503.9	2567.9	260.14	132.17	17.33
8	0.61	10.3	1.75	62.04	23.3	620.7	2236.8	406.07	232.24	43.44
9	0.67	9.4	1.28	42.99	19.4	225.8	73.4	132.96	72.14	11.52
10	0.75	8.4	2.56	54.74	30.8	670.4	1445.2	497.74	303.27	68.60

Concept development, floating bridge E39 Bjørnafjorden

Appendix S – Parametric excitation – K12
6 Concept assessments: critical amplitudes and
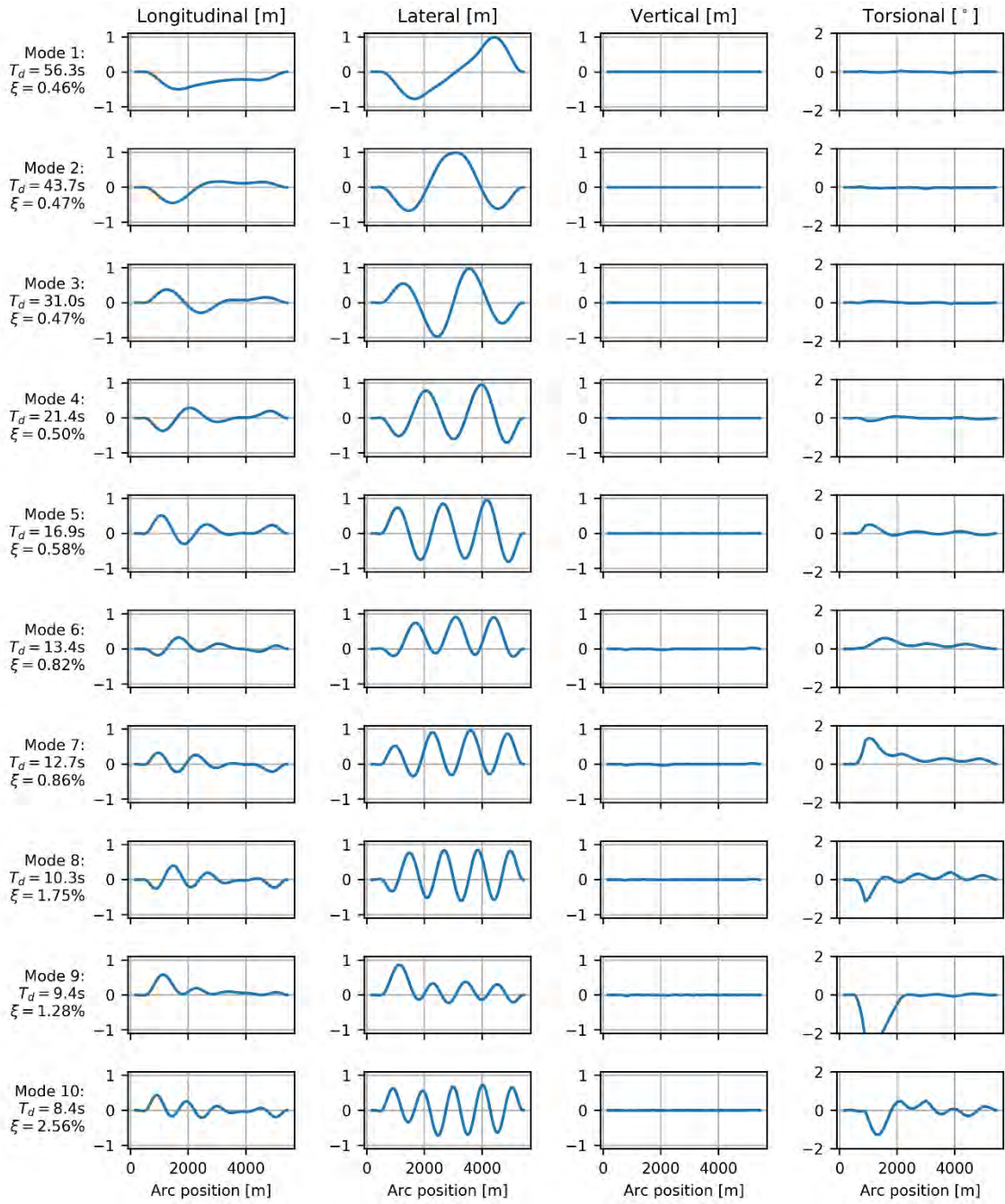terminal level estimates

Figure 6-20. First 10 modes of K12_06.

6.4.1   Swell

6.4.1.1   100-year

The considered axial force spectral density due to a 100-year swell condition on K12 is shown in Figure 6-21, together with the frequency range corresponding to the peak of the spectral density for a specified 95% drop from the peak value. More details about the specific values corresponding to the segment are given in Table 6-15.

An analysis of the robustness of K12 due to the given axial force spectral density was conducted, in line with the presented procedure in Section 3. The results based on a frequency ratio $\beta = 2$ are summarized in Table 6-16. As indicated in the table, mode 3 and 4 exceeds the onset criterion by a moderate amount. Due to the fact that the quadratic damping is mobilized in the modes, the resulting estimated terminal response level considered acceptable (largest bending stress estimated to 25.85 MPa). The sensitivity to an increase in axial force of 20% and a reduction of the quadratic damping of 20%, denoted by an asterisk in the table, is significant but still results in acceptable response values.

Figure 6-21. Spectral density of axial force variation on K12 due to 100-year swell. The segment lines indicate what frequency ranges to consider for evaluation of parametric resonance.

Table 6-15. Segments defined from spectral density of axial force variation on K11 due to 100-year swell.

				Trigger ranges [rad/s]		
Segment	σ_N [MN]	Harmonic, N [MN]	ω_p [rad/s]	$\beta = 0.5$	$\beta = 1.0$	$\beta = 2.0$
1	4.2	15.42	0.4652	0.8712-1.0100	0.4356-0.5050	0.2178-0.2525

Table 6-16. Harmonic results for $\beta = 2.0$, for 100-year swell on K12. The listed β-value corresponds to the frequency ratio between the peak of the axial force spectral density and damped natural frequency of the listed mode. y_0 denotes the generalized response, whereas S_z denotes the bending stress about the strong axis. The asterisk-denoted response values are corresponding to results including uncertainty, characterized by an increase of σ_N of 20% and decrease of quadratic damping (c_{quad}) of 20%. The harmonic amplitude N is established based on an exceedance probability of 10^{-3}.

Mode	ω_d +/- 20% [rad/s]	Segment	β	A_{cr} [MN]	$\sigma_N/0.4$ [MN]	Onset	N [MN]	y_0 (y_0^*)	S_z (S_z^*) [MPa]
3	0.1620–0.2430	1	2.30	4.37	10.38	fails	15.43	1.12 (1.79)	25.85 (41.32)
4	0.2343–0.3515	1	1.59	6.92	10.38	fails	15.43	0.27 (0.46)	7.98 (13.59)

6.4.1.2 10000-year

Figure 6-22 shows the axial force spectral density due to a 10000-year swell condition applied on K12 and the frequency range corresponding to a 95% drop from the peak value. More details about the specific values corresponding to the segment are given in Table 6-17.

The analysis of parametric excitation due to 10000-year swell on K12 is summarized in Table 6-18. As for the 100-year swell condition, modes 3 and 4 of K12 are located within the specified range corresponding to $\beta = 2.0$ for the 10000-year swell condition. The modes also exceed the onset criterion and are thus deemed susceptible to parametric excitation. The estimated terminal response levels are close to the results obtained for the 100-year swell condition: the largest estimated bending stress is 16.24 MPa. The response levels estimated accounting for a 20% reduction in quadratic damping and a 20% increase in the applied axial force amplitude are also acceptable.
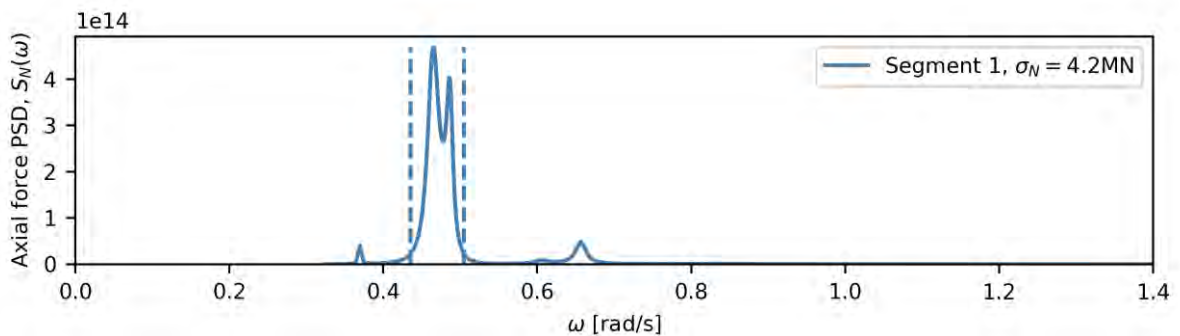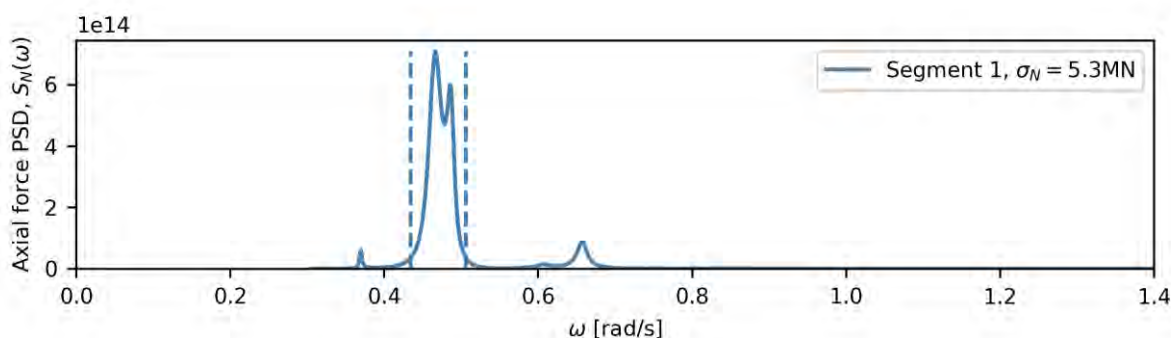

Figure 6-22. Spectral density of axial force variation on K12 due to 10000-year swell. The segment lines indicate what frequency ranges to consider for evaluation of parametric resonance.

Table 6-17. Segments defined from spectral density of axial force variation on K12 due to 10000-year swell.

| Segment | σ_N [MN] | Harmonic, N [MN] | ω_p [rad/s] | Trigger ranges [rad/s] | | |
				$\beta = 0.5$	$\beta = 1.0$	$\beta = 2.0$
1	5.2	11.3	0.4664	0.8684–1.0125	0.4342–0.5062	0.2171–0.2531

Table 6-18. Harmonic results for $\beta = 2.0$, for 10000-year swell on K12. The listed β-value corresponds to the frequency ratio between the peak of the axial force spectral density and damped natural frequency of the listed mode. y_0 denotes the generalized response, whereas S_z denotes the bending stress about the strong axis. The asterisk-denoted response values are corresponding to results including uncertainty, characterized by an increase of σ_N of 20% and decrease of quadratic damping (c_{quad}) of 20%. The harmonic amplitude N is established based on an exceedance probability of 10^{-1}.

Mode	ω_d +/- 20% [rad/s]	Segment	β	A_{cr} [MN]	$\sigma_N/0.4$ [MN]	Onset	N [MN]	y_0 (y_0^*)	S_z (S_z^*) [MPa]
3	0.1620–0.2430	1	2.30	4.37	13.19	fails	11.32	0.70 (1.17)	16.24 (26.92)
4	0.2343–0.3515	1	1.59	6.92	13.19	fails	11.32	0.14 (0.27)	4.12 (7.81)

The validity of the terminal level estimate of mode 3 is assessed by Monte Carlo simulation. Prior to Monte Carlo simulation, the spectral density of the axial force was frequency-shifted such that the peak had a frequency ratio to mode 3 of exactly 2.0, as indicated in Figure 6-23. The external flat-spectrum force power spectral density is also indicated in the figure. The difference between the maximum generalized response with and without parameter variation are shown from all simulations as a probability paper in Figure 6-24. The linearity of the sample points in the probability paper is reasonably good, and in particular, it is satisfactory given the low response values. The estimated terminal level, due to a Rayleigh distribution with exceedance probability of 43.1%, corresponding to an exceedance probability of 10% of a 1hr simulation (scaled to ensure 500 cycles of mode), is shown in the same figure. The estimated terminal response yields a maximum displacement of 0.25m of the girder and a maximum strong axis bending stress of almost 6 MPa. Even though this clearly represents an acceptable response, it seems to be too conservative, when comparing the result with the Monte Carlo simulations. The time series corresponding to the specified exceedance probability of 43.1% (4310th largest response) is shown in Figure 6-25. Still, the Monte Carlo simulation support the conclusion from the terminal level estimate: parametric excitation due to swell on K12 may occur, but the likely effects on the response are acceptable.
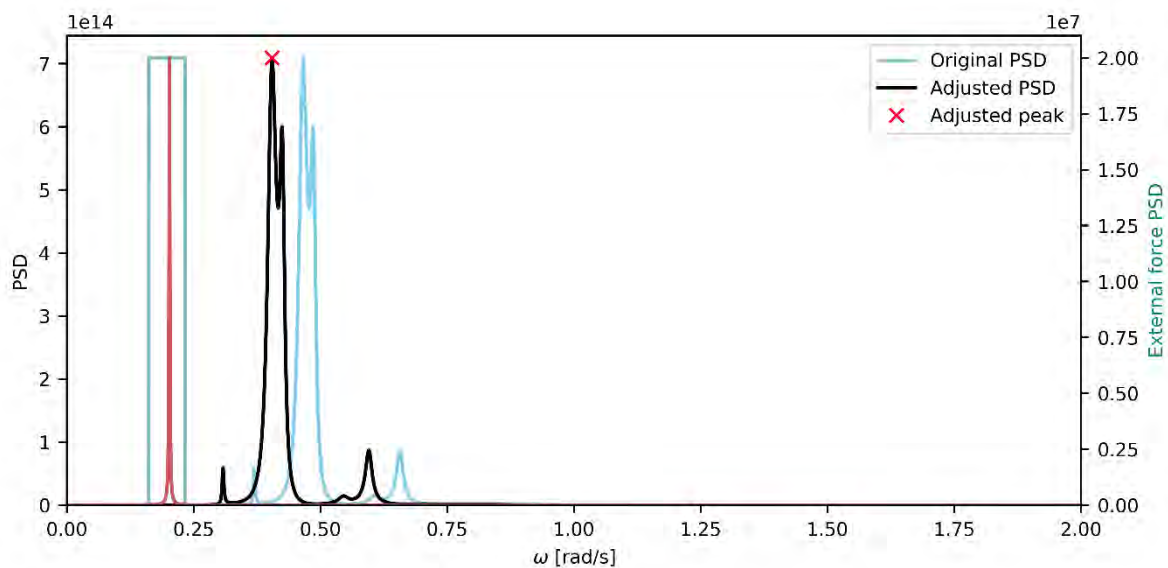
Figure 6-23. Power spectral densities of axial force variation due to 10000-year swell conditions and the evenly distributed lateral, external force, adjusted to trigger parametric resonance in mode 3 of K12. The red curve indicates the shape and frequency position of the frequency response function of the mode under investigation.

Concept development, floating bridge E39 Bjørnafjorden

Appendix S – Parametric excitation – K12   6 Concept assessments: critical amplitudes and
terminal level estimates
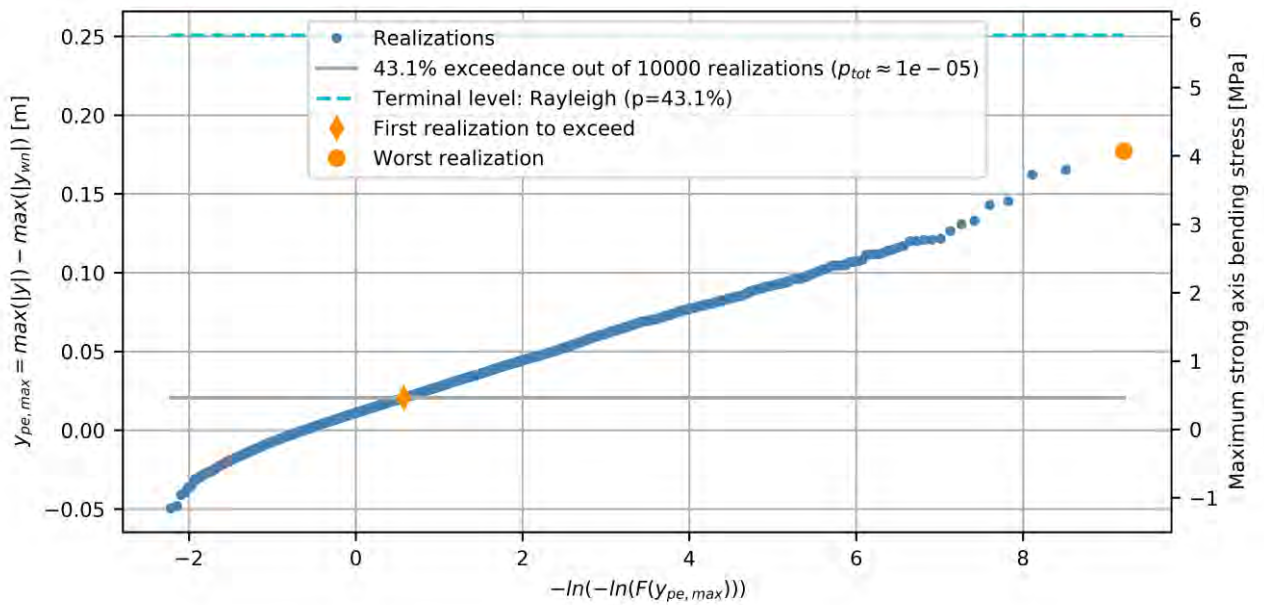
Figure 6-24. Gumbel probability paper of maximum response due to parametric resonance, due to simulated axial force spectral density given in Figure 6-23, which is resulting from a 10000-year swell condition. The maximum response from the realization with approximate exceedance probability $p = 43.1\%$ corresponds to the 4310th largest realization (out of 10000 realizations in total).
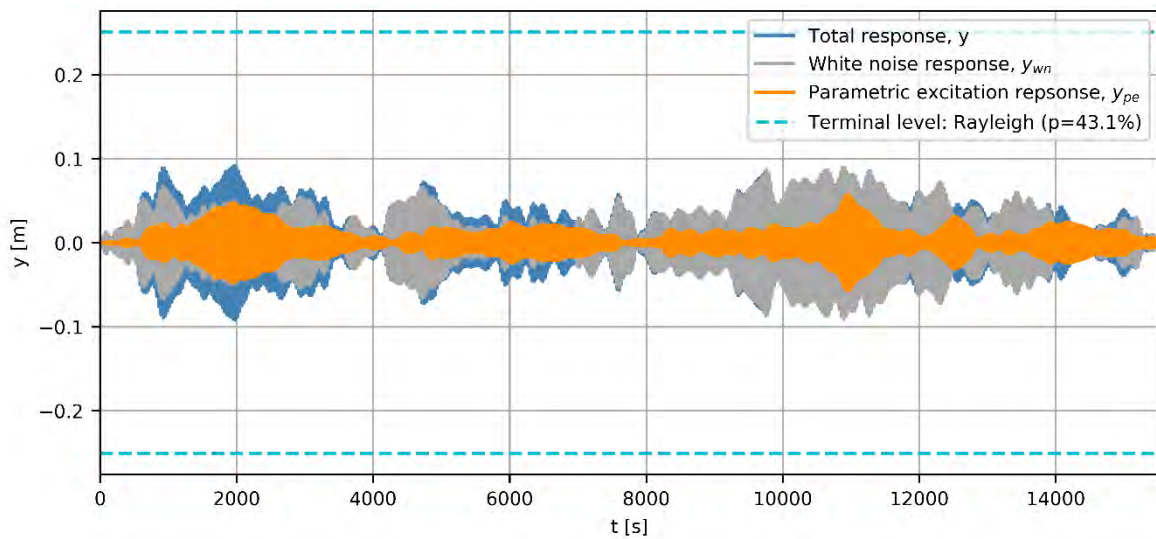
Figure 6-25. The 4310th largest response out of 10000 realizations, or the response corresponding to exceedance probability $p = 43.1\%$, corresponding to ($\blacklozenge$) in Figure 6-24.

6.4.2 Wind sea

6.4.2.1 100-year

Figure 6-26 shows the axial force spectral density due to a 100-year wind sea condition applied on K12 and the frequency range corresponding to a 90% drop from the peak value. More details about the specific values corresponding to the segment are given in Table 6-19. The results from the harmonic analysis of parametric excitation of K12 exposed to 100-year wind sea excitation, with frequency ratio $\beta = 2$, are summarized in Table 6-20. As the table indicates, the onset criterion is not exceeded for any modes.

Figure 6-26. Spectral density of axial force variation on K12 due to 100-year wind sea. The segment lines indicate what frequency ranges to consider for evaluation of parametric resonance.

Table 6-19. Segments defined from spectral density of axial force variation on K12 due to 100-year wind sea.

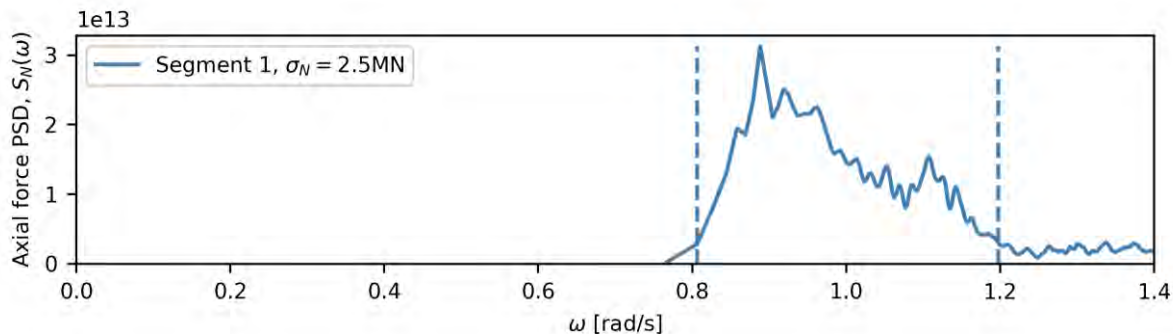|				Trigger ranges [rad/s]		
Segment	σ_N [MN]	Harmonic, N [MN]	ω_p [rad/s]	$\beta = 0.5$	$\beta = 1.0$	$\beta = 2.0$
1	2.5	9.45	0.8883	1.6134–2.3951	0.8067–1.1976	0.4033–0.5988

Table 6-20. Harmonic results for $\beta = 2.0$, for 100-year wind sea on K12. The listed β-value corresponds to the frequency ratio between the peak of the axial force spectral density and damped natural frequency of the listed mode. y_0 denotes the generalized response, whereas S_z denotes the bending stress about the strong axis. The asterisk-denoted response values are corresponding to results including uncertainty, characterized by an increase of σ_N of 20% and decrease of quadratic damping (c_{quad}) of 20%. The harmonic amplitude N is established based on an exceedance probability of 10^{-3}.

Mode	ω_d +/- 20% [rad/s]	Segment	β	A_{cr} [MN]	$\sigma_N/0.4$ [MN]	Onset	N [MN]	y_0 (y_0^*)	S_z (S_z^*) [MPa]
5	0.2980–0.4470	1	2.38	17.59	6.35	ok	9.45	0	0
6	0.3756–0.5634	1	1.89	38.60	6.35	ok	9.45	0	0
7	0.3957–0.5936	1	1.80	24.59	6.35	ok	9.45	0	0
8	0.4898–0.7346	1	1.45	51.39	6.35	ok	9.45	0	0
9	0.5372–0.8058	1	1.32	13.78	6.35	ok	9.45	0	0

6.4.2.2 *10000-year*

The spectral density of the axial force variation on K12 from 10000-year wind sea is shown in Figure 6-27. The spectral density is divided into two different segments and assigned frequency ranges based on a 90% drop from the peak values. More details about the specific values corresponding to the segment are given in Table 6-21. The results from the harmonic analysis of parametric excitation of K12 exposed to 10000-year wind sea excitation, with frequency ratio $\beta = 2$, are summarized in Table 6-22. As for the 100-year wind sea condition, the onset criterion is not exceeded for any modes.
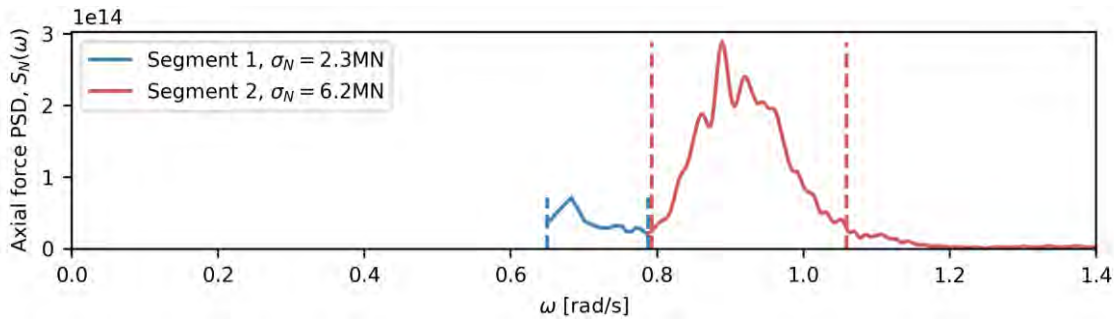

Figure 6-27. Spectral density of axial force variation on K12 due to 10000-year wind sea. The segment lines indicate what frequency ranges to consider for evaluation of parametric resonance

Table 6-21. Segments defined from spectral density of axial force variation on K11 due to 10000-year wind sea.

| Segment | σ_N [MN] | Harmonic, N [MN] | ω_p [rad/s] | Triggering ranges [rad/s] | | |
				$\beta = 0.5$	$\beta = 1.0$	$\beta = 2.0$
1	2.3	4.96	0.6826	1.2993–1.5752	0.6497–0.7876	0.3248–0.3938
2	6.2	13.4	0.8890	1.5851–2.1175	0.7926–1.0588	0.3963–0.5294

Table 6-22. Harmonic results for $\beta = 2.0$, for 10000-year wind sea on K12. The listed β-value corresponds to the frequency ratio between the peak of the axial force spectral density and damped natural frequency of the listed mode. y_0 denotes the generalized response, whereas S_z denotes the bending stress about the strong axis. The asterisk-denoted response values are corresponding to results including uncertainty, characterized by an increase of σ_N of 20% and decrease of quadratic damping (c_{quad}) of 20%. The harmonic amplitude N is established based on an exceedance probability of 10^{-1}.

Mode	ω_d +/- 20% [rad/s]	Segment	β	A_{cr} [MN]	$\sigma_N/0.4$ [MN]	Onset	N [MN]	y_0 (y_0^*)	S_z (S_z^*) [MPa]
4	0.2980–0.4470	1	2.33	19.51	5.77	ok	4.96	0	0
5	0.2980–0.4470	2	2.39	19.77	15.61	ok	13.4	0	0
6	0.3756–0.5634	2	1.89	41.84	15.61	ok	13.4	0	0
7	0.3957–0.5936	2	1.80	26.00	15.61	ok	13.4	0	0
8	0.4898–0.7346	2	1.45	53.13	15.61	ok	13.4	0	0

Mode 5 is considered the most critical in the preceding analysis, and Monte Carlo simulation is carried out to verify the findings. Prior to Monte Carlo simulation, the peak of the spectral density is shifted in frequency such that it has a ratio to the natural frequency of mode 5 of exactly 2.0, as indicated in Figure 6-28. The external flat-spectrum force power spectral density is also indicated in the figure. The results conducted with the full damping present, i.e., including the aerodynamic contributions, supports the results in the harmonic analysis summarized in Table 6-22: no parametric excitation is observed. Monte Carlo simulation was therefore conducted on the system excluding the aerodynamic damping, which clearly is a highly conservative approach.

The difference between the resulting maximum generalized response with and without parameter variation are shown from all simulations as a Gumbel probability paper in Figure 6-29. The estimated terminal level, due to a Rayleigh distribution with exceedance probability of 23.4% (scaled to a duration corresponding to 500 cycles) is shown in the same figure. The linearity of the sample points in the probability paper is rather poor, but will produce conservative estimates if the lowest response values are used to produce a linear fit. The observed value with the given exceedance probability based on all the sampled simulations is significantly lower than the estimated terminal level. This is as expected due to the broad-bandedness of the axial force variation from wind sea excitation. As this example illustrates, the parametric excitation of K12 due to wind sea excitation under the assumption of no aerodynamic damping is considered unproblematic.
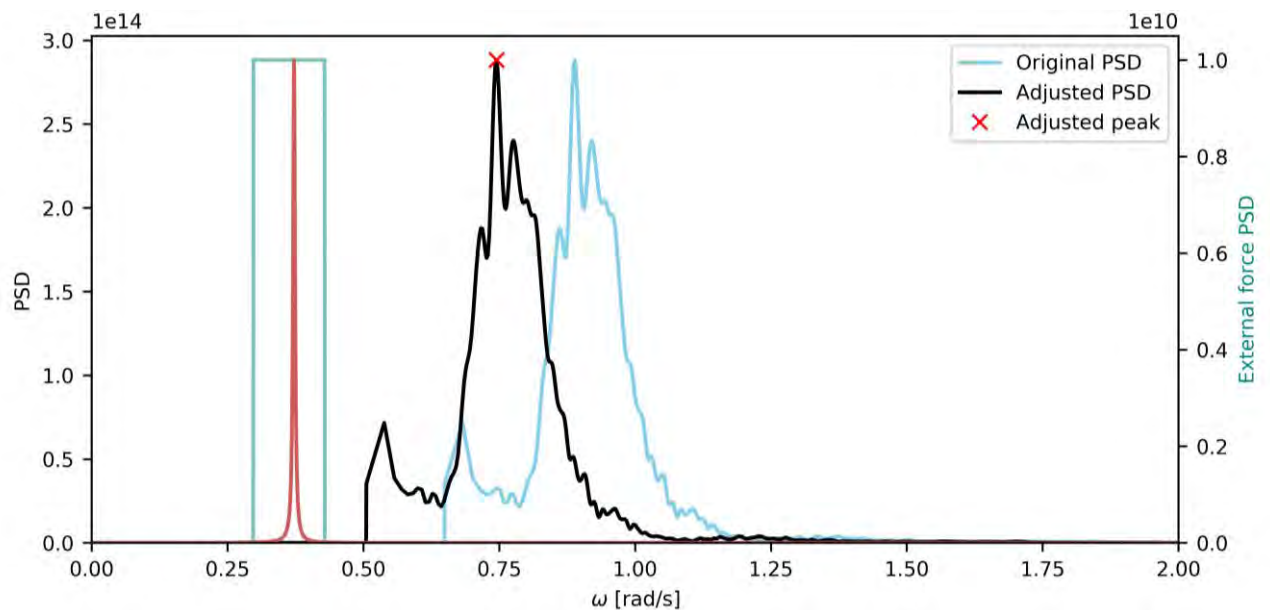
Figure 6-28. Power spectral densities of axial force variation due to a 10000-year wind sea condition and the evenly distributed lateral external force, adjusted to trigger parametric resonance in mode 5 of K12. The red curve indicates the shape and frequency position of the frequency response function of the mode under investigation.
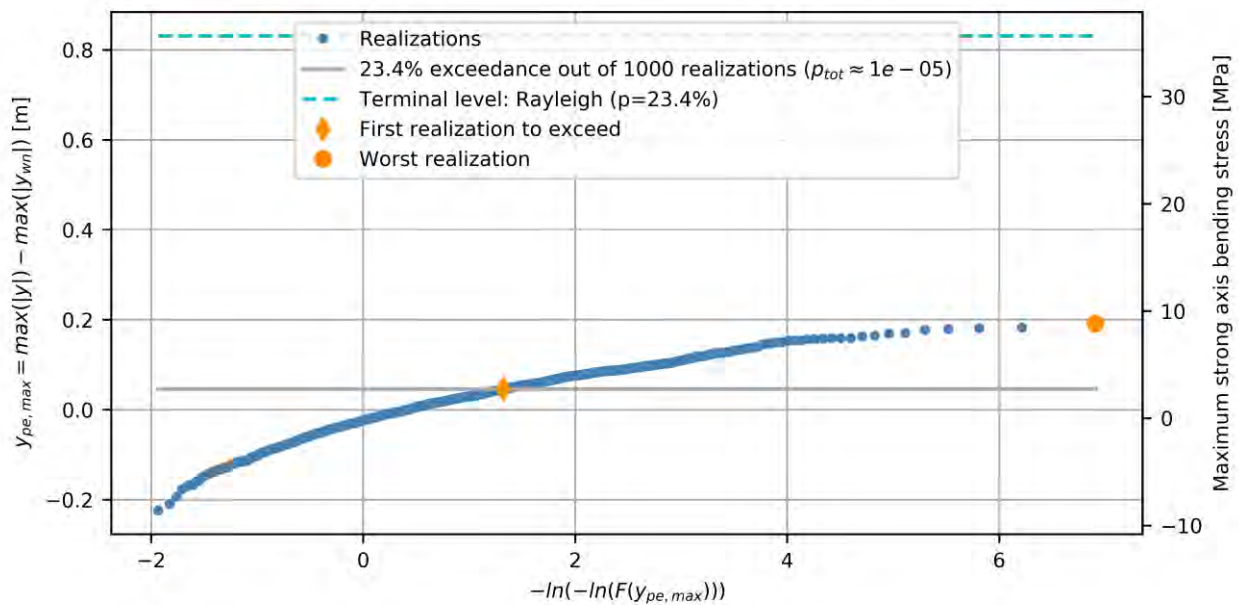
Figure 6-29. Gumbel probability paper of maximum response of mode 5 on K12 due to parametric resonance, due to simulated axial force spectral density given in Figure 6-28, which is resulting from a 10000-year wind sea condition. The maximum response from the realization with approximate exceedance probability $p = 30.4\%$ corresponds to the 30th largest realization (out of 1000 realizations in total).
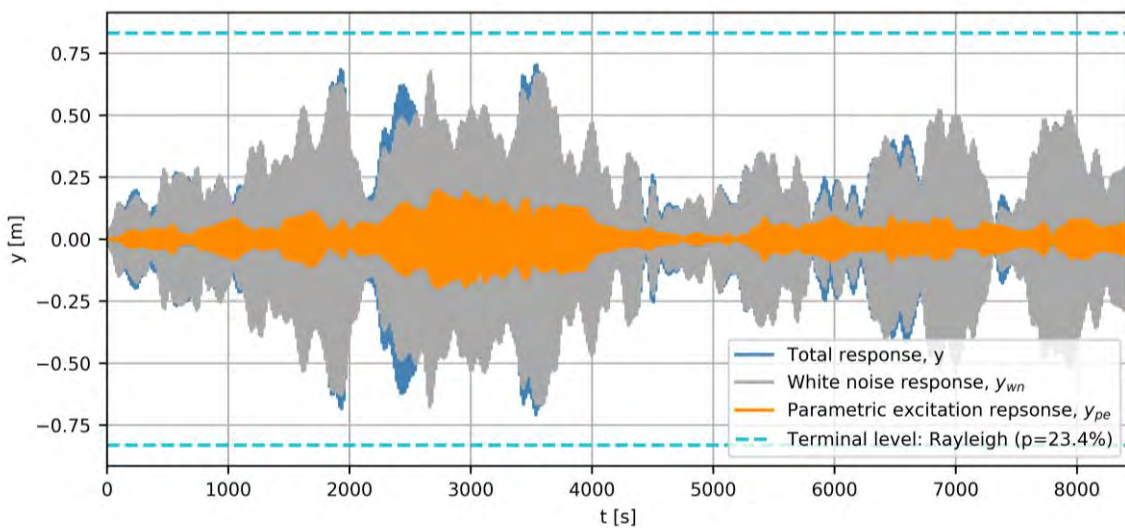
Figure 6-30. The 234th largest response out of 1000 realizations, or the response corresponding to exceedance probability $p = 23.4\%$, corresponding to (♦) in Figure 6-28.

6.4.3 Wind

Figure 6-31 depicts the frequency ratios between all the combinations of the first ten modes of K12. The frequency ratios close to 0.5, 1.0 or 2.0 are highlighted; an uncertainty of 10% is considered for both natural frequencies in each combination. The two following sub-sections provide details regarding the analysis of parametric excitation of K12 due to 100-year and 10000-year wind conditions.
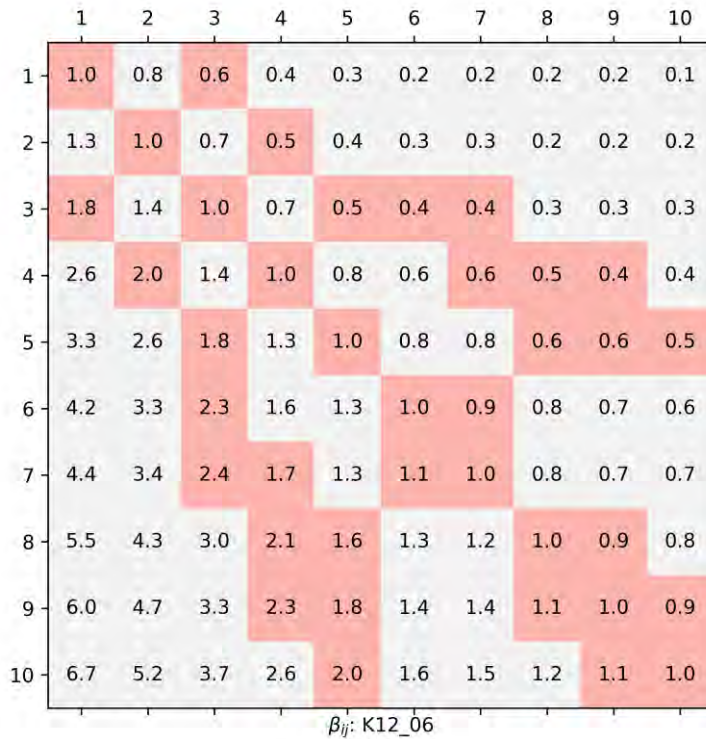
Figure 6-31. Frequency ratios between natural frequencies of K12_06. Frequency ratios close to 0.5, 1.0 or 2.0 are highlighted.

6.4.3.1 100-year

The harshest axial force response on K12 due to 100-year wind is observed for the westerly winds (except for mode 7) in Table 5-3. These standard deviations and the corresponding contribution to the critical damping coefficient from aerodynamic damping are listed in Table 6-23. The onset criterion was assessed based on the given data, producing results as indicated in Enclosure 2. Some of the most important results are given in Table 6-24. The results indicate that no modes on K12 are susceptible to parametric excitation due to the axial force spectral density resulting from the 100-year wind condition.

*Table 6-23: Utilized (westerly wind) aerodynamic damping as a fraction of critical damping and the modal standard deviation for the 100-year wind conditions for the K12 concept.*

	Aerodynamic critical damping ratio, ξ_{aero}	Standard deviation of axial force, σ_N [MN]
Mode 1	0.0217	-
Mode 2	0.0180	-
Mode 3	0.0126	-
Mode 4	0.0084	0.55
Mode 5	0.0072	-
Mode 6	0.0056	1.49
Mode 7	0.0043	0.59
Mode 8	0.0036	-
Mode 9	0.0029	1.06
Mode 10	0.0027	-
Mode 11	0.0013	-
Mode 12	0.0015	0.50

Table 6-24. Selected harmonic results for $\beta = 0.5, 1.0, 2.0$, for 100-year wind on K12.

Mode pair						
Axial force	Response	β	ξ including aero. [%]	A_{cr} [MN]	$\sigma_N/0.4$ [MN]	Onset
4	2	2.04	2.27	20.16	1.38	ok
6	3	2.32	1.73	16.03	3.73	ok
6	7	0.95	1.29	161.87	3.73	ok

6.4.3.2 10000-year

The harshest axial force response on K12 due to 10000-year wind is observed for the westerly winds (except for mode 7) in Table 5-41. These standard deviations and the corresponding contribution to the critical damping coefficient from aerodynamic damping are listed in Table 6-25. The onset criterion was assessed based on the given data, producing results as indicated in Enclosure 2, of which some of the most important results are reproduced in Table 6-26. As for the 100-year condition, no modes on K12 are parametrically excited by the axial force spectral density resulting from the 10000-year wind condition.

Table 6-25: Utilized (westerly wind) modal aerodynamic damping as a fraction of critical damping and the modal standard deviation for the 10000-year wind conditions for the K12 concept.

	Aerodynamic critical damping ratio, ξ_{aero}	Standard deviation of axial force, σ_N [MN]
Mode 1	0.0260	-
Mode 2	0.0215	-
Mode 3	0.0151	-
Mode 4	0.0101	0.86
Mode 5	0.0086	-
Mode 6	0.0066	2.47
Mode 7	0.0052	0.96
Mode 8	0.0044	-
Mode 9	0.0036	1.72
Mode 10	0.0033	-
Mode 11	0.0016	-
Mode 12	0.0018	0.78

Table 6-26. Selected harmonic results for $\beta = 0.5, 1.0, 2.0$, for 10000-year wind on K12.

Mode pair						
Axial force	Response	β	ξ including aero. [%]	A_{cr} [MN]	$\sigma_N/0.4$ [MN]	Onset
4	2	2.04	2.62	23.28	2.15	ok
6	3	2.32	1.98	18.34	6.17	ok
6	7	0.95	1.38	167.42	6.17	ok

6.5 K14

The modes of K14 are presented in Figure 6-32 and Table 6-27. The succeeding sub-sections study parametric resonance of the modes from swell, wind sea and wind.

Table 6-27. Modal parameters of K14_06. The aerodynamic damping is not included in the critical damping ratios listed, because they are dependent on the wind speed. It is also assumed that a swell condition can occur without the presence of wind.

Mode	ω_d [rad/s]	T_d [s]	ξ[%]	m [10^6 kg]	k [MN/m]	$\frac{k}{k_g}$ [MN]	c_{quad} [kN/(m/s)²]	A_{cr} [MN] $\beta = 0.5$	$\beta = 1$	$\beta = 2$
1	0.15	41.4	0.46	75.74	1.7	1321.9	2755.4	554.90	254.2	24.45
2	0.18	35.0	0.47	63.36	2.0	283.7	1590.6	119.49	54.84	5.30
3	0.25	25.2	0.48	53.42	3.3	354.0	1868.9	150.36	69.29	6.78
4	0.29	21.9	0.49	43.96	3.6	320.0	424.8	137.26	63.57	6.31
5	0.38	16.4	0.62	45.03	6.6	417.1	1260.7	192.67	92.60	10.28
6	0.47	13.3	0.79	52.94	11.9	654.1	1672.1	328.50	164.6	20.71
7	0.56	11.2	1.00	76.37	24.0	2088.8	8773.1	1133.3	590.2	83.40
8	0.62	10.1	1.84	55.09	21.1	843.7	4428.2	561.48	323.8	62.16
9	0.71	8.9	1.57	32.96	16.5	1743.4	281.3	1099.6	617.3	109.23
10	0.75	8.4	2.76	49.31	27.7	867.1	2953.1	660.46	407.6	95.79

Concept development, floating bridge E39 Bjørnafjorden

Appendix S – Parametric excitation – K12
6 Concept assessments: critical amplitudes and
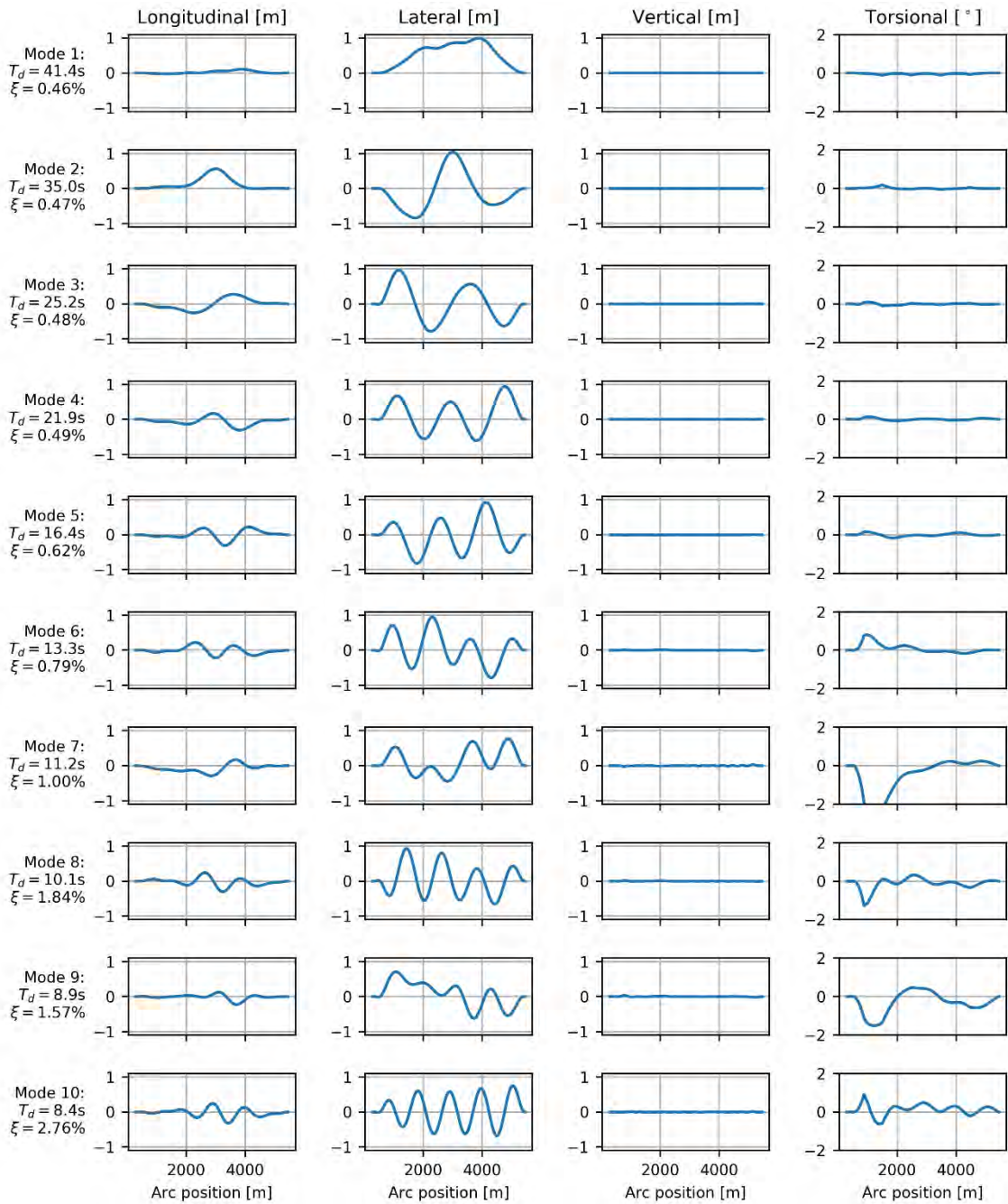terminal level estimates

Figure 6-32. First 10 modes of K14_06.

6.5.1 Swell

6.5.1.1 100-year

The spectral density of the axial force variation on K14 from 100-year swell is shown in Figure 6-33. The spectral density is divided into two different segments and assigned frequency ranges based on a 95% drop from the peak values. More details about the specific values corresponding to the segment are given in Table 6-28.

The analysis of parametric excitation due to 100-year swell on K14 is summarized in Table 6-29. As indicated in the table, modes 3 and 4 of K14 are located within the specified range corresponding to $\beta = 2.0$ for the 100-year swell condition. The modes also exceed the onset criterion and are thus deemed susceptible to parametric excitation. The estimated terminal response levels are deemed acceptable: the largest estimated bending stress is 30.31 MPa. By accounting for a 20% reduction of quadratic damping and a 20% increase of the applied axial force amplitude, the maximum strong axis bending stress is increased to 56.17MPa, which is significant.
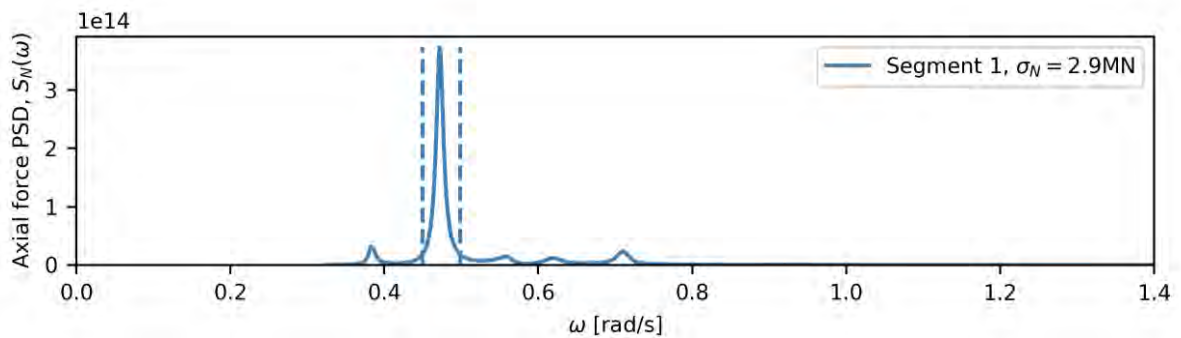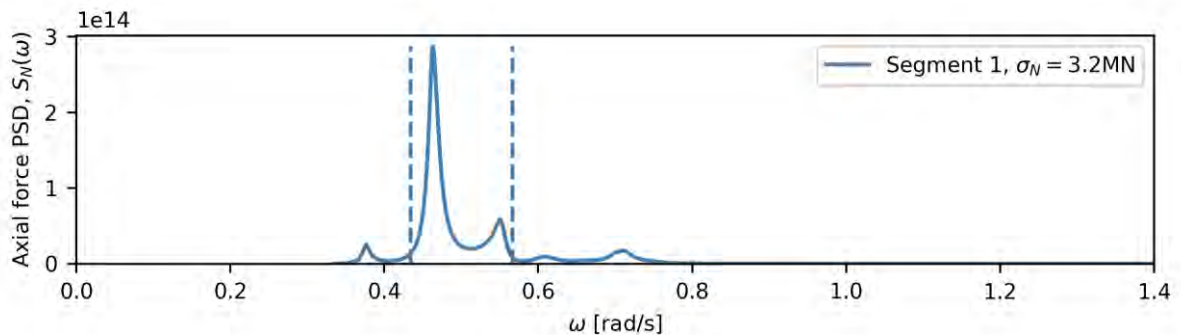

Figure 6-33. Spectral density of axial force variation on K14 due to 100-year swell. The segment lines indicate what frequency ranges to consider for evaluation of parametric resonance.

Table 6-28. Segments defined from spectral density of axial force variation on K14 due to 100-year swell.

| Segment | σ_N [MN] | Harmonic, N [MN] | ω_p [rad/s] | Trigger ranges [rad/s] | | |
				$\beta = 0.5$	$\beta = 1.0$	$\beta = 2.0$
1	2.9	10.7847	0.4720	0.8990–0.9974	0.4495–0.4987	0.2248–0.2493

Table 6-29. Harmonic results for $\beta = 2.0$, for 100-year swell on K14. The listed β-value corresponds to the frequency ratio between the peak of the axial force spectral density and damped natural frequency of the listed mode. y_0 denotes the generalized response, whereas S_z denotes the bending stress about the strong axis. The asterisk-denoted response values are corresponding to results including uncertainty, characterized by an increase of σ_N of 20% and decrease of quadratic damping (c_{quad}) of 20%. The harmonic amplitude N is established based on an exceedance probability of 10^{-3}.

Mode	ω_d +/- 20% [rad/s]	Segment	β	A_{cr} [MN]	$\sigma_N/0.4$ [MN]	Onset	N [MN]	y_0 (y_0^*)	S_z (S_z^*) [MPa]
3	0.1998–0.2997	1	1.89	6.78	7.25	fails	10.78	0.19 (0.37)	5.76 (11.09)
4	0.2300–0.3450	1	1.64	6.31	7.25	fails	10.78	0.85 (1.58)	30.31 (56.17)

6.5.1.2 10000-year

The 10000-year swell condition applied to K14 in the global analysis model yields the axial force spectral density depicted in Figure 6-34. The frequency range corresponding to 95% drop from the peak value is also indicated in the figure. More details about the specific values corresponding to the segment are given in Table 6-30.

The analysis of parametric excitation due to 10000-year swell on K14 is summarized in Table 6-31. As for the 100-year swell condition, modes 3 and 4 are located within the specified range corresponding to $\beta = 2.0$ for the 10000-year swell condition. The onset criterion is exceeded for both modes, and the modes might be parametrically excited. The estimated terminal response levels are significantly lower than the results obtained for the 100-year swell condition: the largest estimated bending stress is estimated to 3.88 MPa. The response levels estimated accounting based on a 20% reduction of quadratic damping and a 20% increase of the applied axial force amplitude are relatively very large, but represent acceptable absolute levels.

Figure 6-34. Spectral density of axial force variation on K14 due to 10000-year swell. The segment lines indicate what frequency ranges to consider for evaluation of parametric resonance.

Table 6-30. Segments defined from spectral density of axial force variation on K14 due to 10000-year swell.

| Segment | σ_N [MN] | Harmonic, N [MN] | ω_p [rad/s] | Trigger ranges [rad/s] | | |
				$\beta = 0.5$	$\beta = 1.0$	$\beta = 2.0$
1	3.2	6.8863	0.4633	0.8682–1.1330	0.4341–0.5665	0.2170–0.2832

Table 6-31. Harmonic results for $\beta = 2.0$, for 10000-year swell on K14. The listed β-value corresponds to the frequency ratio between the peak of the axial force spectral density and damped natural frequency of the listed mode. y_0 denotes the generalized response, whereas S_z denotes the bending stress about the strong axis. The asterisk-denoted response values are corresponding to results including uncertainty, characterized by an increase of σ_N of 20% and decrease of quadratic damping (c_{quad}) of 20%. The harmonic amplitude N is established based on an exceedance probability of 10^{-1}.

Mode	ω_d +/- 20% [rad/s]	Segment	β	A_{cr} [MN]	$\sigma_N/0.4$ [MN]	Onset	N [MN]	y_0 (y_0^*)	S_z (S_z^*) [MPa]
3	0.1998–0.2997	1	1.85	6.78	8.02	fails	6.89	0 (0.09)	0.15 (2.67)
4	0.2300–0.3450	1	1.61	6.31	8.02	fails	6.89	0.11 (0.46)	3.88 (16.52)

To assess the validity of the observed results, a Monte Carlo simulation of mode 4 of K14 was conducted with axial force variation characterized by the spectral density from the selected 10000-year swell condition. Prior to Monte Carlo simulation, the spectral density was adjusted to have a frequency ratio to mode 4 of exactly 2.0, as indicated in Figure 6-35. The external flat-spectrum force power spectral density, characterizing the external white-noise excitation applied, is also indicated in the figure. The difference between the maximum generalized response with and without parameter variation from all simulations are shown in Figure 6-36 as a Gumbel probability paper. The linearity of the sample points in the probability paper is not very good, but is still considered reasonable due to the low response values. The estimated terminal level, due to a Rayleigh distribution with exceedance probability of 30.4%, corresponding to an exceedance probability of 10% of a 1hr simulation (scaled to ensure 500 cycles of mode), is shown in the same figure. Because the applied axial force is very close to the critical amplitude, the resulting terminal level estimate is zero for the given probability. The results from the Monte Carlo simulation support the fact that a very small response due to parametric resonance is observed; the 3040th largest response (from 10000 realizations) due to parametric resonance is below 0.01m (under 0.5MPa). The corresponding time series is shown in Figure 6-37. Thus, the Monte Carlo simulation support the conclusion from the terminal level estimate: parametric excitation due to 10000-year swell conditions on K14 may occur, but the likely effects on the response are acceptable.
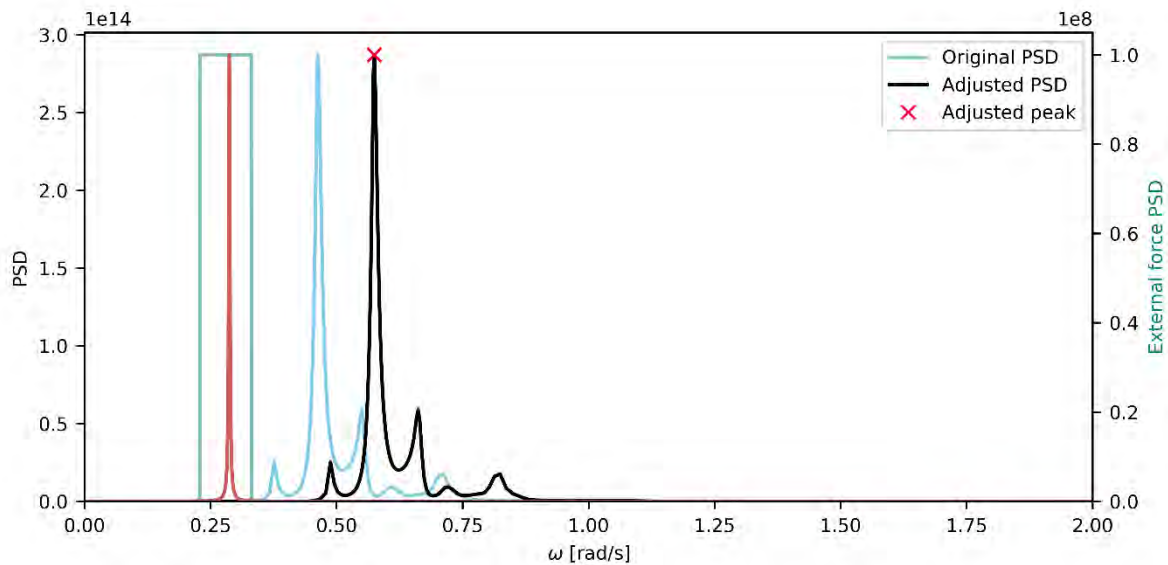

Figure 6-35. Power spectral densities of axial force variation due to a 10000-year swell condition and the evenly distributed lateral external force, adjusted to trigger parametric resonance in mode 4 of K14. The red curve indicates the shape and frequency position of the frequency response function of the mode under investigation.

Concept development, floating bridge E39 Bjørnafjorden

Appendix S – Parametric excitation – K12
6 Concept assessments: critical amplitudes and
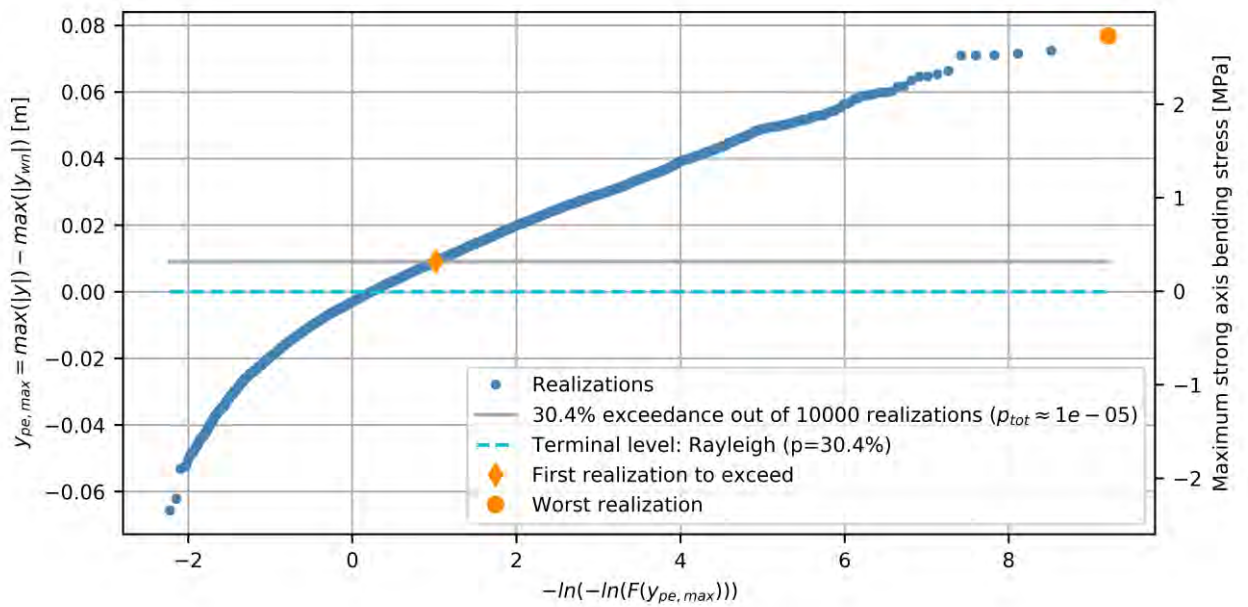terminal level estimates

Figure 6-36. Gumbel probability paper of maximum response of mode 4 of K14 due to parametric excitation, due to simulated axial force spectral density given in Figure 6-35, which is resulting from a 10000-year swell condition. The maximum response from the realization with approximate exceedance probability $p = 30.4\%$ corresponds to the 30th largest realization (out of 10000 realizations in total).
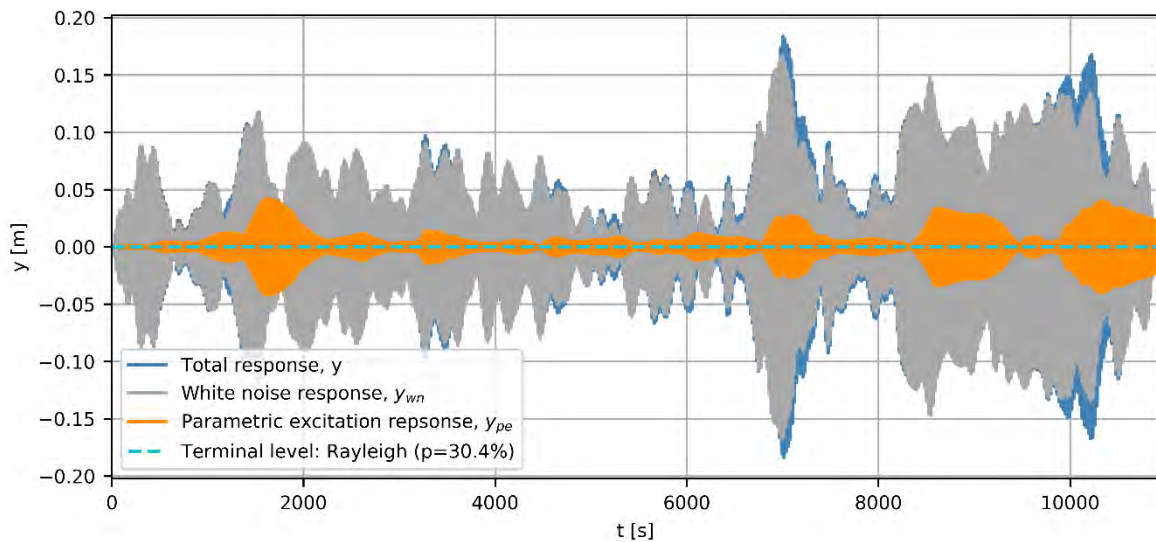
Figure 6-37. The 3040th largest response out of 10000 realizations, or the response corresponding to exceedance probability $p = 30.4\%$, corresponding to (♦) in Figure 6-36.

6.5.2   Wind sea

6.5.2.1   100-year

The spectral density of the axial force variation on K14 from 100-year wind sea is shown in Figure 6-38. The spectral density is assigned a frequency range based on a 90% drop from the peak value. More details about the segment are given in Table 6-32. The results from the harmonic analysis of parametric excitation of K14 exposed to 100-year wind sea excitation, with frequency ratio $\beta = 2$, are summarized in Table 6-33. As seen in the table, the onset criterion is not exceeded for any modes.
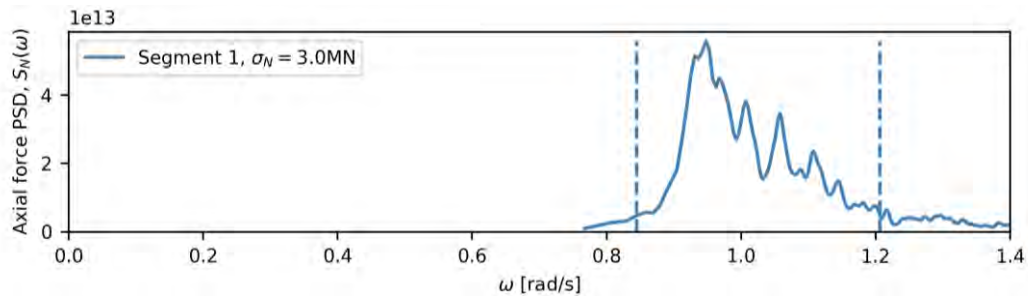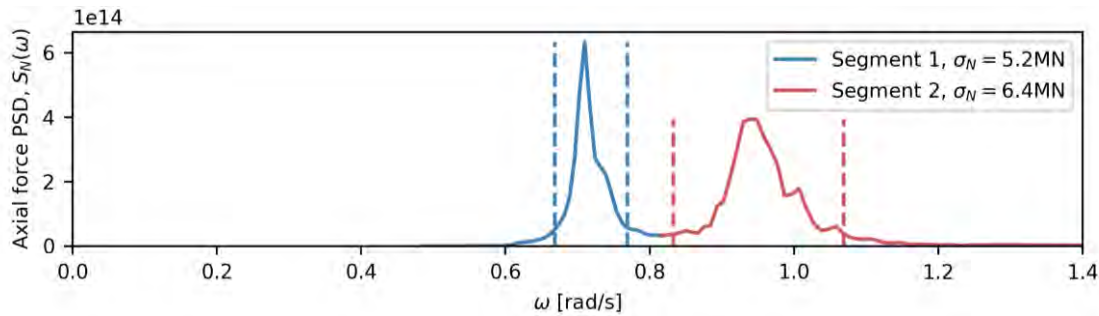

Figure 6-38. Spectral density of axial force variation on K14 due to 100-year wind sea. The segment lines indicate what frequency ranges to consider for evaluation of parametric excitation.

Table 6-32. Segments defined from spectral density of axial force variation on K14 due to 100-year wind sea.

Segment	σ_N [MN]	Harmonic, N [MN]	ω_p [rad/s]	Trigger ranges [rad/s] $\beta = 0.5$	$\beta = 1.0$	$\beta = 2.0$
1	3.0	11.3	0.9476	1.6896–2.4128	0.8448–1.2064	0.4224–0.6032

Table 6-33. Harmonic results for $\beta = 2.0$, for 100-year wind sea on K14. The listed β-value corresponds to the frequency ratio between the peak of the axial force spectral density and damped natural frequency of the listed mode. y_0 denotes the generalized response, whereas S_z denotes the bending stress about the strong axis. The asterisk-denoted response values are corresponding to results including uncertainty, characterized by an increase of σ_N of 20% and decrease of quadratic damping (c_{quad}) of 20%. The harmonic amplitude N is established based on an exceedance probability of 10^{-3}.

Mode	ω_d +/- 20% [rad/s]	Segment	β	A_{cr} [MN]	$\sigma_N/0.4$ [MN]	Onset	N [MN]	y_0 (y_0^*)	S_z (S_z^*) [MPa]
5	0.3074–0.4611	1	2.47	18.95	7.61	ok	11.31	0	0
6	0.3789–0.5683	1	2.00	30.65	7.61	ok	11.31	0	0
7	0.4480–0.6720	1	1.69	106.80	7.61	ok	11.31	0	0
8	0.4953–0.7429	1	1.53	71.61	7.61	ok	11.31	0	0
9	0.5654–0.8481	1	1.34	128.77	7.61	ok	11.31	0	0
10	0.5997–0.8996	1	1.26	103.07	7.61	ok	11.31	0	0

6.5.2.2 10000-year

The excitation corresponding to 10000-year wind sea conditions applied to the global analysis model, yielded an axial force variation spectral density as shown in Figure 6-39. The spectral density was divided into two segments and given frequency ranges corresponding to a 90% drop from the peaks within each segment, as indicated in the figure. More details about the segments of the spectral density are given in Table 6-34. The results from the harmonic analysis of parametric excitation of K14 exposed to 10000-year wind sea excitation, with frequency ratio $\beta = 2$, are summarized in Table 6-34. As for the 100-year wind sea condition, the onset criterion is not exceeded for any modes.

Figure 6-39. Spectral density of axial force variation on K14 due to 10000-year wind sea. The segment lines indicate what frequency ranges to consider for evaluation of parametric resonance.

Table 6-34. Segments defined from spectral density of axial force variation on K14 due to 10000-year wind sea.

| Segment | σ_N [MN] | Harmonic, N [MN] | ω_p [rad/s] | Trigger ranges [rad/s] | | |
				$\beta = 0.5$	$\beta = 1.0$	$\beta = 2.0$
1	5.2	11.1	0.7099	1.3373–1.5379	0.6686–0.7690	0.3343–0.3845
2	6.4	13.8	0.9389	1.6658–2.1382	0.8329–1.0691	0.4165–0.5345

Table 6-35. Harmonic results for $\beta = 2.0$, for 10000-year wind sea on K14. The listed β-value corresponds to the frequency ratio between the peak of the axial force spectral density and damped natural frequency of the listed mode. y_0 denotes the generalized response, whereas S_z denotes the bending stress about the strong axis. The asterisk-denoted response values are corresponding to results including uncertainty, characterized by an increase of σ_N of 20% and decrease of quadratic damping (c_{quad}) of 20%. The harmonic amplitude N is established based on an exceedance probability of 10^{-1}.

Mode	ω_d +/- 20% [rad/s]	Segment	β	A_{cr} [MN]	$\sigma_N/0.4$ [MN]	Onset	N [MN]	y_0 (y_0^*)	S_z (S_z^*) [MPa]
4	0.2300–0.3450	1	2.47	18.22	12.91	ok	11.08	0	0
5	0.3074–0.4611	2	2.44	20.96	16.03	ok	13.76	0	0
6	0.3789–0.5683	2	1.98	32.75	16.03	ok	13.76	0	0
7	0.4480–0.6720	2	1.68	112.64	16.03	ok	13.76	0	0
8	0.4953–0.7429	2	1.52	73.64	16.03	ok	13.76	0	0

Concept development, floating bridge E39 Bjørnafjorden

Appendix S – Parametric excitation – K12
6 Concept assessments: critical amplitudes and
terminal level estimates

To assess the validity of the observed results, a Monte Carlo simulation of mode 4 of K14 was conducted with axial force variation characterized by the spectral density from the selected 10000-year wind sea condition. Prior to Monte Carlo simulation, the peak of the spectral density is shifted in frequency such that it has a ratio to the natural frequency of mode 4 of exactly 2.0, as indicated in Figure 6-40. The external flat-spectrum force power spectral density is also indicated in the figure. The results conducted with the full damping present, i.e., including the aerodynamic contributions, supports the results in the harmonic analysis summarized in Table 6-35: no parametric excitation is observed. Monte Carlo simulation was therefore conducted on the system excluding the aerodynamic damping, which clearly would produce highly conservative results. The difference between the resulting maximum generalized response with and without parameter variation are shown from all simulations as a Gumbel probability paper in Figure 6-41. The estimated terminal level, due to a Rayleigh distribution with exceedance probability of 30.4% (scaled to a duration corresponding to 500 cycles) is shown in the same figure. The linearity of the sample points in the probability paper is considered reasonably good. This time series is depicted in Figure 6-42. The realization with sample probability equal to the set exceedance probability is showing a far lower response than the terminal response estimate. This is as expected due to the broad-bandedness of the axial force variation. As this example illustrates, the response resulting from parametric excitation of K14 due to wind sea excitation under the assumption of no aerodynamic damping is considered unproblematic.
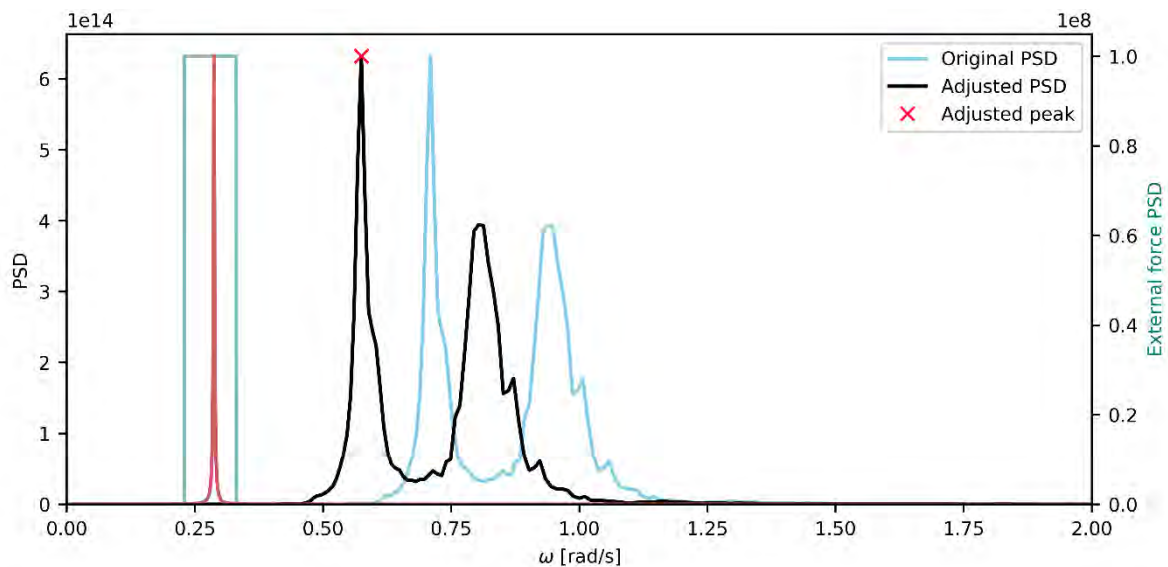
Figure 6-40. Power spectral densities of axial force variation due to a 10000-year wind sea condition and the evenly distributed lateral external force, adjusted to trigger parametric resonance in mode 4 of K14. The red curve indicates the shape and frequency position of the frequency response function of the mode under investigation.
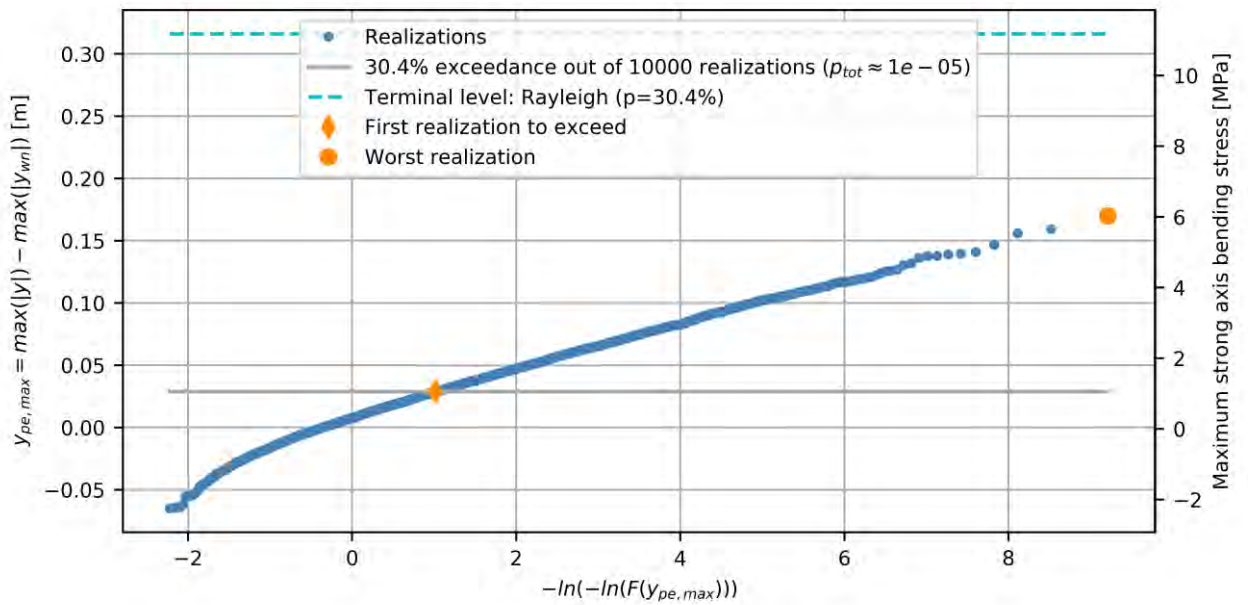
Figure 6-41. Gumbel probability paper of maximum response due to parametric resonance, due to simulated axial force spectral density given in Figure 6-40, which is resulting from a 10000-year wind sea condition. The maximum response from the realization with approximate exceedance probability $p = 30.4\%$ corresponds to the 3040th largest realization (out of 10000 realizations in total).
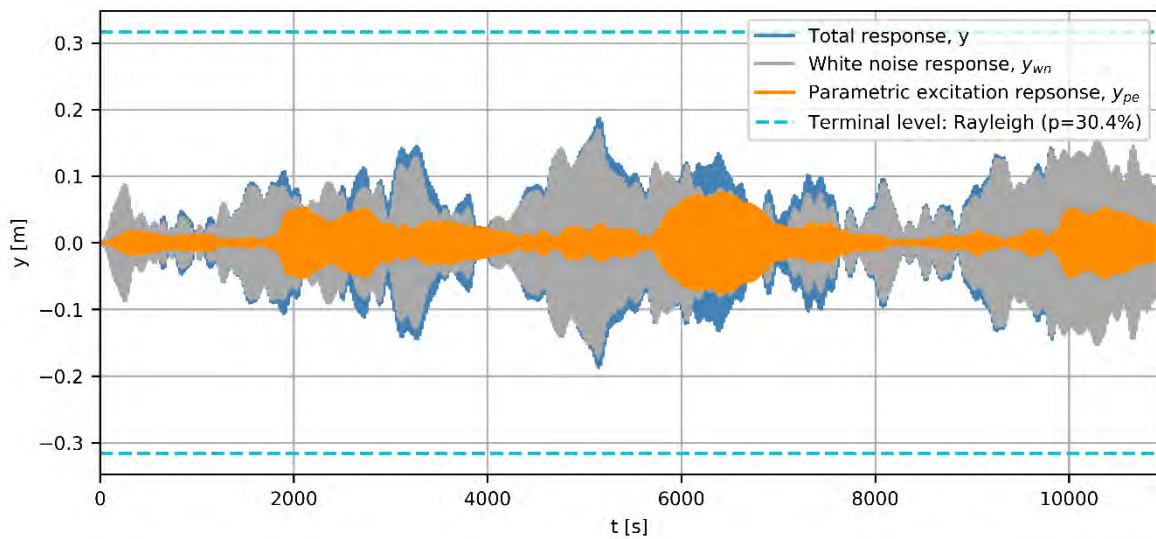

Figure 6-42. The 3040th largest response out of 10000 realizations, or the response corresponding to exceedance probability $p = 30.4\%$, corresponding to (♦) in Figure 6-41.

6.5.3 Wind

Figure 6-43 depicts the frequency ratios between all the combinations of the first ten modes of K14. The frequency ratios close to 0.5, 1.0 or 2.0 are highlighted; an uncertainty of 10% is considered for both natural frequencies in each combination. The two following sub-sections provide details regarding the analysis of parametric excitation due to 100-year and 10000-year wind conditions.

	1	2	3	4	5	6	7	8	9	10
1	1.0	0.8	0.6	0.5	0.4	0.3	0.3	0.2	0.2	0.2
2	1.2	1.0	0.7	0.6	0.5	0.4	0.3	0.3	0.3	0.2
3	1.6	1.4	1.0	0.9	0.6	0.5	0.4	0.4	0.4	0.3
4	1.9	1.6	1.2	1.0	0.7	0.6	0.5	0.5	0.4	0.4
5	2.5	2.1	1.5	1.3	1.0	0.8	0.7	0.6	0.5	0.5
6	3.1	2.6	1.9	1.6	1.2	1.0	0.8	0.8	0.7	0.6
7	3.7	3.1	2.2	1.9	1.5	1.2	1.0	0.9	0.8	0.7
8	4.1	3.5	2.5	2.2	1.6	1.3	1.1	1.0	0.9	0.8
9	4.7	3.9	2.8	2.5	1.8	1.5	1.3	1.1	1.0	0.9
10	4.9	4.2	3.0	2.6	2.0	1.6	1.3	1.2	1.1	1.0

β_{ij}: K14_06
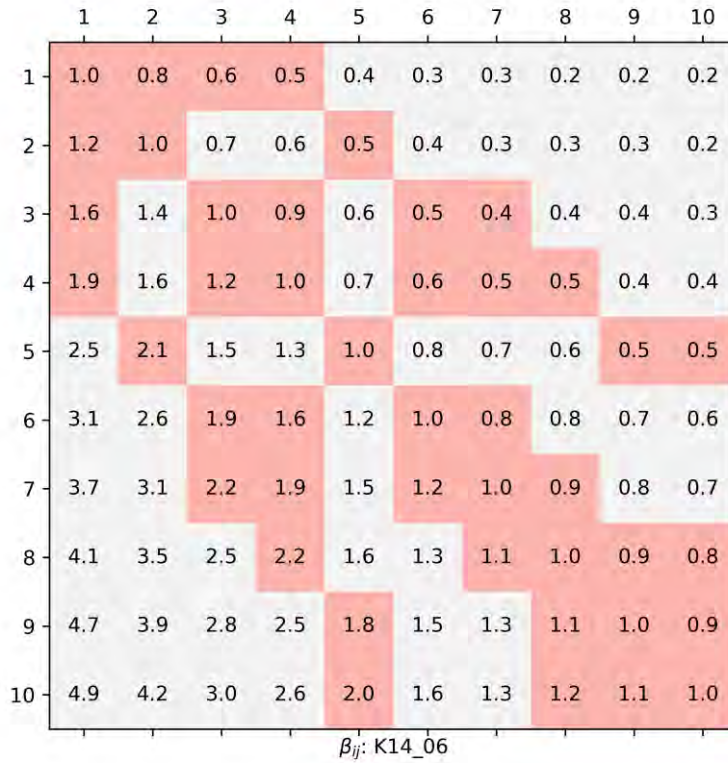
Figure 6-43. Frequency ratios between natural frequencies of K14_06.

6.5.3.1 100-year

The harshest axial force response on K14 due to 100-year wind is observed for the westerly winds in Table 5-5 (except for mode 7). These standard deviations and the corresponding contribution to the critical damping coefficient from aerodynamic damping are listed in Table 6-36. The onset criterion was assessed based on the given data, producing results as indicated in Enclosure 2, and some of the most important results are given in Table 6-37. The results indicate no parametric excitation on K14 due to the axial force spectral density resulting from the 100-year wind condition.

Table 6-36: Utilized (westerly wind) modal aerodynamic damping as a fraction of critical damping and the modal standard deviation for the 100-year wind conditions for the K14 concept.

	Aerodynamic critical damping ratio, ξ_{aero}	Standard deviation of axial force, σ_N [MN]
Mode 1	0.0142	-
Mode 2	0.0140	-
Mode 3	0.0117	-
Mode 4	0.0091	-
Mode 5	0.0062	0.49
Mode 6	0.0045	0.67
Mode 7	0.0029	0.57
Mode 8	0.0033	-
Mode 9	0.0028	0.66
Mode 10	0.0025	-
Mode 11	0.0017	-
Mode 12	0.0015	

Table 6-37. Selected harmonic results for $\beta = 0.5, 1.0, 2.0$, for 100-year wind on K14.

Mode pair					
Axial force	Response	β	ξ including aero. [%]	A_{cr} [MN]	$\sigma_N/0.4$ [MN]	Onset
5	2	2.14	1.87	21.19	1.23	ok
6	3	1.90	1.65	23.35	1.68	ok
6	4	1.65	1.40	17.96	1.68	ok
7	4	1.95	1.40	17.96	1.43	ok
5	5	1.00	1.24	131.15	1.23	ok

6.5.3.2   10000-year

The harshest axial force response on K14 due to 10000-year wind is observed for the westerly winds in Table 5-6. These standard deviations and the corresponding contribution to the critical damping coefficient from aerodynamic damping are listed in Table 6-38. The onset criterion was assessed based on the given data, producing results as indicated in Enclosure 2, and some of the most important results are given in Table 6-39. As for the 100-year condition, the results indicate that K14 is not susceptible to parametric excitation due to axial force variation generated by a 10000-year wind condition.

Table 6-38: Utilized (westerly wind) modal aerodynamic damping as a fraction of critical damping and the modal standard deviation for the 10000-year wind conditions for the K14 concept.

	Aerodynamic critical damping ratio, ξ_{aero}	Standard deviation of axial force, σ_N [MN]
Mode 1	0.0179	-
Mode 2	0.0171	-
Mode 3	0.0142	-
Mode 4	0.0111	-
Mode 5	0.0075	1.22
Mode 6	0.0054	1.69
Mode 7	0.0035	
Mode 8	0.0041	-
Mode 9	0.0034	1.63
Mode 10	0.0029	-
Mode 11	0.0011	-
Mode 12	0.0012	

Table 6-39. Selected harmonic results for $\beta = 0.5, 1.0, 2.0$, for 10000-year wind on K14.

Mode pair						
Axial force	Response	β	ξ including aero. [%]	A_{cr} [MN]	$\sigma_N/0.4$ [MN]	Onset
5	2	2.14	2.18	24.71	3.05	ok
6	3	1.90	1.90	26.89	4.22	ok
6	4	1.65	1.60	20.52	4.22	ok
5	5	1.00	1.37	137.88	3.05	ok

6.6 A comment on the applied aerodynamic damping

For the wind sea analyses, aerodynamic damping is included. This damping contribution is dependent on the wind direction and mean wind velocity, as indicated in Figure 6-44, exemplifying the effect for K11. The aerodynamic damping values used to establish the full modal damping for wind sea cases are based on the values provided in Section 5, i.e., for wind direction fully lateral to the bridge.

According to the design basis, an offset of 15° between mean wave angle and wind angle have to be accounted for. From the figure, a reduction of around 30% could be inferred for cases where the wind is approaching with an offset of 30° from a perpendicular angle to the bridge (15° offset to the wind sea direction). This is currently not included in the analyses provided above, such that the aerodynamic damping levels does not represent the worst-case combination of conditions. Based on the findings regarding the broadbandedness and the resulting acceptable response levels observed from Monte Carlo simulations of response due to parametric excitation from wind sea, which disregards the aerodynamic damping altogether, the conclusions are likely not altered by this. Furthermore, it is not important for the ranking of the concepts. A more refined treatment of the aerodynamic damping due to skew winds should be conducted at a later point in time, for the chosen concept.
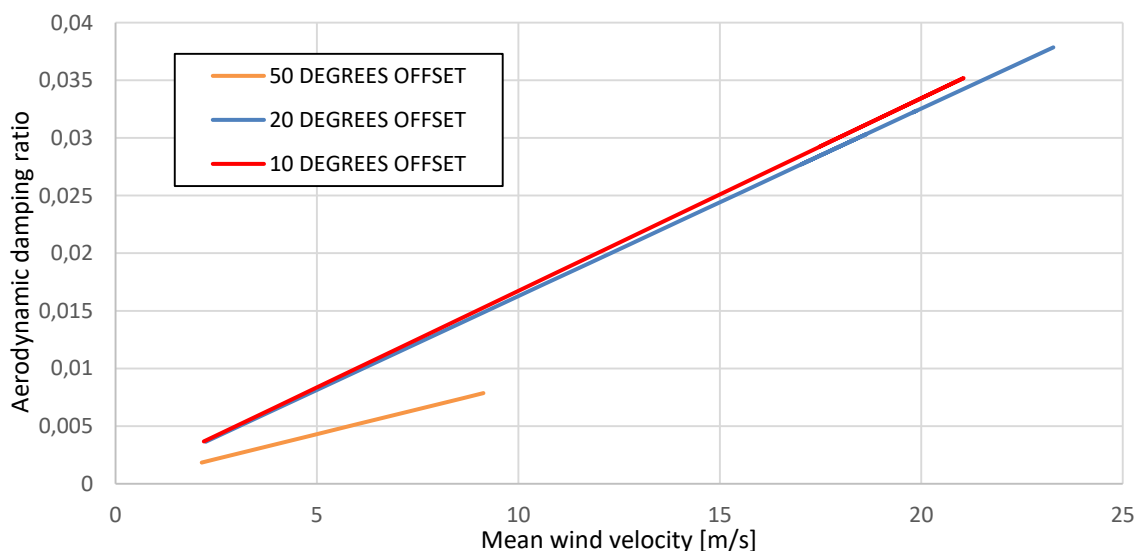
Figure 6-44. Effect on aerodynamic damping of directional offset from a lateral angle and mean wind velocity.

6.7 Summarizing comments

The susceptibilities and likely effects of parametric resonance on all concepts are assessed, mode by mode. A good performance is found for K12 and K14, which are both satisfying the onset criterion for wind sea and wind. A small exceedance of the onset criterion is observed due to swell excitation, but the quadratic damping ensures that the resulting response is very small and clearly acceptable. The analysis of K11, however, is not yielding satisfactory results, and the simplified analysis indicates a potentially large response due to parametric resonance from the swell excitation. Due to the aerodynamic damping also present for wind sea and wind, parametric resonance is not likely to occur due to these environmental actions.

Slightly different results could be expected by adjusting the frequency of the applied excitation used to estimate the axial force spectral densities. However, the overlying conclusions will likely remain the same from the perspective of the simplified analysis conducted herein: K12 and K14 seem reasonably robust with respect to parametric resonance; whereas K11 seems to be highly susceptible to parametric resonance from swell, with an unacceptable response as consequence.

7   Sensitivity studies

Sensitivity studies on certain key parameters are conducted, to assess the effect the parameters have on the excitation or estimated response.

7.1   Damping uncertainty

The total damping is comprised of linear damping sources: potential damping from hydrodynamic self-excited forces on pontoons, structural damping, and aerodynamic damping; and non-linear damping sources, which are only encompassing the quadratic drag damping herein.

The constant modal structural damping $\xi = 0.5\%$ is applied as structural damping, as specified in the design basis [9] and NS-EN 1991-1-4. As this is considered a conservative estimate, the uncertainty of this is on the upper side of the given value. The uncertainty of the contribution from potential damping is most likely caused by an uncertainty in the natural frequencies and mode shape of the full system, because the curve of the potential damping itself is well-established and relative certain. An error in natural frequencies, however, could result in a large error in the damping contribution from potential damping, as indicated in Figure 7-1. For the frequency ranges studied herein, the contribution from potential damping is very small, and this is therefore not an important consideration in this context. The aerodynamic damping contribution is more uncertain, as it is based on either quasi-static assumptions or experimental data from wind tunnel tests, which introduces uncertainty in measurement and analysis.

The quadratic drag damping originating from the pontoons is considered uncertain. Computational fluid dynamics (CFD) simulations have been conducted to provide a better estimate of the drag factor C_d (see Appendix H). Mooring lines from anchoring systems provide the dominating contribution to quadratic drag damping for the anchored concepts. The uncertainty of this damping is much lower because the drag damping of slender bodies (lines) are not dominated by end effects, such that standard results are applicable. However, as indicated in Section 5.6, changing static configuration of the mooring lines could significantly reduce the quadratic damping.

The uncertainty in the sources of damping is not considered directly herein. A study of the effect of the total linear damping and total quadratic damping on the terminal response, however, is given below. The partial derivatives of the modal terminal response with respect to the quadratic damping c_{quad} and the linear critical damping coefficient ξ are given as follows:

$$\frac{\partial y_0}{\partial c_{quad}} = -3\pi \frac{N\hat{k}_g - 2c_{lin}\omega_n}{16\omega_n^2 c_{quad}^2}, \quad \frac{\partial y_0}{\partial \xi} = -\frac{\sqrt{km}}{4c_{quad}} 3\pi$$

The modal parameters representing mode 4 of K11 are used as a representative example, and plots of the resulting terminal response for varying linear and quadratic damping in Figure 7-2 and Figure 7-3, respectively. Both from the equation above and from studying Figure 7-3, it is clear that uncertainty in the quadratic damping estimate has a drastic effect on the terminal level for low quadratic damping. As an example, modes 4 and 5 on K11 (exposed modes) has estimated quadratic drag damping coefficients of $118 \, kN/\left(\frac{m}{s}\right)^2$ and $189 \, kN/\left(\frac{m}{s}\right)^2$. In contrast, the same factor of modes 3 and 5 on K12 (exposed modes) are estimated to $1543 \, kN/\left(\frac{m}{s}\right)^2$ and $302 \, kN/\left(\frac{m}{s}\right)^2$, respectively; whereas modes 3, 4 and 5 on K14 (exposed modes) are estimated to $1869 \, kN/\left(\frac{m}{s}\right)^2$, $425 \, kN/\left(\frac{m}{s}\right)^2$, and $1260 \, kN/\left(\frac{m}{s}\right)^2$, respectively. Inaccuracies in the estimates of the quadratic drag damping thus has a much larger effect on K11 than on K12 and K14.
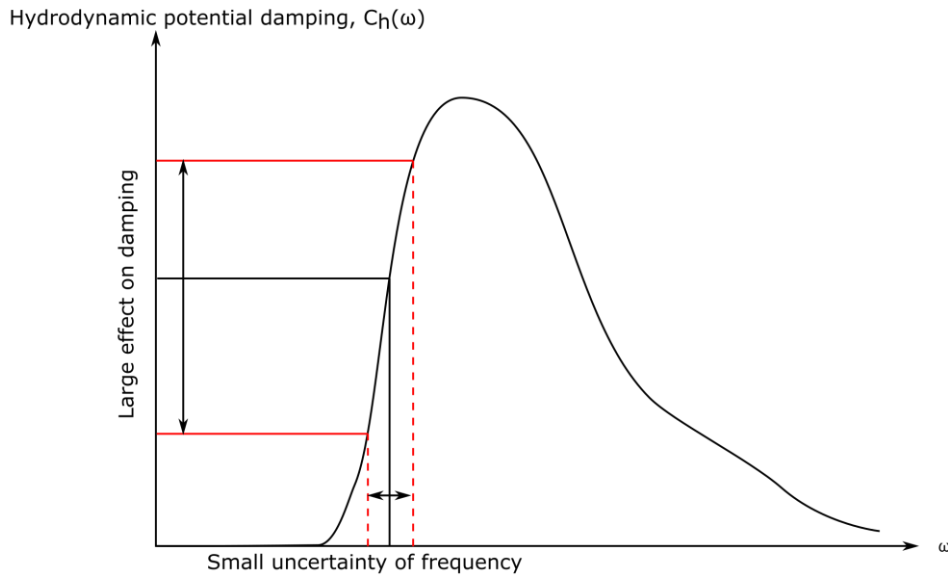
Figure 7-1. Uncertainty in frequency might lead to an effective uncertainty in modal damping due to the frequency dependency of the damping contribution.
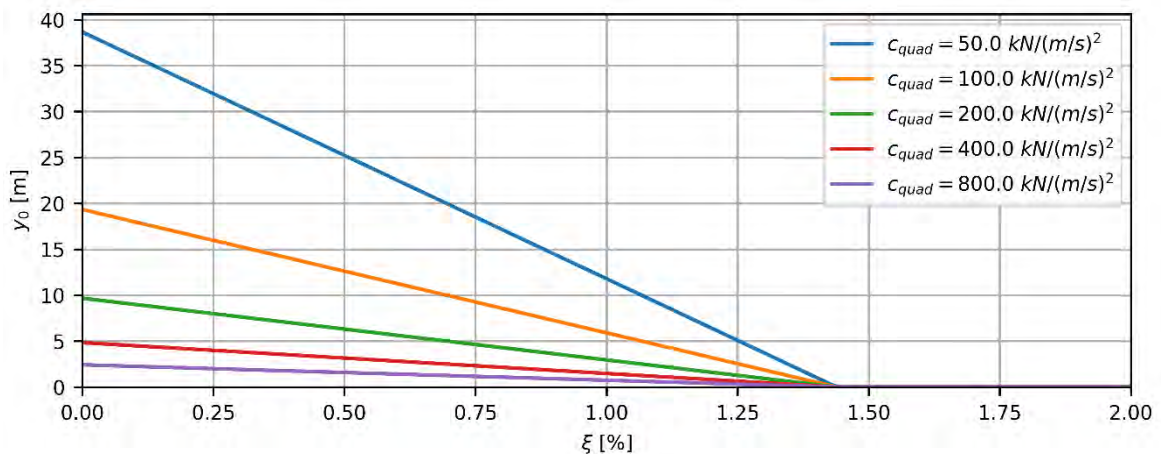

Figure 7-2. Effect of (linear) critical damping ratio on the terminal level for mode 4 on K11, exposed to axial force variation with circular frequency $2\omega_d$.
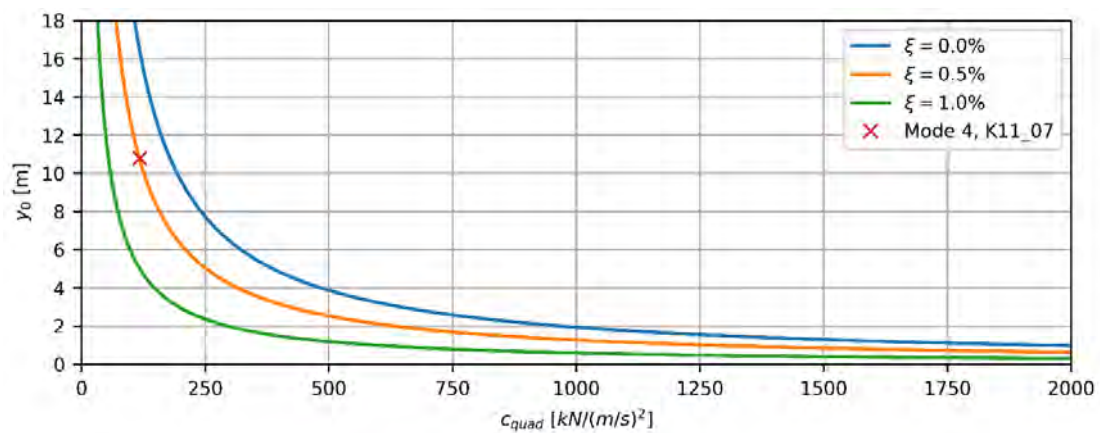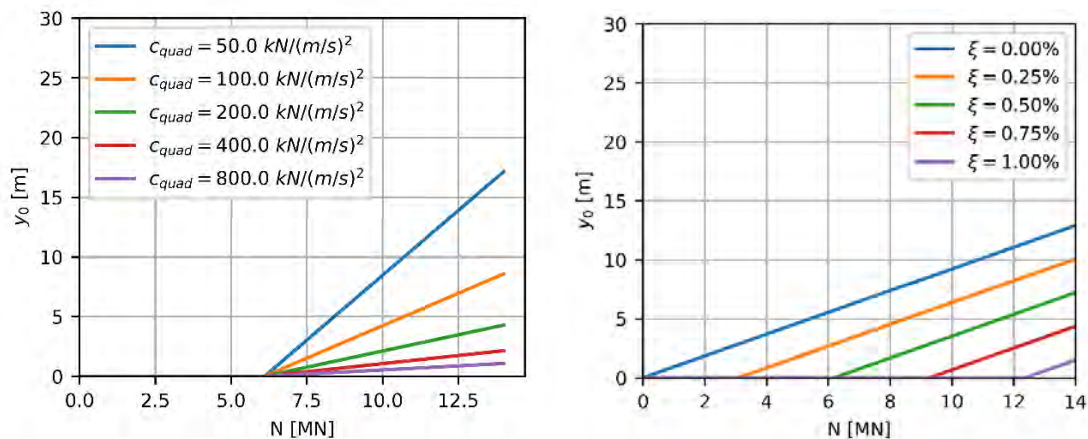

Figure 7-3. Effect of quadratic damping on the terminal level for mode 4 on K11, exposed to axial force variation with circular frequency $2\omega_d$.

Potential errors in the linear critical damping coefficient is affecting the resulting terminal response linearly. It is important to note that for low quadratic damping, the slopes are steeper; the effect on terminal response from the uncertainty of the linear damping is increased when the quadratic drag damping is low. Uncertainties in the natural frequency has the same functional effect, but the natural frequency predictions are considered more certain than the quadratic drag predictions.

7.2   Applied axial force

The partial derivatives of the modal terminal response with respect to the harmonic axial force amplitude can be expressed as follows:

$$\frac{\partial y_0}{\partial N} = \frac{3\pi}{16 c_{quad} \omega_n^2} \hat{k}_g$$

The effect of uncertainty in the applied harmonic axial force is depicted in Figure 7-4. As expected, the terminal response increases linearly, from the point where $N = A_{cr} \Rightarrow y_0 = 0$, as the applied axial force increases. The linear slope is larger for lower quadratic damping, such that, again, the consequence of treating the applied axial force imprecise is amplified for lower quadratic damping ranges. Larger normalized geometric stiffness increases the slope.

The applied axial force is also highly dependent on the specified frequency of the swell excitation, compared to the modes of the system. The reason for this is that the swell spectral density is narrow-banded and the transfer function between wave excitation and axial force response is narrow-banded; the multiplication of two narrow-banded functions will become very sensitive to the frequency difference between the two peaks. In particular, mode 6 of all three concepts considered have a very large axial force contribution, such that the axial force due to swell excitation near the frequency of this mode will be very sensitive to changes in frequency. If the specified range for swell in the design basis is slightly inaccurate, it might therefore cause large inaccuracies in the estimated axial force spectral density.

Figure 7-4. Effect of harmonic axial force amplitude on the terminal level for mode 4 on K11, exposed to axial force variation with circular frequency $2\omega_d$. The left figure shows the relationship for different quadratic drag damping coefficients, whereas the right figure shows the relationship for different linear critical damping ratios.

7.3 Geometric stiffness

The partial derivatives of the modal terminal response with respect to the normalized geometric stiffness can be expressed as follows:

$$\frac{\partial y_0}{\partial \hat{k}_g} = \frac{3\pi}{16 c_{quad} \omega_n^2} N$$

Figure 7-5 depicts the terminal response for varying values of geometric stiffness. Larger applied axial force increases the slope.
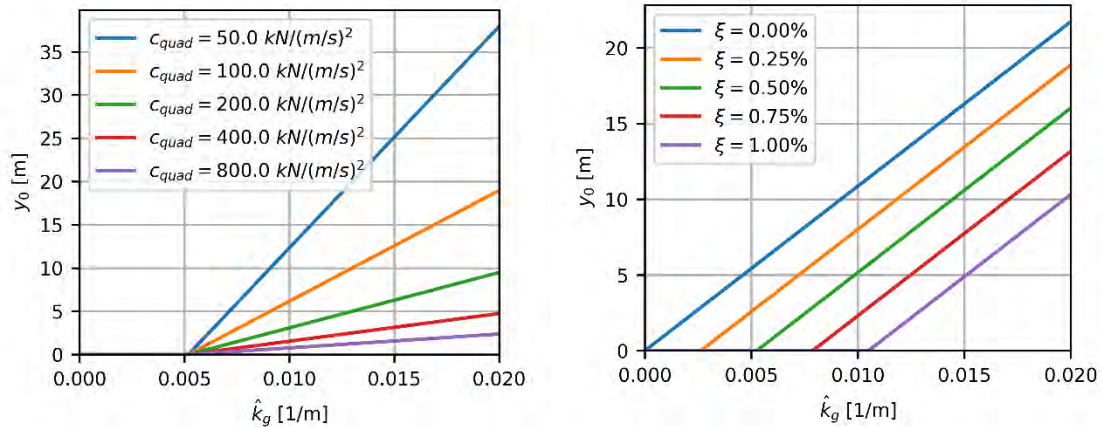
Figure 7-5. Effect of geometric stiffness (normalized to maximum axial force amplitude) on the terminal level for mode 4 on K11, exposed to axial force variation with circular frequency $2\omega_d$. The left figure shows the relationship for different quadratic drag damping coefficients, whereas the right figure shows the relationship for different linear critical damping ratios.

8 Global response analyses

8.1 Introduction

Global analyses of the numerical OrcaFlex models have been simulated for K11, K12 and K14, subjected to loads that trigger parametric resonance. The numerical analysis should in principle be able to capture the geometric variations that causes parametric resonance. A model description of the OrcaFlex model is presented in Appendix F.

8.1.1 Regular wave analysis

Regular wave analyses have been simulated in OrcaFlex for the K11, K12 and K14 model, to assess the global response in representative regular waves. The wave period was applied at the wave period in the swell frequency range which gives the highest axial force response (12.75s for K11, 13s for K12 and 13.25s for K14). Three wave heights have been considered: 0.9m (roughly two times the 10 000-year H_s), 1.8m and 2.7m. The bridge girder stiffness was modified to account for the 10% uncertainty in the eigenfrequencies as recommended in the procedure outlined by the client [2]. This has been done by a 20% decrease of strong axis stiffness for K11 and K12, and a 200% axial stiffness increase of K14, and ensures that mode 4 coincides with half the regular wave frequency.

The regular wave analyses indicate that without the mooring line damping, all concept may be prone to parametric resonance for a regular wave representation of the swell sea state. However, when including the nonlinear mooring damping, the axial force is significantly reduced, and parametric resonance is not observed. Sensitivity studies with higher pontoon drag coefficients have been performed for the K11 model, where it is observed that the response is reduced because of the quadratic damping. However, as presented in Section 9, this increase of pontoon drag coefficient may result in static buckling.

The global analysis results for K11 have been compared with a representation of a linear response, where a 1/10 of the wave height have been simulated and the response have been scaled by a factor 10 post-analysis. The linear representation has a significantly lower response and indicate that OrcaFlex may capture parametric excitation.

When parametric resonance seems to be triggered, a shift is observed in the axial force and result in a substantially lower level of axial force response after the onset of parametric resonance. This shift of axial response is not accounted for in the SDOF results, where frequency domain results (linear analysis) are used as input.

8.1.2 Stochastic analysis

Stochastic analysis of the K11 has also been performed, to give a better understanding of the parametric resonance phenomenon and to validate the effect observed with a background white noise simulation, where the results are presented in Section 4.3.

8.2 Regular wave analysis of K11

8.2.1 Sensitivity of pontoon drag coefficients

Regular wave analyses were performed with $H = 0.9m$, $H = 1.8m$, $H = 2.7m$. The drag coefficient was varied between $C_d = 0$, $C_d = 0.4$ and $C_d = 1.0$. The time histories of the maximum response values of axial forces, strong axis bending moment and transverse displacement are shown in Figure 8-1, Figure 8-2 and Figure 8-3, for three selected combinations of wave height and drag coefficient. Parametric resonance was observed for all wave heights for $C_d = 0$ or 0.4, and wave heights of 1.8m

and 2.9m for $C_d = 1.0$. As can be observed in the time series plot, the bridge girder axial force response is reduced when the parametric resonance occurs. The mechanisms behind this behaviour are unknown, and this could be further studied in the future by simulating the response with a two-degree-of-freedom model with the same damping levels and frequency ratios. Envelope values of axial forces and transverse displacement from the different combinations of wave height and drag coefficie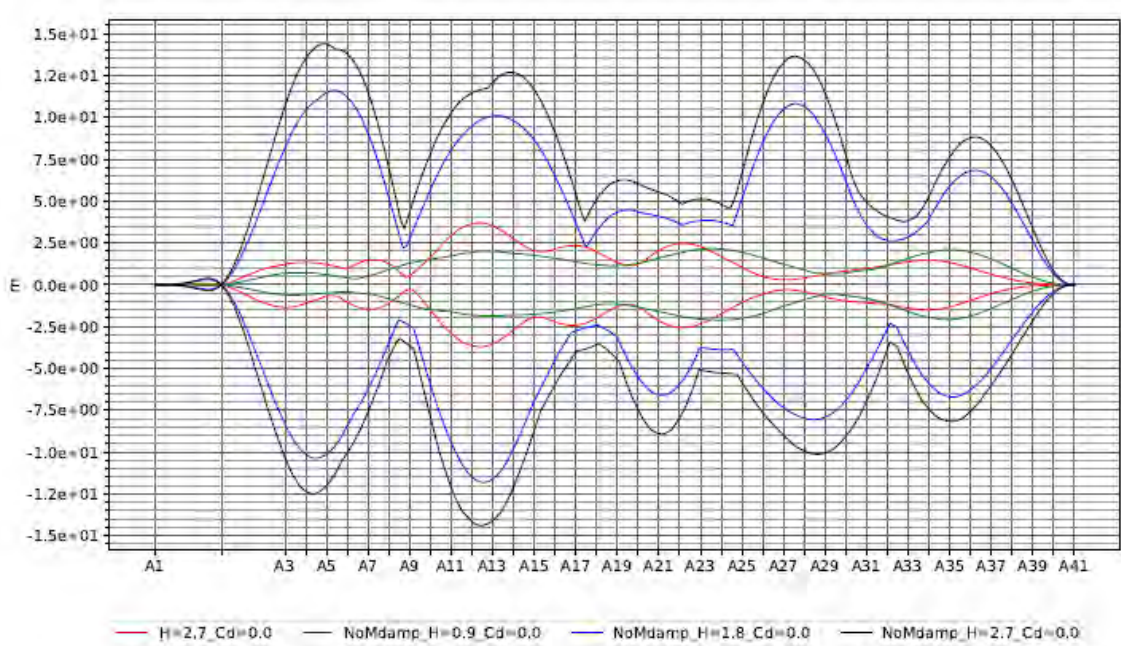nt are shown in Figure 8-4 and Figure 8-5, respectively. They support the comments made based on the time history plots.
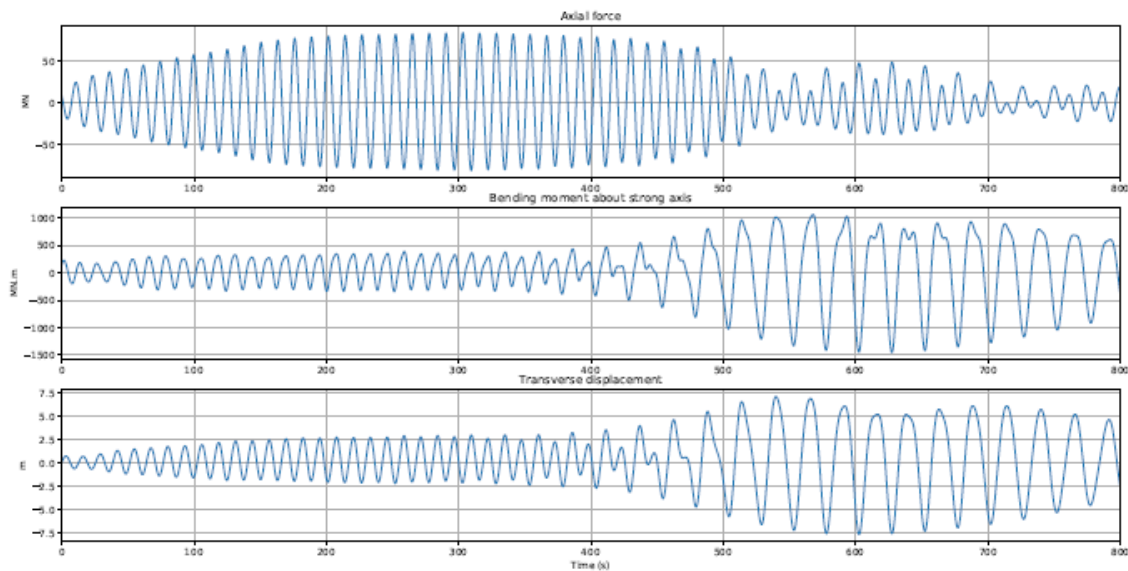
Figure 8-1. $H = 0.9m$, $C_d = 0$.
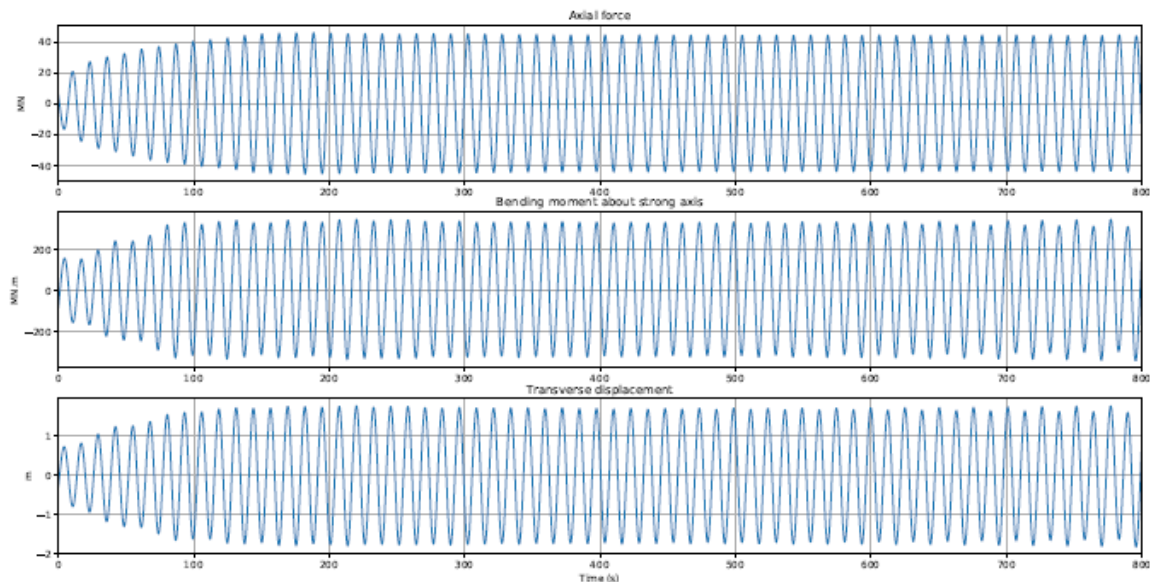
Figure 8-2. $H = 0.9m$, $C_d = 1.0$.
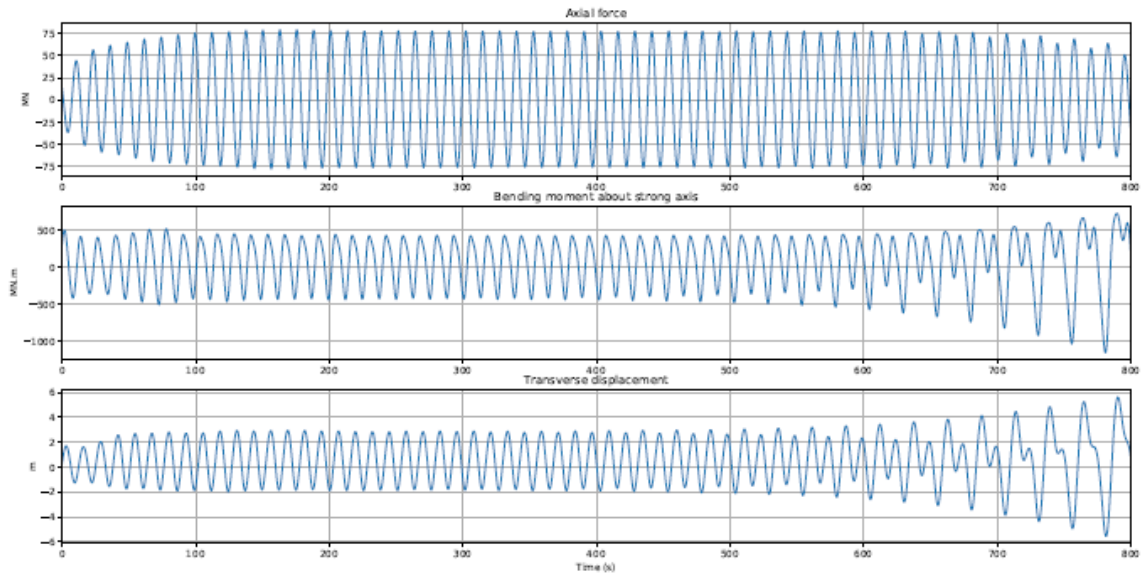
Figure 8-3. $H = 1.8m, C_d = 1.0$.
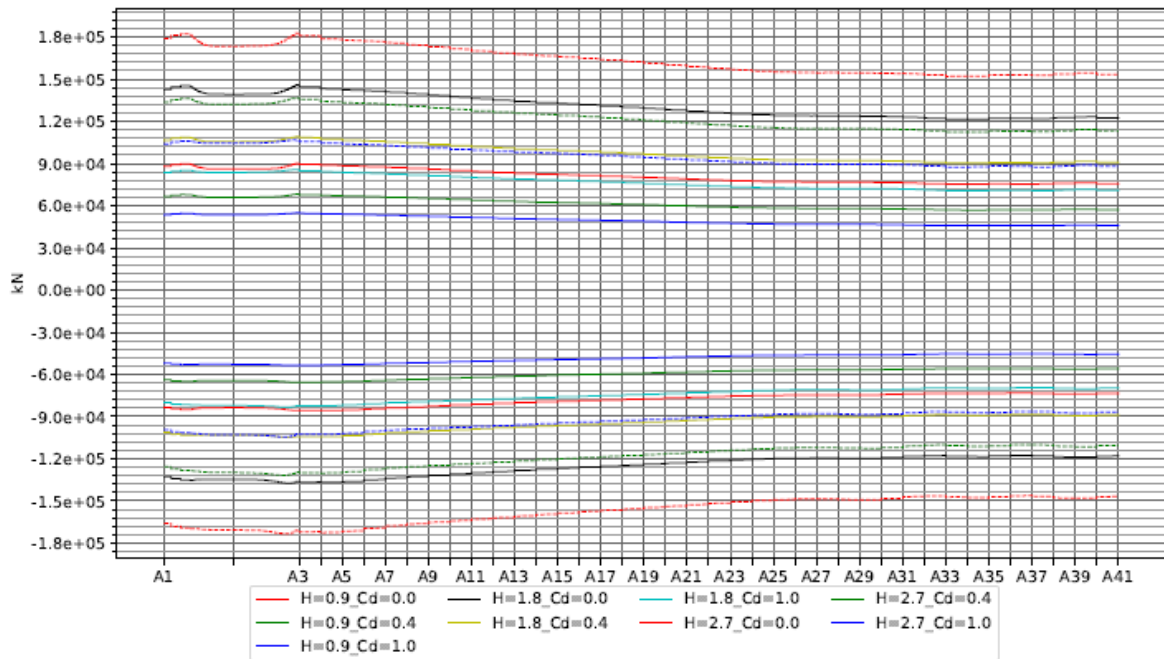
Figure 8-4. Envelope of axial force.
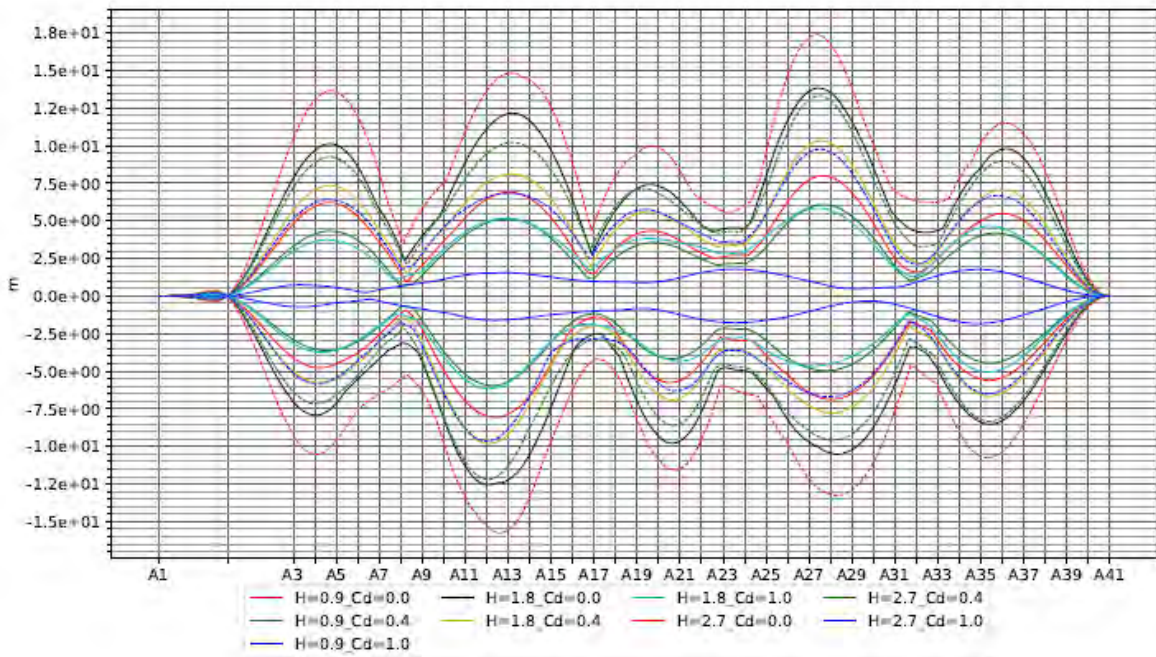
Figure 8-5. Envelope of transverse displacement.

8.2.2   Comparison with linear response

As an approximation of the linear response, a wave height of 0.1m was applied to the OrcaFlex model and the resulting response scaled by a factor 9, post simulation, to mimic a linear analysis with wave height $H = 0.9m$. The resulting maximum axial force, strong axis bending moment and transverse displacement responses are shown in Figure 8-6. The results from this serves as reference solutions, in which the effect of parametric resonance is not present. The corresponding envelopes curves of axial force and transverse displacement are compared with simulations based on $H = 0.9m$ and pontoon drag coefficients $C_d = 0.4$, $C_d = 1.0$ and $C_d = 2.0$. The result from the linear analysis shows a higher axial force, as depicted in Figure 8-7, but a significantly lower strong axis bending moment, shown in Figure 8-8.
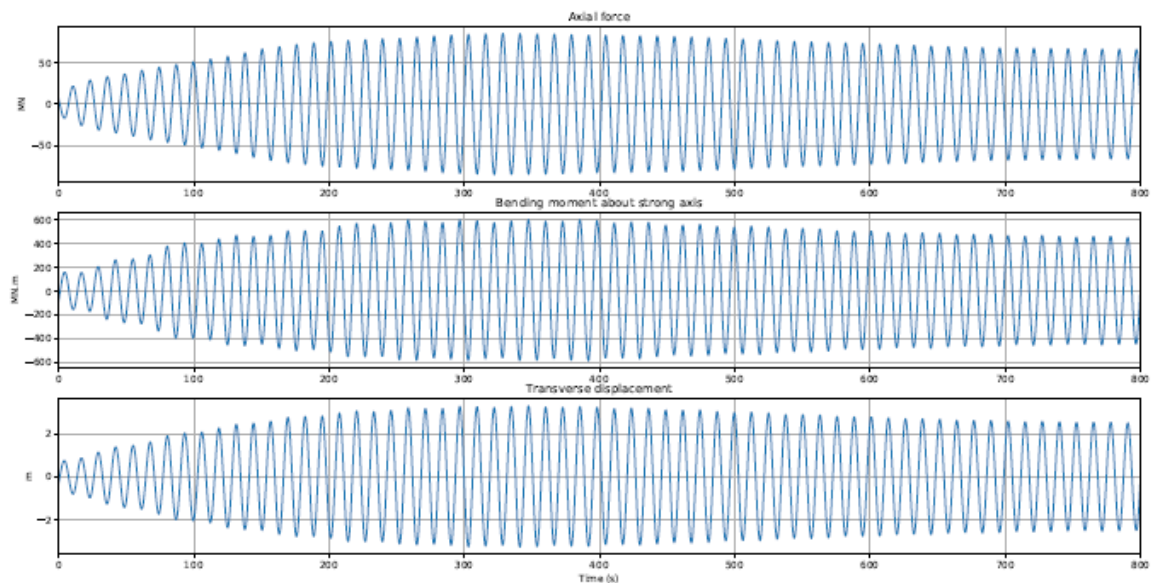
Figure 8-6. Quasi-linear simulation, with scaled results. $H = 0.9m$, $C_d = 0$. No parametric resonance is present.
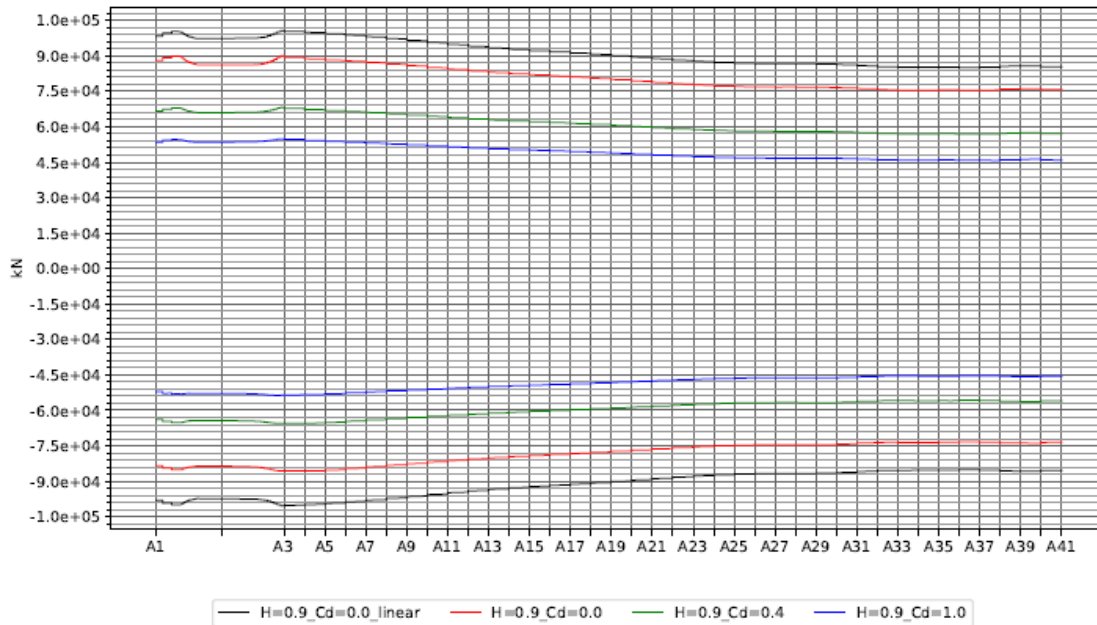
Figure 8-7. Envelope of axial force.
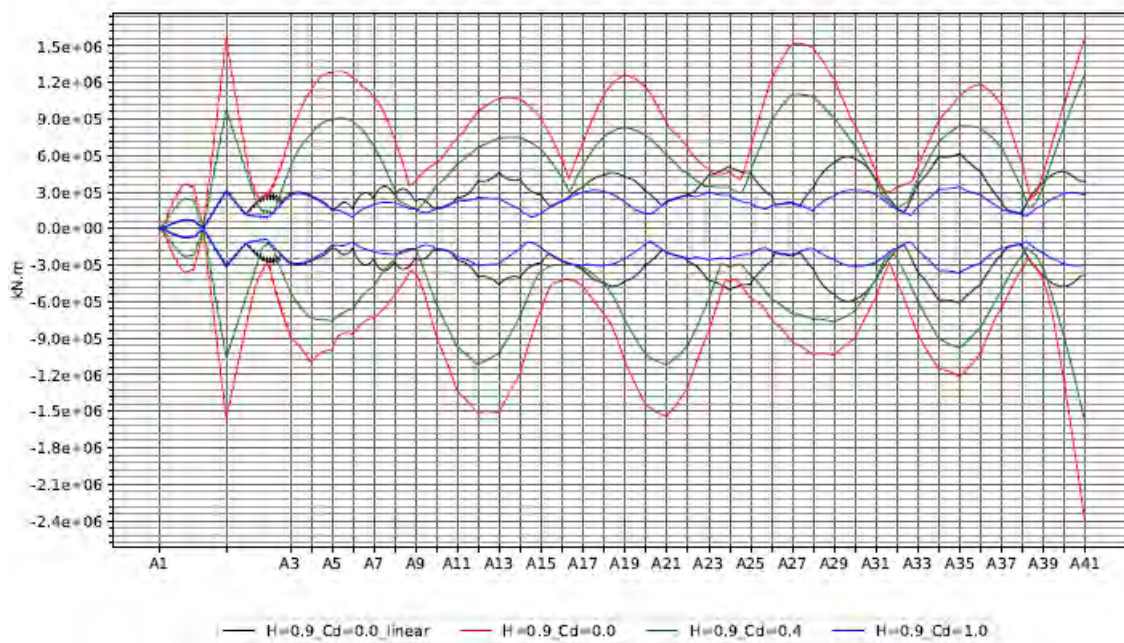
Figure 8-8. Envelope of strong axis bending moment.

8.3   Regular wave analysis of K12

Regular wave analyses were performed with $H = 0.9m$, $H = 1.8m$, $H = 2.7m$, showing no parametric excitation. The mooring lines are modelled as linear springs and with a quadratic damping coefficient, based on the method described in Appendix F, Enclosure 2. The same analysis has been performed with removing the mooring quadratic damping, denoted as *NoMdamp* in the plot legends. As indicated in the parametric resonance occur without the mooring damping in simulations with wave height of 1.8m and 2.7m. Envelope values of axial forces and transverse displacement from the different combinations of wave height and drag coefficient are shown in Figure 8-9 and Figure 8-10, respectively.
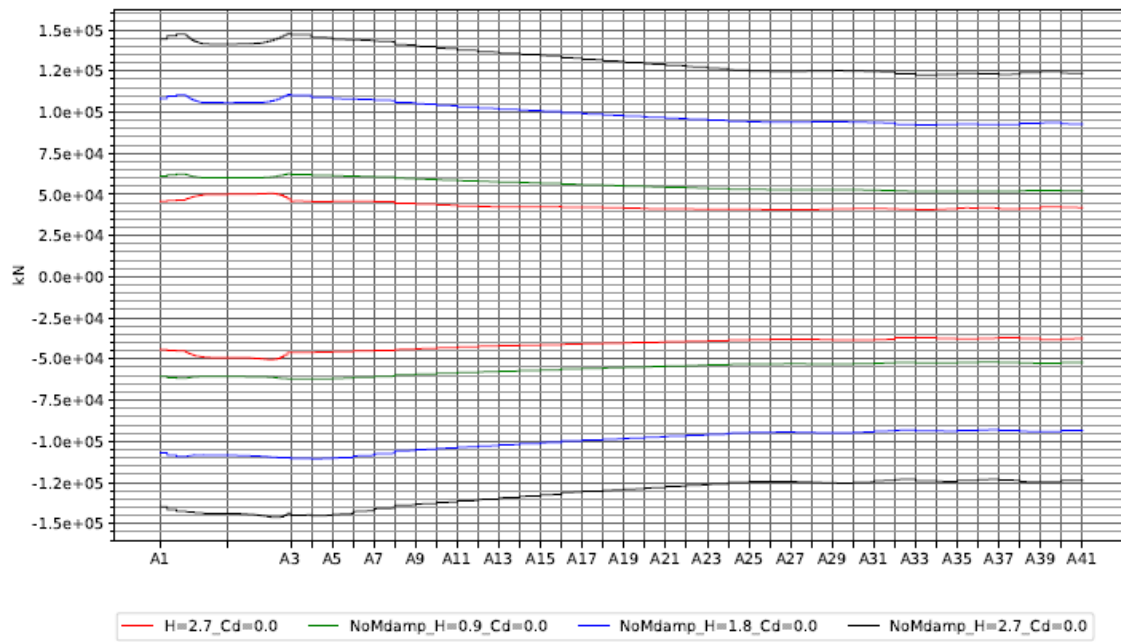
Figure 8-9. Axial force on K12.

Figure 8-10. Transverse displacement on K12.

To supplement the envelope plots, the time histories of the maximum response values of axial forces, strong axis bending moment and transverse displacement are shown in Figure 8-11 and Figure 8-12, corresponding to wave heights 1.8m and 2.7m, respectively. These simulations were conducted without any drag damping on the pontoons, and the latter simulation was furthermore based on no mooring damping.
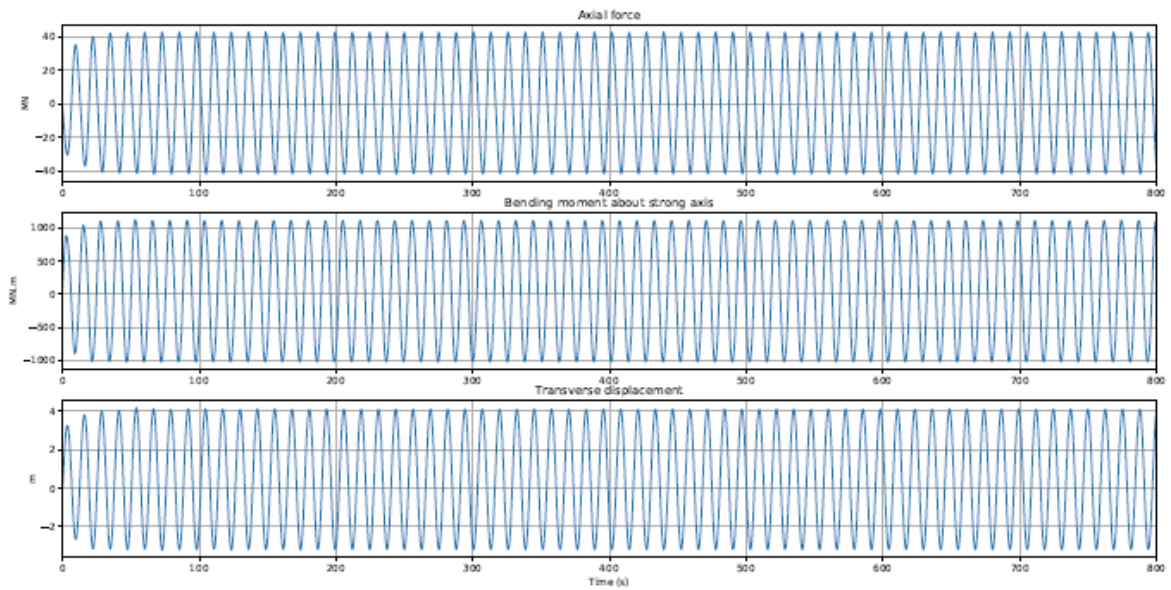
Figure 8-11. Axial force and response for K11 with a regular wave with wave height $H = 2.7m$. The drag damping coefficient was set to $C_d = 0$.
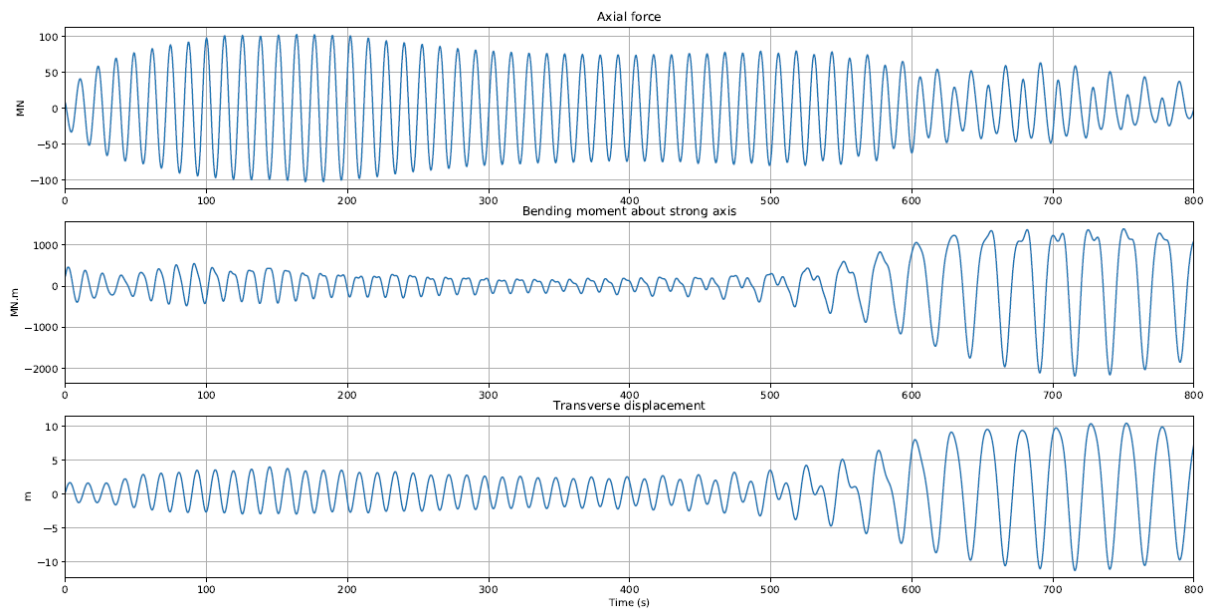
Figure 8-12. No mooring damping, $H = 1.8m$, $C_d = 0$.

8.4   Regular wave analysis of K14

Regular wave analyses were performed with $H = 0.9m$, $H = 1.8m$, $H = 2.7m$, showing no parametric resonance. The mooring lines are modelled as linear springs and with a quadratic damping coefficient, based on the method described in Appendix F, Enclosure 2. The same analysis has been performed with removing the mooring quadratic damping, denoted as *NoMdamp* in the plot legends. Envelope values of axial forces and transverse displacement from the different combinations of wave height and drag coefficient are shown in Figure 8-13 and Figure 8-14, respectively. As can be seen parametric resonance occur without the mooring damping when the wave height is 1.8m and 2.7m.
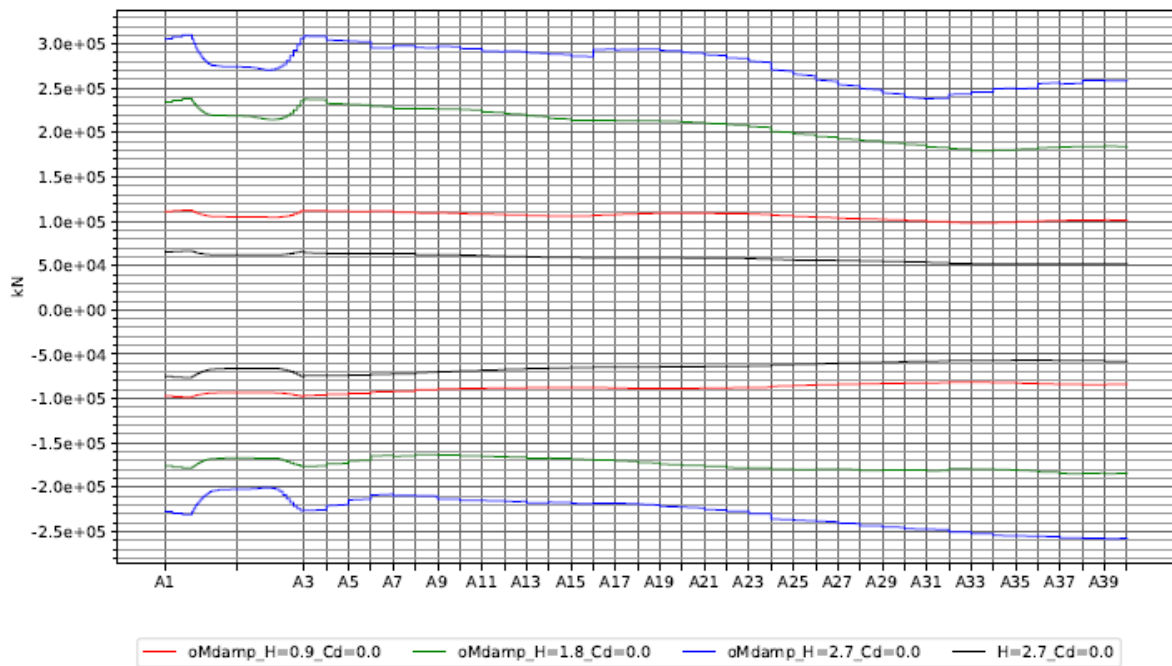
Figure 8-13. Envelope of axial force.
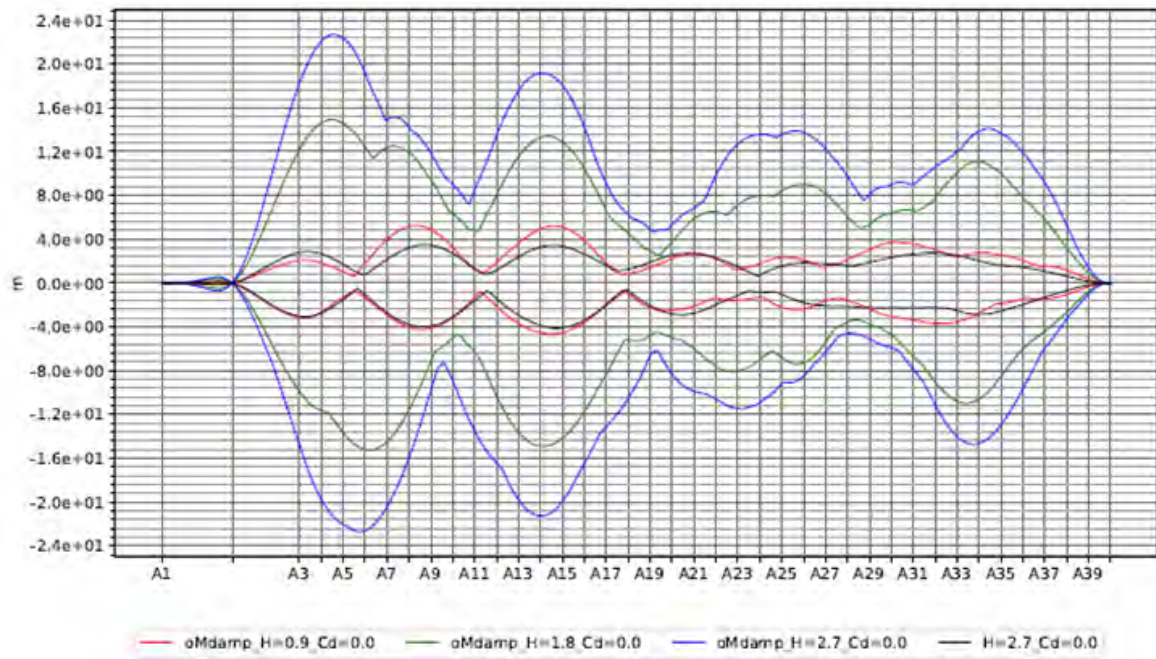
Figure 8-14. Envelope of transverse displacement.

8.5   Stochastic analysis of the K11 concept

8.5.1   Long-crested sea state in the swell frequency regime

To give a better understanding of parametric resonance and to assess whether the phenomenon can be simulated in OrcaFlex, K11 was simulated with 34 3-hour realizations of long crested sea. In all the realizations, the axial force response is significantly higher than the onset criterion for parametric resonance. This has only been done to obtain a better understanding of the physics of the problem, and as illustrated in the note from NTNU the extremes may possible only be detected when simulating significantly more simulations [2].

As a simplification, the sea state is simulated as long-crested and with a wave angle of 260° (not given in the design basis). The peak period is set to the eigenperiod of the mode with the highest axial response (13.1s), and $H_s = 0.46m$. The strong axis stiffness was somewhat adjusted to ensure that half the frequency coincides with the natural frequency of mode 4. No drag nor hydrodynamic damping is included in the simulations, resulting in a very high axial force response. Figure 8-15 shows a 3D visualization of the response spectra along the bridge girder based on the time series response from a selected simulation. The figure indicates that the axial force variation induces large response at half the frequency (double the period). Furthermore, the envelope plots of axial force and transverse displacement are shown in Figure 8-16 and Figure 8-17, respectively, for all the realizations. The corresponding maximum response values for all realizations are shown as probability papers in Figure 8-18 and Figure 8-19, indicating an apparent linear trend.
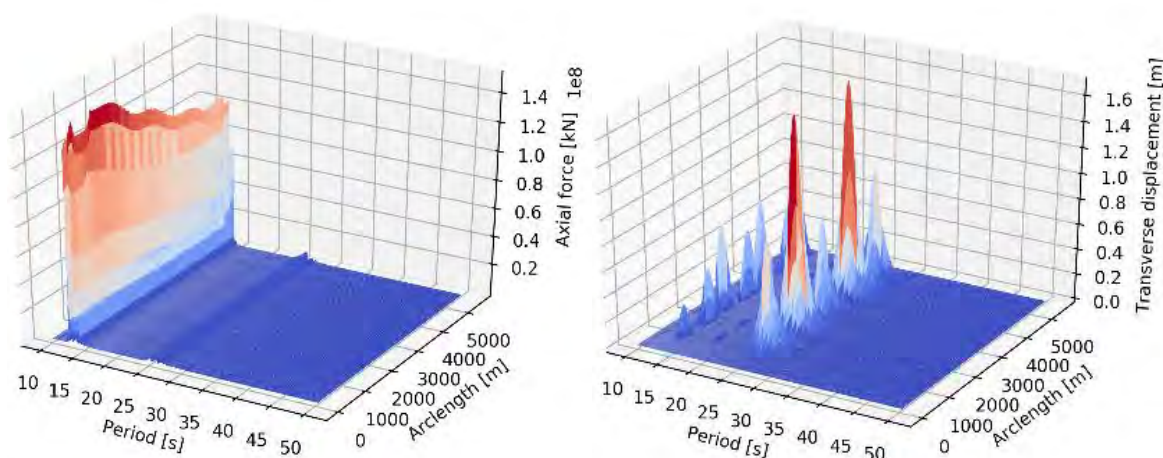
Figure 8-15: 3D visualization of the response spectra (axial force on the left, transverse displacement on the right) along the bridge girder based on the time series response from a selected simulation.
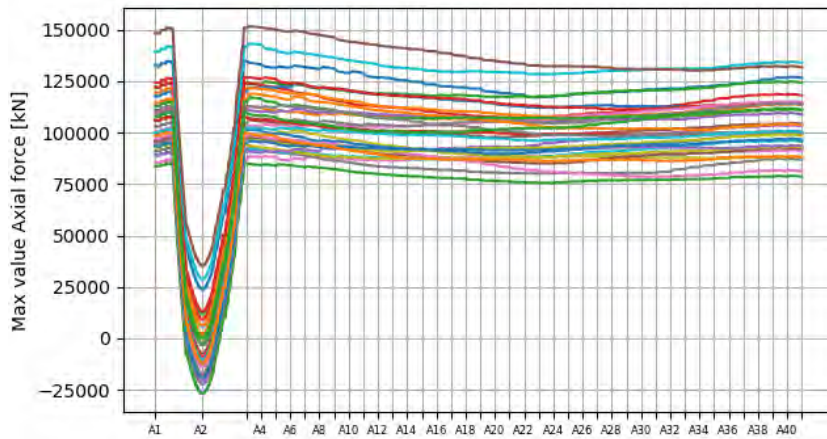
Figure 8-16: Observed maximum axial force at each evaluated point along the bridge axis from each simulation.
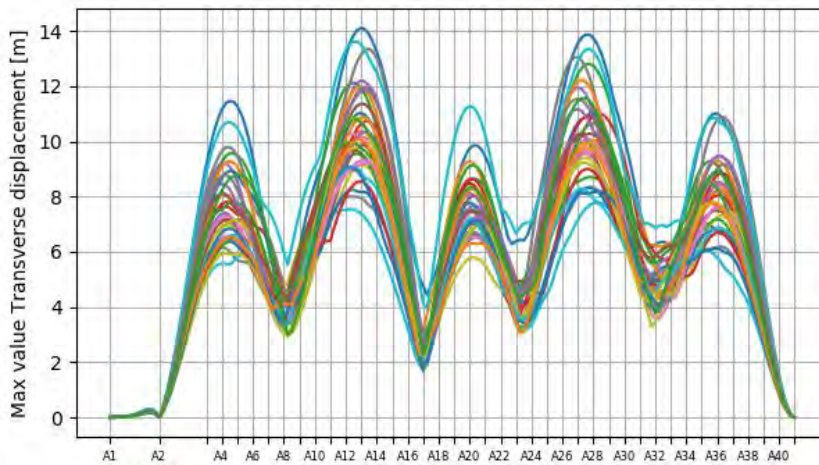

Figure 8-17: Observed maximum transverse displacement at each evaluated point along the bridge axis from each simulation.
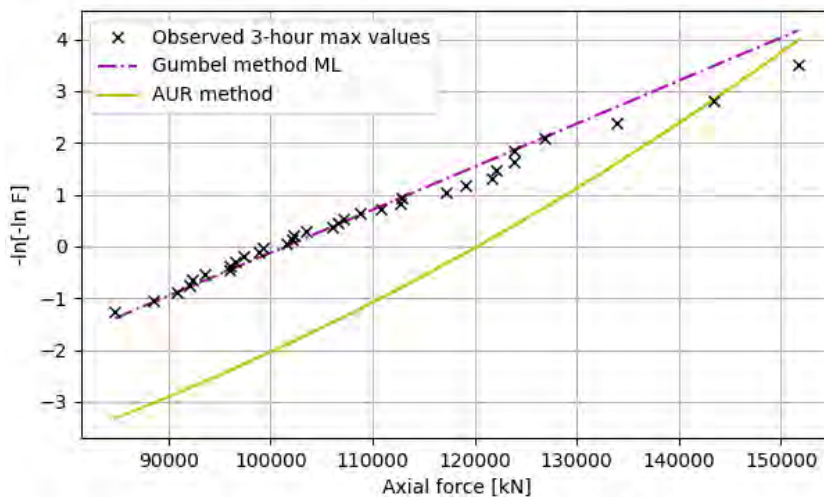

Figure 8-18. Observed maximum axial force at the point along the bridge with the highest response for each simulation, plotted together with a Gumbel fit from the observed maximum and an AUR-method fit of the time series.
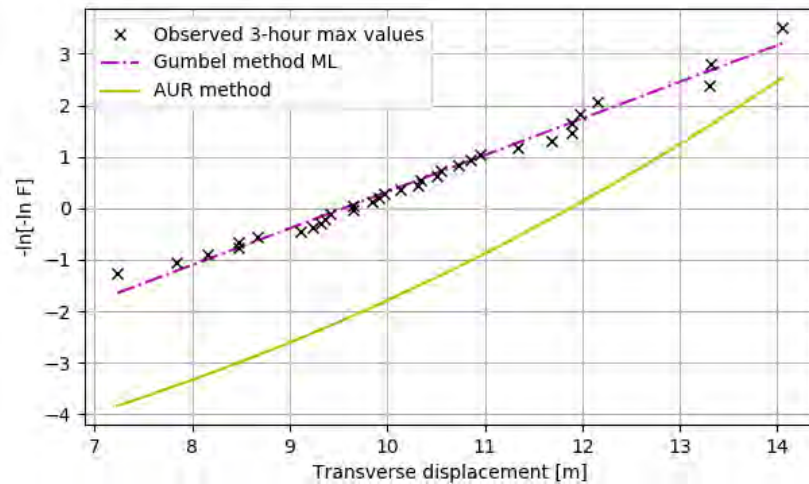
Figure 8-19: Observed maximum transverse displacement at the point along the bridge with the highest response for each simulation, plotted together with a Gumbel fit from the observed maximum and an AUR-method fit of the time series.

8.5.2   Short crested sea state in the swell frequency domain

OrcaFlex was used to simulate the in short-crested swell sea response, with and without a background white noise, as presented in Section 4.3. The analyses were conducted for the sea state presented in Table 8-1. The white noise force was simulated as a flat white noise elevation spectrum with values $S_\eta(\omega) = 1 sm^2$, defined between 0.0333 and 0.05 Hz. The spectrum value approximately represents an applied background force of $S_0(\omega) = 1 \cdot 109 \, sN^2$, simulated in the SDOF model. Four 1-hour realizations of each of the following cases were simulated with a time step of 0.25 seconds: (1) swell only, (2) white noise only, (3) swell and white noise swell only. Figure 8-20 shows a snapshot of a 10000-year swell state with and without the white noise external excitation, indicating a large response due to a 10000-year swell state.

Table 8-1: Short crested swell sea state simulated in OrcaFlex, for validation of SDOF model.

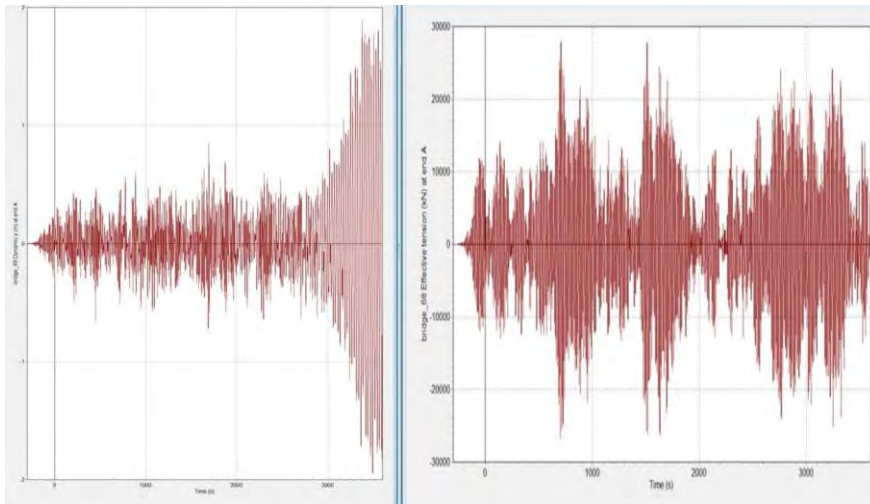| Significant wave height, H_s	Peak period, T_p	Wave direction	Directional spreading exponent (n)	Peakedness, γ
0.46 m	12.65 s	285 °	10	5

Figure 8-20: Snapshot from a stochastic realization of a 10000-year swell sea state (without white noise) in OrcaFlex. The realization indicate that parametric resonance may have been triggered in the global analysis model.

9 Potential mitigation strategies for K11

9.1 Damper in tower

By releasing the lateral constraint of the deck at the tower and in the back spans, the bridge girder can vibrate at the tower position. This allows for dashpots to be positioned at the connection to the tower, to introduce linear damping in the system.

Simplified analyses are conducted by assuming that the dashpots are grounded on the side away from the girder, and the modal analysis was conducted in the same manner as described in Section 3.6, and more in-depth, in Appendix F, Section 6.2. By not introducing any assumptions about the damping in the modal analysis, in contrast to traditional modal analysis where the damping is assumed classical, the physics of the introduction of a damper is better represented. The following results are based on including hydrodynamic contributions but disregarding aerodynamic contributions.

Figure 9-1 shows the critical damping ratio for modes 1–6 with varying damping constants on the discrete damper. As is observed from the figure, a damping constant maximizing the critical damping coefficient can be found for each mode. This fact is supported by the fact that when the damper is larger, the resulting mode shapes change such that the damper is less mobilized. A value of C in the range between $15 \; MN/(m/s)$ and $20 \; MN/(m/s)$ seems to provide a rather good damping contribution to all modes considered.

The critical damping ratio and corresponding critical axial force of modes 1–10 due to the introduction of a damper with characterized by $C = 15 \; MN/(m/s)$ are compared with K11_07 in Figure 9-2. The comparison is made based on a linearized quadratic drag damping corresponding to a 1m displacement of the modes (one at the time). Some of the change in critical amplitude can be explained by the fact that the ratio $k/\hat{k}_g$ is also changed (mode 6), as seen in Figure 9-3, but the largest effect is due to the drastically increased critical damping ratio.

By introducing a large non-classical damping contribution, an assessment of the degree of coupledness of the modes should be conducted before carrying out other analyses based on the diagonalized system. The effect of the damper with $C = 15 MN/(m/s)$ on the modal phase collinearity (MPC) factor, which is described in Appendix F, Section 6.2, is illustrated by comparing Figure 9-4 and Figure 9-5. As expected, the modes have larger phase differences between response values, which indicates a coupled response. This is something that must be investigated more in depth before drawing final conclusions about the increased robustness towards parametric resonance. However, the preliminary findings indicate a vastly improved robustness towards parametric resonance by introducing a damper. Other effects due to the introduction of a damper is not evaluated in this section.
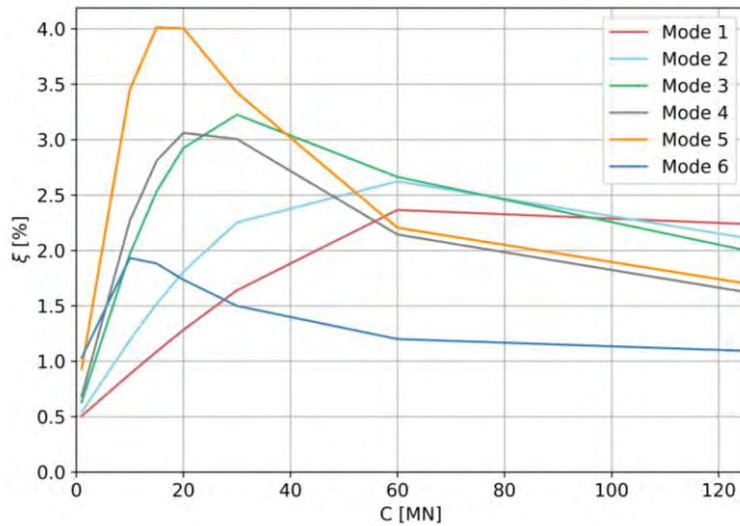
Figure 9-1. Optimal damper constant for the maximization of each modal critical damping ratio.
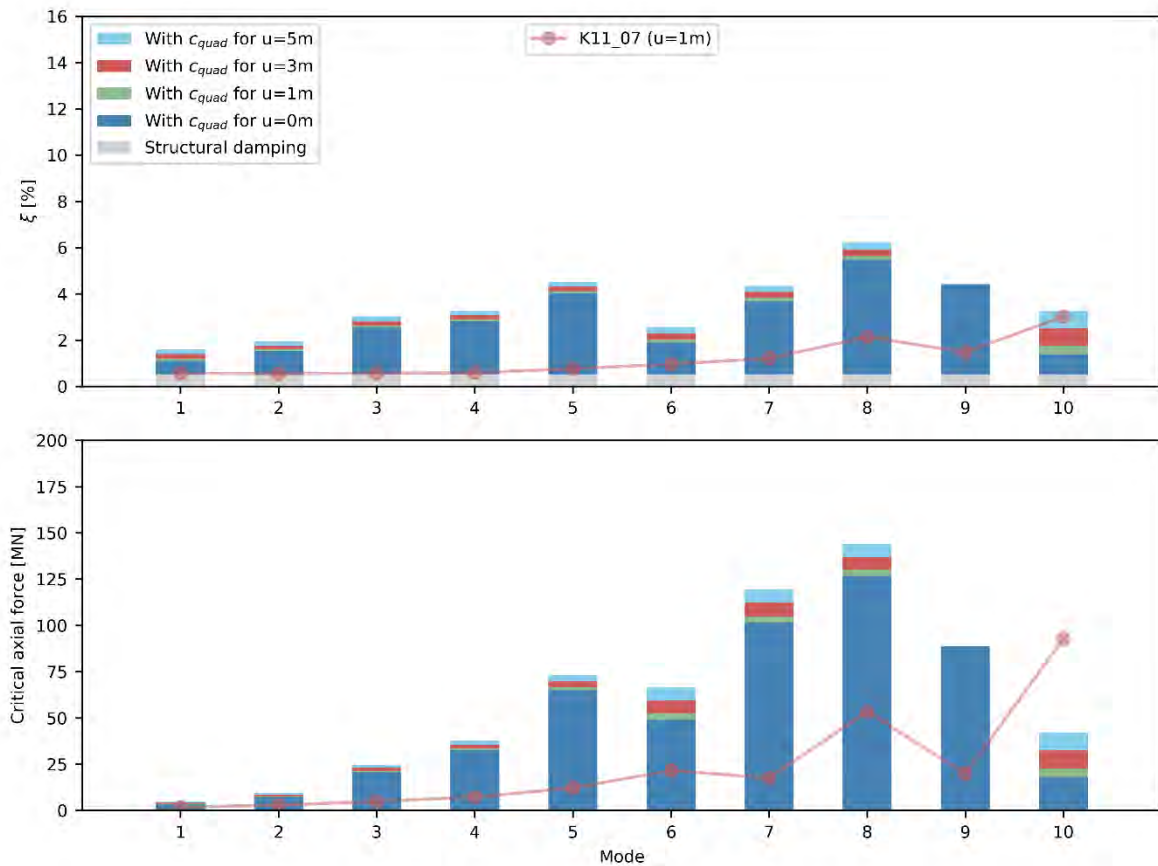

Figure 9-2. Comparison of K11_07 and the modified K11_07 (released lateral motion in tower and back span) with a discrete linear damper with $C = 15MN/(m/s)$.
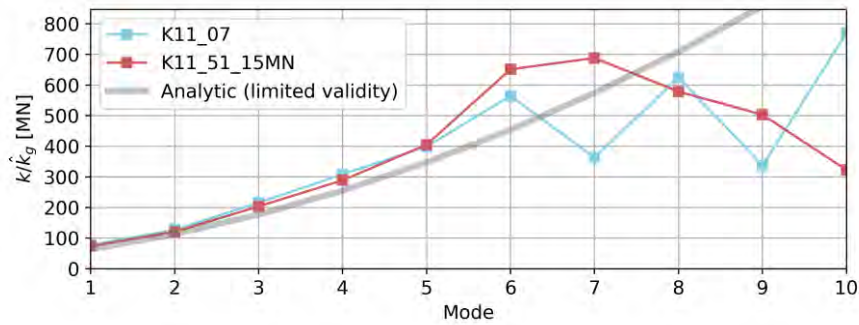
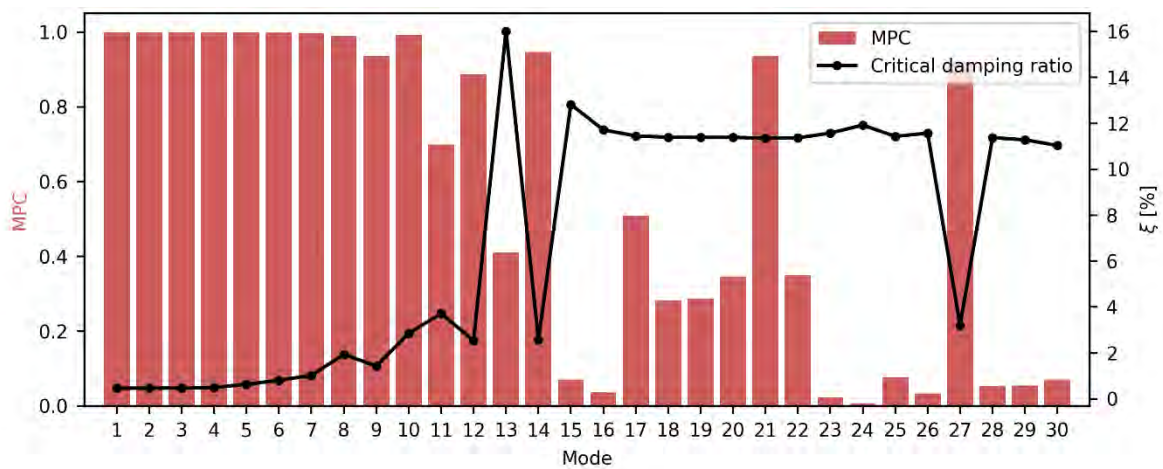*Figure 9-3. Ratio of total static stiffness to geometric stiffness per axial force.*

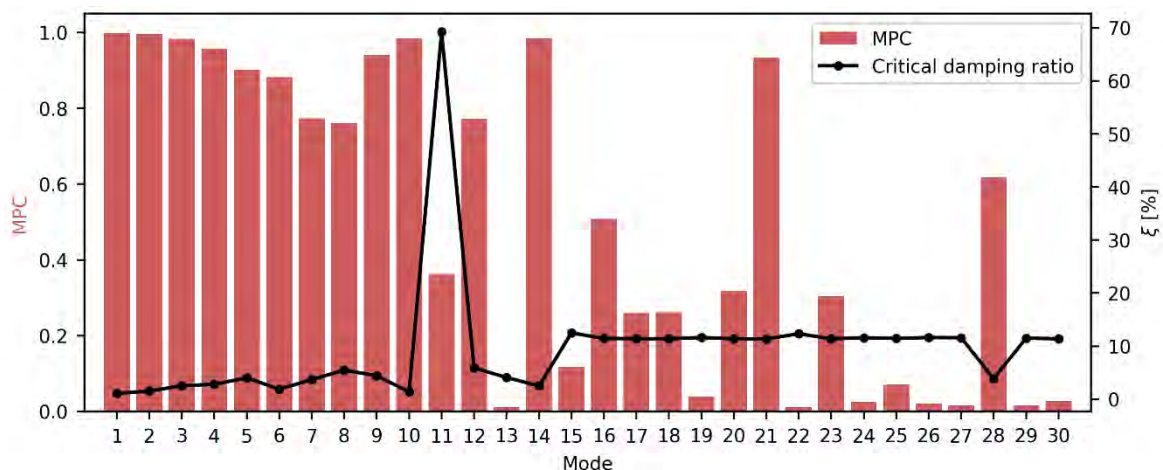*Figure 9-4. Modal phase collinearity (MPC) and critical damping ratio for 30 first modes of K11.*

Figure 9-5. Modal phase collinearity (MPC) and critical damping ratio for 30 first modes of adjusted K11 model (released at tower and back span) with a discrete linear damper with $C = 15\ MN/(m/s)$. The MPC is reduced when including the discrete damper.

9.2 Increased pontoon drag damping

To increase the quadratic damping of K11, the pontoon drag damping could theoretically be increased by increasing the drag factor. The lowest buckling mode has a buckling load close to 65

MN. With a drag coefficient of the pontoon $C_d = 2.0$, the K11 may buckle with a load factor below 2.0, only applying the uniform current forces. This is illustrated in Figure 9-6 as snapshots of the displacement at different time steps. The corresponding load effects for various load factors are illustrated by envelope plots in Figure 9-7–Figure 9-9.

As a consequence, the design of the girder must be strengthened to handle the increased buckling loads, if a larger pontoon drag damping is sought after.
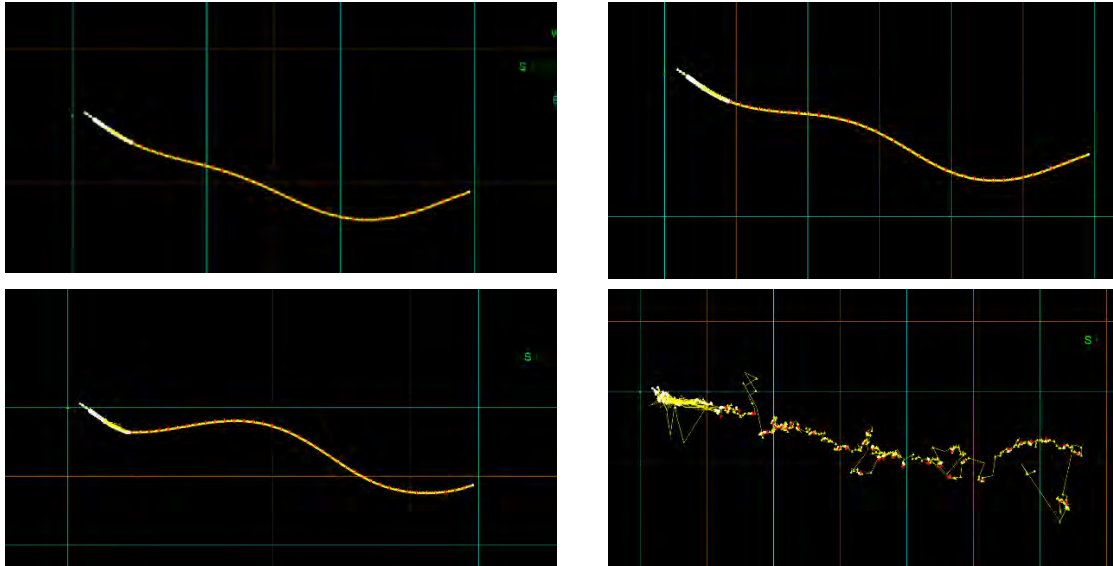

Figure 9-6: Snapshots from the non-linear analysis of the curved bridge in 10.000y current with a load factor of 2.0 and a pontoon drag factor $C_d = 2.0$.
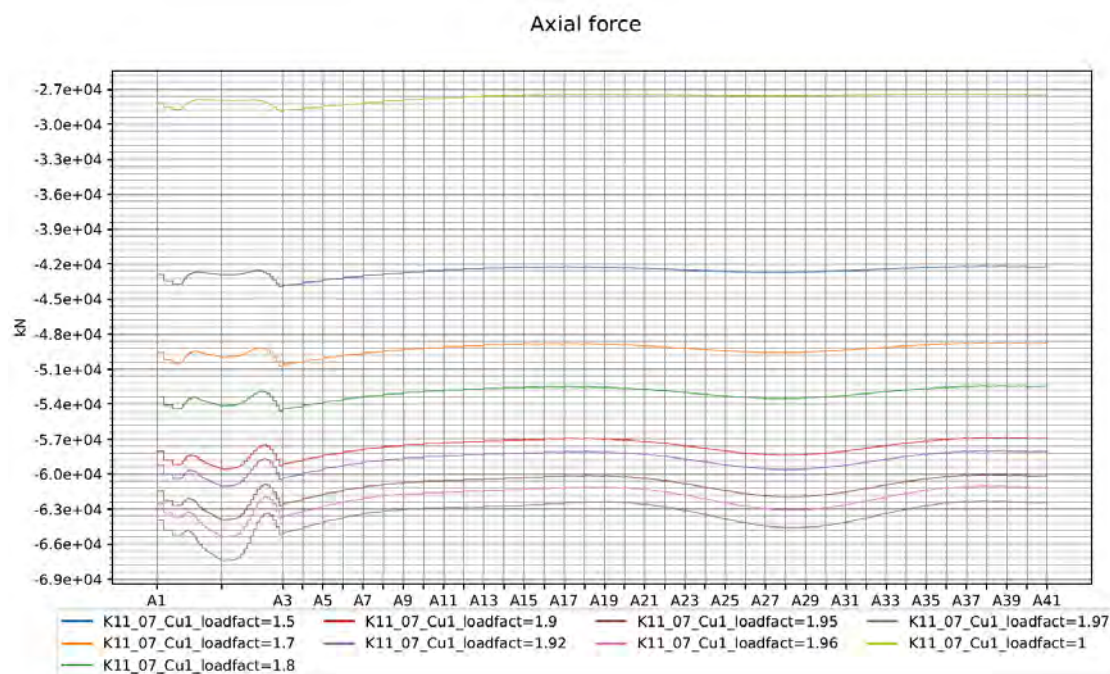

Figure 9-7: Envelope of the axial force from the 10 000-year current load for K11, $C_d = 2.0$ for different load factors. When the load factor is above 1.97 the solution diverges.
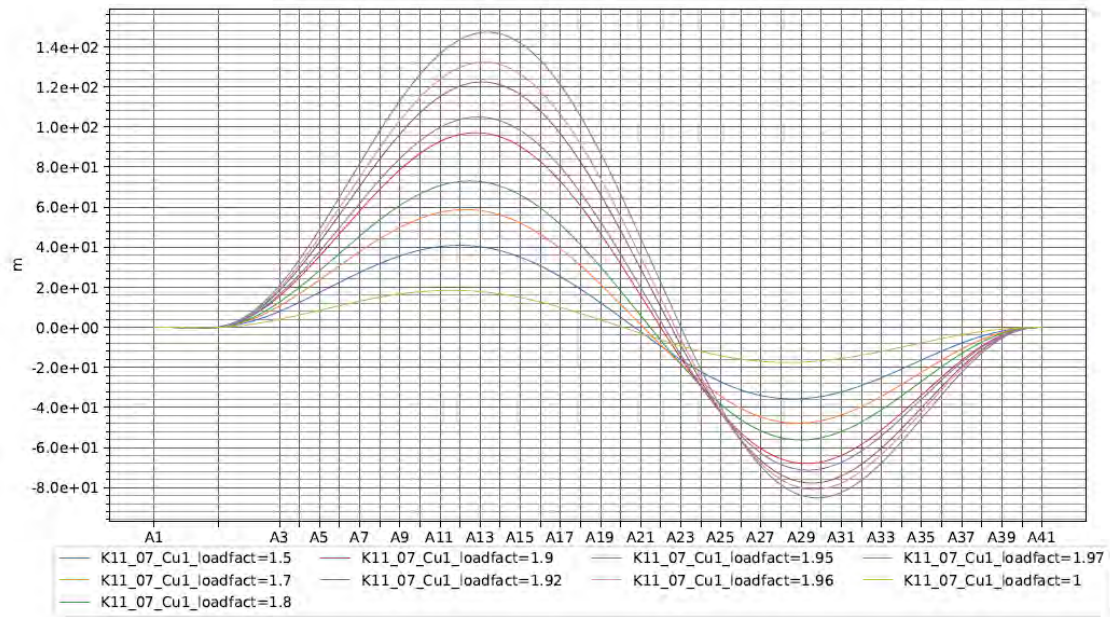
Figure 9-8: Envelope of the transverse displacement from the 10 000-year current load for K11, $C_d = 2.0$ for different load factors. When the load factor is above 1.97 the solution diverges.
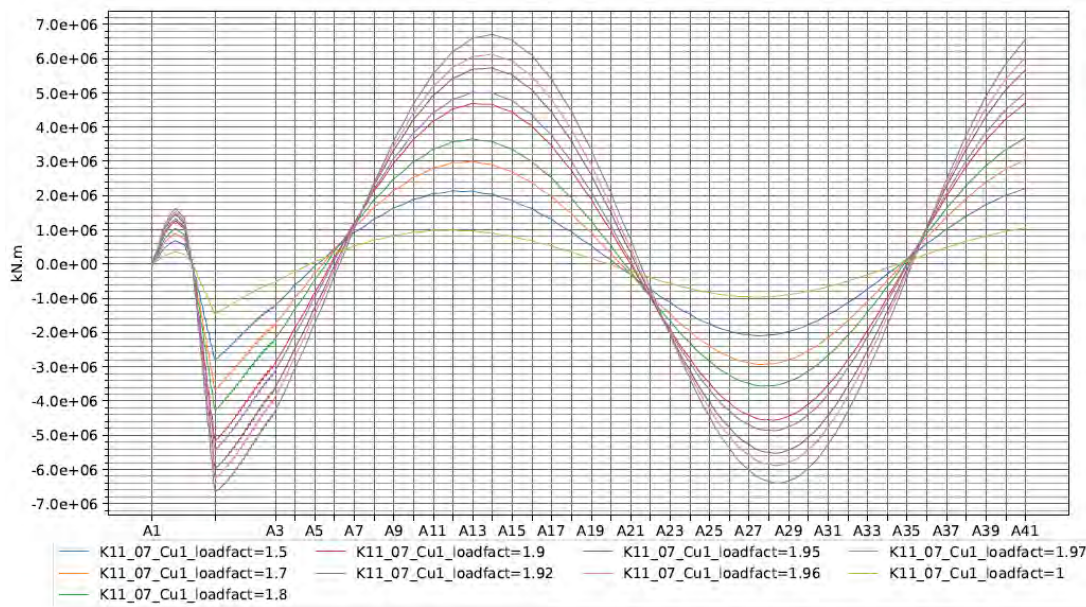

Figure 9-9: Envelope of the girder strong axis moment from the 10 000-year current load for K11, $C_d = 2.0$ for different load factors. When the load factor is above 1.97 the solution diverges.

9.2.1   Considering the Keulegan–Carpenter number

Drag coefficients are known to vary based on amplitude and velocity of the oscillation, typically characterized by the normalized quantity known as K_c-number (Keulegan-Carpenter number). The effect this has on the response from parametric excitation on K11 is briefly studied in Enclosure 4.

10 References

[1] W.-C. Xie, Dynamic stability of structures, Cambridge University Press, 2006.

[2] O. Øiseth, B. Costa og A. Fenerci, «SBJ-32-C4-NTNU-22-RE-001 "Dynamic stability of elastic nonlinear systems subjected to random excitation",» Statens vegvesen, 2018.

[3] Statens vegvesen, «SBJ-01-C4-SVV-01-BA-001 MetOcean Design basis, rev. 1,» 2018.

[4] J. L. Humar, Dynamics of structures, CRC Press, 2012.

[5] I. Kovacic, R. Rand og S. M. Sah, «Mathieu's Equation and Its Generalizations: Overview of Stability Charts and Their Features,» *Applied Mechanics Reviews,* 2018.

[6] M. Shinozuka, «Monte Carlo solution of structural dynamics,» *Computers & Structures,* pp. 855-874, 1972.

[7] A. Naess og T. Moan, Stochastic dynamics of marine structures, New York: Cambridge University Press, 2012.

[8] K. A. Kvåle, R. Sigbjörnsson og O. Øiseth, «Modelling the stochastic dynamic behaviour of a pontoon bridge: A case study,» *Computers & Structures,* pp. 123-135, 2016.

[9] Statens vegvesen, «SBJ-32-C4-SVV-90-BA-001 - Design Basis Bjørnajorden Rev 0,» 2018.

11 Enclosures

Enclosure 1 - 10205546-11-NOT-092 - Analysis of parametric resonance of single-degree-of-freedom systems using Newmark's method and Monte Carlo simulation

Enclosure 2 - Parametric excitation results

Enclosure 3 - 10205546-11-NOT-186 - Verification of modal interpretation of drag damping

Enclosure 4 - 10205546-11-NOT-187 - Effect of KC-dependent drag coefficient on parametric excitation

Enclosure 5 - 10205546-11-NOT-188 - Assessment of risk of parametric excitation of mooring cables

Enclosure 6 - 10205546-11-NOT-189 - Effect of static forces on K12